Article

Cell Metabolism

NAD depletion in skeletal muscle does not compromise muscle function or accelerate aging

Graphical abstract

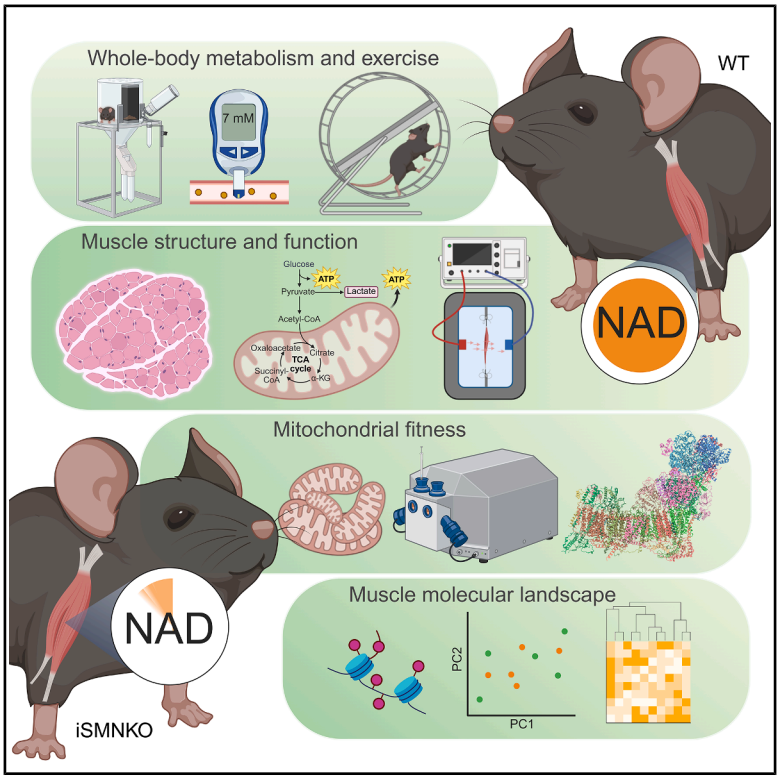

Authors

Sabina Chubanava, Iuliia Karavaeva, Amy M. Ehrlich, ..., Gareth G. Lavery, Atul S. Deshmukh, Jonas T. Treebak

Correspondence

jttreebak@sund.ku.dk

In brief

NAD depletion in skeletal muscle does not impair tissue integrity and function or accelerate aging, as shown in a mouse model with an 85% decrease in muscle NAD^+ levels. Muscle structure, metabolism, and mitochondrial function remain unaffected, suggesting that NAD depletion does not drive age-related muscle decline.

Highlights

- Knockout of *Nampt* in adult mouse skeletal muscle decreases NAD^+ by 85%
- Exercise tolerance and muscle contractility are intact despite NAD depletion
- A 50% decrease in mitochondrial NAD does not affect mitochondrial structure and function
- Lifelong depletion of skeletal muscle NAD does not exacerbate muscle aging

Chubanava et al., 2025, Cell Metabolism *37*, 1460–1481
July 1, 2025
https://doi.org/10.1016/j.cmet.2025.04.002

CellPress

CellPress
OPEN ACCESS

Cell Metabolism

Article

NAD depletion in skeletal muscle does not compromise muscle function or accelerate aging

Sabina Chubanava,[1,14] Iuliia Karavaeva,[1] Amy M. Ehrlich,[1] Roger M. Justicia,[1] Astrid L. Basse,[1] Ivan Kulik,[2] Emilie Dalbram,[1] Danial Ahwazi,[1] Samuel R. Heaselgrave,[3,13,15] Kajetan Trošt,[1] Ben Stocks,[1] Ondřej Hodek,[4] Raissa N. Rodrigues,[1] Jesper F. Havelund,[5] Farina L. Schlabs,[1] Steen Larsen,[6,7] Caio Y. Yonamine,[1] Carlos Henriquez-Olguín,[8,9] Christian Ludwig,[10] Daniela Giustarini,[11] Ranieri Rossi,[11] Zachary Gerhart-Hines,[1] Thomas Moritz,[1] Juleen R. Zierath,[1,12] Kei Sakamoto,[1] Thomas E. Jensen,[8] Nils J. Færgeman,[5] Gareth G. Lavery,[3,13] Atul S. Deshmukh,[1] and Jonas T. Treebak[1,16,*]

[1]Novo Nordisk Foundation Center for Basic Metabolic Research, Faculty of Health and Medical Sciences, University of Copenhagen, Copenhagen, Denmark
[2]Institute of Translational Stem Cell Research, Helmholtz Diabetes Center, Munich, Germany
[3]Institute of Metabolism and Systems Research, University of Birmingham, Birmingham, UK
[4]Swedish Metabolomics Centre, Department of Forest Genetics and Plant Physiology, Swedish University of Agricultural Sciences, Umeå, Sweden
[5]Department of Biochemistry and Molecular Biology, University of Southern Denmark, Odense, Denmark
[6]Department of Biomedical Sciences, Faculty of Health and Medical Sciences, University of Copenhagen, Copenhagen, Denmark
[7]Clinical Research Centre, Medical University of Bialystok, Bialystok, Poland
[8]Department of Nutrition, Exercise and Sports, Faculty of Science, University of Copenhagen, Copenhagen, Denmark
[9]Center for Exercise Physiology and Metabolism, Department of Kinesiology, Faculty of Medicine, Universidad Finis Terrae, Santiago, Chile
[10]Department of Metabolism and System Science, College of Medicine and Health, University of Birmingham, Birmingham, UK
[11]Department of Biotechnology, Chemistry and Pharmacy, University of Siena, Siena, Italy
[12]Section of Integrative Physiology, Department of Molecular Medicine and Surgery and Department of Physiology and Pharmacology, Karolinska Institutet, Stockholm, Sweden
[13]Centre for Systems Health and Integrated Metabolic Research, Department of Biosciences, Nottingham Trent University, Nottingham, UK
[14]Present address: Institute for Diabetes and Obesity, Helmholtz Diabetes Center, Munich, Germany
[15]Present address: Center of Hypothalamic Research, Department of Internal Medicine, University of Texas Southwestern Medical Center, Dallas, TX, USA
[16]Lead contact
*Correspondence: jttreebak@sund.ku.dk
https://doi.org/10.1016/j.cmet.2025.04.002

SUMMARY

Nicotinamide adenine dinucleotide (NAD) is a ubiquitous electron carrier essential for energy metabolism and post-translational modification of numerous regulatory proteins. Dysregulations of NAD metabolism are widely regarded as detrimental to health, with NAD depletion commonly implicated in aging. However, the extent to which cellular NAD concentration can decline without adverse consequences remains unclear. To investigate this, we generated a mouse model in which nicotinamide phosphoribosyltransferase (NAMPT)-mediated NAD^+ biosynthesis was disrupted in adult skeletal muscle. The intervention resulted in an 85% reduction in muscle NAD^+ abundance while maintaining tissue integrity and functionality, as demonstrated by preserved muscle morphology, contractility, and exercise tolerance. This absence of functional impairments was further supported by intact mitochondrial respiratory capacity and unaltered muscle transcriptomic and proteomic profiles. Furthermore, lifelong NAD depletion did not accelerate muscle aging or impair whole-body metabolism. Collectively, these findings suggest that NAD depletion does not contribute to age-related decline in skeletal muscle function.

INTRODUCTION

Nicotinamide adenine dinucleotide (NAD: NAD^+ and NADH) is a cofactor that plays a central role in energy metabolism. NAD^+ facilitates substrate oxidation, capturing reductive potential that is subsequently transferred to the mitochondrial electron transport chain (ETC). This process generates the inner mitochondrial membrane potential (IMMP), which drives ATP synthesis. NAD^+ is also integral to cellular signaling pathways regulated by sirtuins, ADP-ribosyltransferases, and ADP-ribosyl cyclases.[1–4] These enzymes utilize NAD^+ as a co-substrate, influencing metabolism, genomic stability, cell viability, and aging.[5–7] Additionally, NAD serves as a substrate for NAD kinases, the sole enzymes responsible for synthesizing cellular NADP ($NADP^+$ and NADPH). NADP functions as a redox carrier in anabolic reactions and in maintaining oxygen balance by modulating reactive

CellPress
OPEN ACCESS

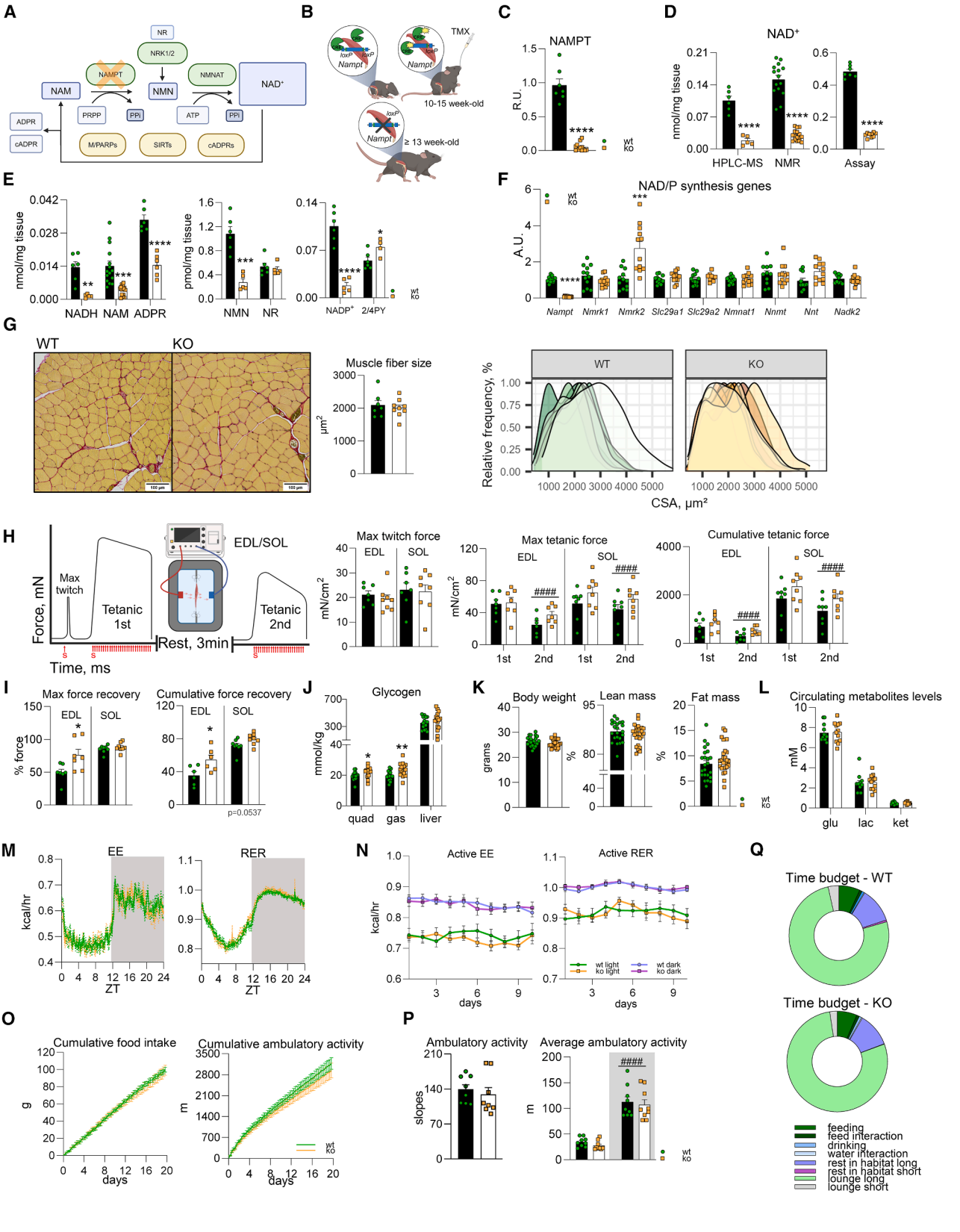

(legend on next page)

oxygen species (ROS) through NADPH oxidases and glutathione reductases (GRx).[8]

Increasing NAD availability through supplementation with its precursors potentially enhances the activity of NAD-dependent enzymes and possibly improves tissue function and overall health.[9–21] Conversely, NAD depletion is expected to impair energy homeostasis and tissue functionality. In skeletal muscle, NAD deficiency has been linked to mitochondrial myopathy, sarcopenia, and cancer cachexia.[18,22–24] Additionally, aging-associated decrease in skeletal muscle NAD concentrations correlate with dysfunction and disuse, suggesting a role in frailty and functional decline.[25–27] This aligns with the findings that embryonic deletion of nicotinamide phosphoribosyltransferase (*Nampt*), a key NAD salvage enzyme, leads to progressive muscle degeneration and metabolic disruptions.[28,29]

Here, we demonstrate that skeletal muscle function remains intact despite an 85% reduction in NAD^+ content. Using an inducible skeletal-muscle-specific *Nampt* knockout (iSMNKO) model, we disrupted NAD synthesis in adult mice, avoiding confounding effects during muscle development.[28,29] Although iSMNKO mice showed increased exercise-induced energetic stress and modest oxidative metabolism alterations, muscle mass, tissue integrity, contractility, and exercise performance were unaffected. At the molecular level, NAD-depleted muscle exhibited normal transcriptomic, proteomic, and mitochondrial profiles, as well as preserved DNA methylation. Markers of whole body and muscle health remained at wild-type (WT) levels even after lifelong NAD depletion. These findings suggest that skeletal muscle health is less dependent on NAD than previously thought. Notably, NAD depletion exceeding aging-related declines (10%–30%) does not impair muscle function or accelerate its deterioration with aging.

RESULTS

Inducible *Nampt* knockout reduces NAD by 85% in adult skeletal muscle

NAMPT catalyzes the conversion of nicotinamide (NAM) to nicotinamide mononucleotide (NMN) (Figure 1A). Inducible *Nampt* deletion in mature skeletal muscle (Figure 1B) led to a substantial reduction in NAMPT and NAD^+, NADH, NMN, and other NAD-related metabolites, including $NADP^+$ (Figures 1C–1E). Despite this depletion, mitochondrial NADP synthesis enzymes NAD kinase 2 (*Nadk2*) and NADPH-producing NAD(P) transhydrogenase (*Nnt*) showed no compensatory upregulation, although nicotinamide riboside kinase 2 (*Nmrk2*), responsible for the generation of NMN from nicotinamide riboside (NR), was upregulated (Figures 1A and 1F). At the same time, muscle NR levels and expression of *Slc29a1/2* transporters involved in its uptake remained unchanged (Figures 1E and 1F). Nevertheless, we cannot exclude the contribution of NRK2 in maintaining NAD^+ levels in iSMNKO muscle. NAMPT depletion was expected to elevate NAM and reduce NAD^+ cleavage products, such as adenosine diphosphate ribose (ADPR) (Figure 1A). However, both ADPR and NAM levels were 60% and 80% lower, respectively (Figure 1E). This likely resulted from increased methylation-independent NAM efflux[30] and degradation into methyl pyridines (Figure 1E), without upregulation of nicotinamide N-methyltransferase (*Nnmt*) (Figure 1F).

Muscle structure, morphology, and function remain intact in iSMNKO mice

To assess whether NAD depletion induces aging-like muscle phenotypes, we examined muscle morphology and function. Despite lower NAD levels, iSMNKO tibialis anterior (TA) fibers retained normal structure and size (Figure 1G). Force production in extensor digitorum longus (EDL) and soleus (SOL) muscles was comparable between iSMNKO and WT mice in single-twitch and tetanic contractions (Figures 1H and S1A). However, iSMNKO EDL exhibited improved force recovery during repeated tetanic contractions (Figure 1I), suggesting reduced fatigability, potentially linked to elevated glycogen content (Figure 1J). Residual glycogen levels post contraction were similar (Figure S1B), implying enhanced glycogen breakdown in iSMNKO muscles during exercise. Overall, muscle structure and contractility remained intact despite NAD depletion.

Figure 1. Inducible skeletal muscle *Nampt* knockout alters NAD metabolism without disrupting basal whole-body metabolism and muscle function

(A) NAMPT-mediated NAD^+ biosynthesis pathway.
(B) Schematic of the inducible skeletal muscle-specific *Nampt* knockout (iSMNKO) mouse model.
(C) NAMPT abundance in gastrocnemius (GAS) muscle of 25-week-old male WT (*Cre*-negative) and iSMNKO mice 10 weeks after tamoxifen.
(D) GAS NAD^+ measured by HPLC-MS, 1D-NMR, and biochemical cycling assay.
(E) NAD metabolites measured by 1D-NMR (NAM in GAS) and HPLC-MS (QTOF) (others in tibialis anterior, TA).
(F) Expression of NAD/P biosynthesis genes in quadriceps (QUAD) of WT and iSMNKO mice.
(G) Mean muscle fiber size and fiber size distribution in WT and iSMNKO TA stained with Picrosirius red (PSR); representative images, scale bar length, 100 μm.
(H) *Ex vivo* muscle force assay, extensor digitorum longus (EDL), and soleus (SOL) maximal single-twitch and cumulative force production.
(I) Recovery from tetanic muscle contraction.
(J) Muscle and liver glycogen content of randomly fed mice (ZT3–7).
(K) Body weight and composition.
(L) Ambulatory levels of blood lactate, glucose, and ketones (ZT7 and 8).
(M) Average energy expenditure (EE), respiratory exchange ratio (RER) (5 days), cumulative feed intake, and ambulatory activity (20 days) of WT and iSMNKO mice ($n = 8$).
(N) Day- and night-time EE and RER during ambulatory activity (10 days) ($n = 8$).
(O–Q) Home-cage behavior time distribution (feeding, walking, resting, etc.) (%) ($n = 8$).
ZT, zeitgeber time; *n*, biological replicates. Mean values are plotted. Error bars represent SEM. Statistical significance was tested by unpaired two-tailed Student's t test or two-way ANOVA with Holm-Šídák post hoc test (genotype effect, $^*p < 0.05$, $^{**}p < 0.01$, $^{***}p < 0.001$, $^{****}p < 0.0001$; time of day and round of contraction effects, $^{\#\#\#\#}p < 0.0001$). Mice were male and 15–20 weeks of age, unless stated otherwise.

CellPress
OPEN ACCESS

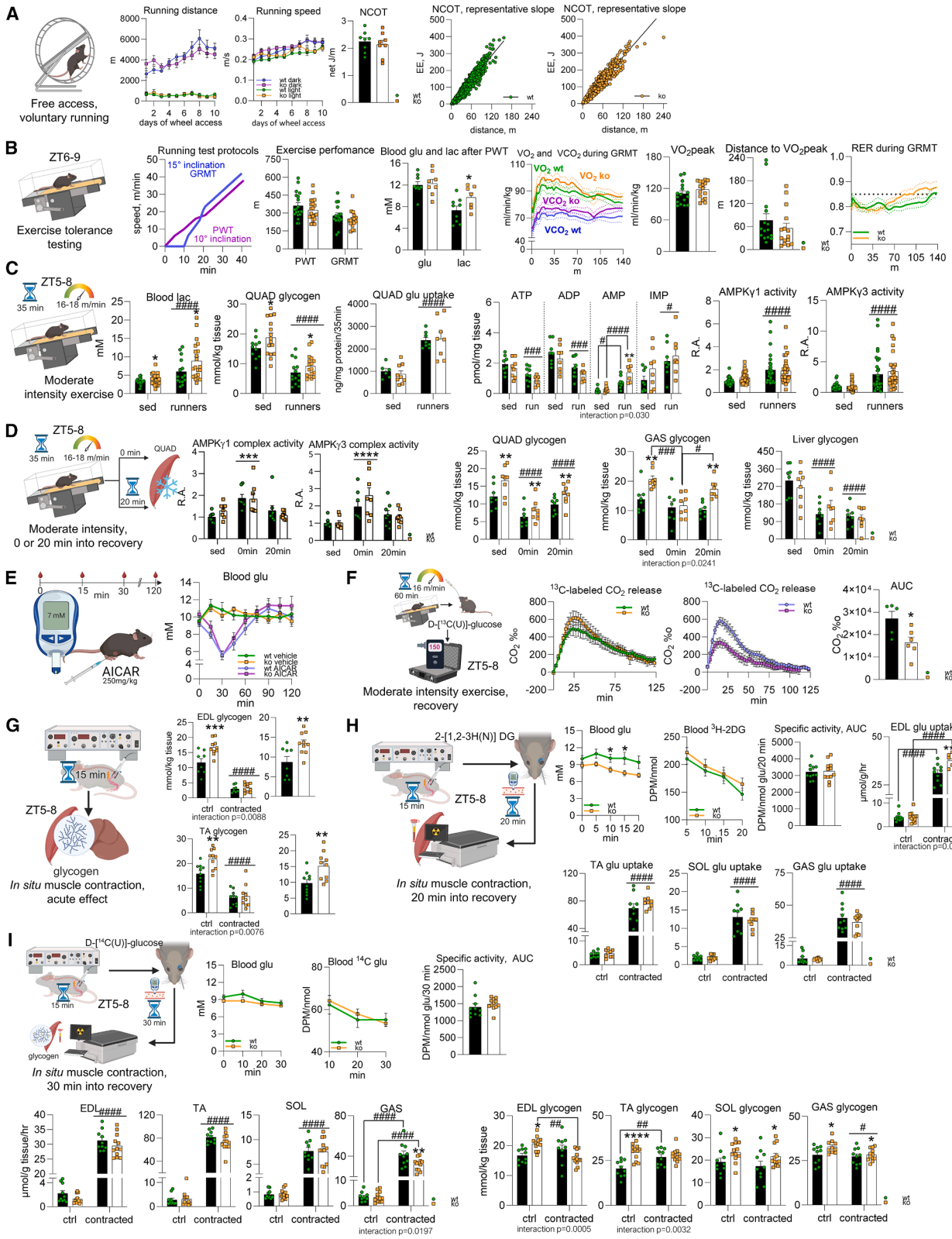

(legend on next page)

Whole-body metabolism is largely unaffected in iSMNKO mice

Given the metabolic importance of skeletal muscle, we examined whole-body physiology. iSMNKO and WT mice showed no differences in body weight and composition (Figures 1K and S1D) or metabolic markers, including blood glucose, lactate, and ketones (Figure 1L). Indirect calorimetry revealed no genotype differences in respiration, ambulatory activity, or feeding behavior. Respiratory exchange ratio (RER) remained unchanged (Figures 1M and S1C), indicating normal substrate oxidation. Diurnal energy expenditure (EE) fluctuations (Figures 1M and 1N) and activity patterns (Figures 1O–1Q) were also unaffected, confirming that NAD depletion does not impair systemic metabolism.

Acute high-intensity exercise is well tolerated by iSMNKO mice

Exercise activates muscle oxidative metabolism and imposes substantial whole-body energetic demands.[31] To assess exercise performance, we monitored voluntary wheel running. Both genotypes exhibited similar running frequency, speed, and distance, with no differences in EE (net cost of transport [NCOT]) (Figure 2A). High-intensity treadmill tests, including the power test (PWT) and the graded maximal exercise test (GRMT), showed comparable performance between iSMNKO and WT mice (Figures 2B [left] and S1D). However, post-exercise lactate levels were elevated after PWT in iSMNKO mice (Figures 2B [left] and S1D). Despite this, peak oxygen consumption (VO_{2peak}) and related parameters (distance to VO_{2peak} and RER during GRMT) remained unaffected (Figure 2B, right), confirming that muscle NAD depletion does not impair exercise tolerance.

Exercise-induced energetic stress is greater in skeletal muscle of iSMNKO mice

Following moderate-intensity exercise, iSMNKO mice exhibited higher blood lactate levels despite a similar increase across genotypes (Figure 2C, left). At rest, iSMNKO quadriceps (QUAD) contained 20% more glycogen, yet during exercise, glucose uptake and glycogen utilization matched WT levels (Figure 2C, center). Elevated AMP levels indicated greater energetic stress in iSMNKO muscle, though AMP-activated protein kinase (AMPK) γ1- or γ3-complex activation remained unchanged (Figure 2C, right). Furthermore, the dynamics of muscle AMPK-γ1/γ3 activities were independent of NAD availability, with similar activity at exercise completion and a return to basal levels within 20 min post exercise (Figure 2D, left). 5-Aminoimidazole-4-carboxamide ribonucleotide (AICAR) is a pharmacological activator of AMPK, which increases muscle glucose uptake in an AMPK-γ3-dependent manner.[32–34] To further examine the activation of AMPK-γ3 complex in the context of low muscle NAD, we assessed the ability of AICAR to lower blood glucose in iSMNKO mice but found no difference between the genotypes in this endpoint (Figure 2E).

iSMNKO skeletal muscle utilizes higher quantities of glycogen during contraction

Muscle glycogen content is rapidly restored after an exercise bout. In both WT and iSMNKO, QUAD and gastrocnemius (GAS) glycogen levels were nearly fully restored within 20 min of recovery, unlike that of the liver (Figure 2D, right). To assess whole-body glucose oxidation after an hour-long moderate-intensity exercise (Figure 2F), we used uniformly labeled ^{13}C glucose and a stable isotope analyzer combined with indirect calorimetry. While at rest, there was no effect on ^{13}C-labeled CO_2 release rates (Figures 2F [left] and S1E); they were decreased by exercise only in iSMNKO mice, which indicates lower glucose oxidation and higher rates of glycogenesis during recovery. However, this had no influence on RER and EE in the hours and days following the exercise (Figure S1F). To further investigate the regulation of muscle glycogen metabolism in the iSMNKO mice, we used *in situ* muscle contraction, which is based on electrical stimulation of the sciatic nerve and offers tight control over the contraction duration and intensity. In WT and iSMNKO EDL and TA, contraction reduced glycogen levels to the same extent (Figure 2G). However, contracted iSMNKO muscles utilized on average ∼50% more glycogen than WT (Figure 2G). Liver and SOL glycogen stores were unaffected by the stimulation (Figure S1G). Next, we determined whether the increased glycogen utilization of the iSMNKO muscle during contraction was followed by elevated glucose uptake during recovery (Figure 2H). In three out of four tested muscle groups, the amount of glucose transported into the muscle within the first 20 min after contraction was comparable between the genotypes (Figure 2H). However, in EDL, glucose uptake was increased in iSMNKO compared with the WT mice (Figure 2H). To directly assess glycogen content and rate of its resynthesis,

Figure 2. iSMNKO mice have intact exercise capacity despite an altered metabolic response to acute exercise

(A) Voluntary wheel running distance, average speed, and net cost of transport (NCOT) of WT and iSMNKO mice (10 days) ($n = 8$).

(B) Exercise performance in treadmill running power test (PWT), graded maximal running test (GMRT), blood glucose and lactate levels after PWT, and VO_2 peak and gas exchange rates during GRMT.

(C) Metabolic response to a moderate-intensity exercise in WT and iSMNKO mice: blood lactate and QUAD glycogen post-exercise, 2-deoxyglucose (2-DG) uptake during exercise, QUAD concentrations of adenosine phosphates, and activity of AMPK complexes.

(D) Metabolism during post-exercise recovery: AMPK complex activity in QUAD, muscle, and liver glycogen contents.

(E) 5-Aminoimidazole-4-carboxamide ribonucleotide (AICAR) tolerance test (ZT2–6) ($n = 8$–10).

(F) Whole-body ^{13}C-labeled CO_2 release ($n = 5$–6) and EE and RER after 1 h of exercise, moderate speed ($n = 8$).

(G) Muscle (EDL, TA) glycogen levels immediately after *in situ* contraction and total amount of glycogen utilized for contraction.

(H) *In situ* muscle (EDL, TA, SOL, and GAS) glucose uptake after contraction.

(I) Glucose, levels of ^{14}C-glucose, and specific activity of tracer in blood during measurements of glycogen resynthesis rates in EDL, TA, SOL, and GAS after *in situ* contraction. Glycogen levels in the indicated muscles 30 min after termination of *in situ* muscle contraction.

Mean values are plotted. Error bars represent SEM. Statistical significance was tested by unpaired two-tailed Student's t test or two-way ANOVA with Holm-Šídák post hoc test (genotype effect, $^{*}p < 0.05$, $^{**}p < 0.01$, $^{***}p < 0.001$, $^{****}p < 0.0001$; running/contraction effect, $^{\#}p < 0.05$, $^{\#\#}p < 0.01$, $^{\#\#\#}p < 0.001$, $^{\#\#\#\#}p < 0.0001$). The mice were male and 15–20 weeks of age.

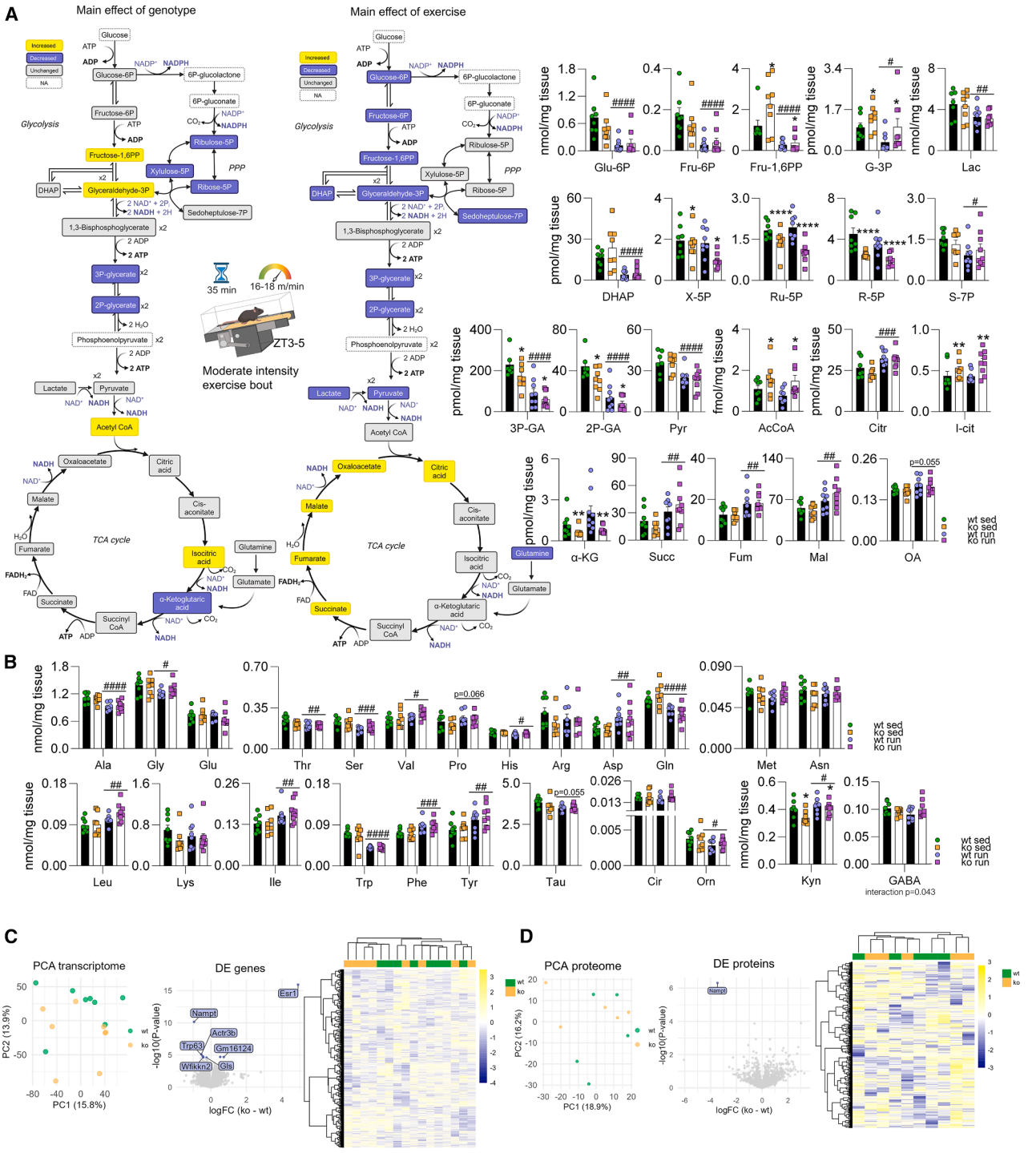

Figure 3. Muscle gene expression and oxidative metabolism are robust to NAD depletion

(A) Schematic of glycolysis, tricarboxylic acid cycle (TCA), and oxidative pentose phosphate pathway (PPP): main effect of genotype (left) and main effect of exercise (right) in QUAD of WT and iSMNKO at rest and after running (blue, decreased; yellow, increased; gray, unchanged; white, undetected). Concentrations of individual metabolites are shown in the right panel.

(B) Concentrations of amino acids in QUAD of WT and iSMNKO mice at rest and after running.

(C and D) Transcriptome (left) and proteome (right) of WT and iSMNKO QUAD: principal-component analysis (PCA), differentially expressed genes/proteins, and heatmaps of transcripts/proteins showing mean *Z* scores.

(legend continued on next page)

we measured the incorporation of radioactively labeled glucose into glycogen. Although glycogen resynthesis rates were similar between the genotypes, iSMNKO muscles did not reach their pre-contraction levels within the first 30 min of recovery (Figure 2I). Overall, these data show that iSMNKO mice have elevated levels of basal muscle glycogen, which is depleted to a greater extent during contraction. Nevertheless, the glycogen synthesis rate in the minutes after contraction is not limited by lowered muscle NAD. Taken together, the increased glycogen availability may be an adaptation of iSMNKO muscle, which allows it to maintain its functional capacity.

Major branches of muscle oxidative metabolism are resilient to decreased NAD availability

Targeted metabolomics revealed similar levels of most glycolytic and tricarboxylic acid cycle (TCA) intermediates in QUAD muscle across genotypes (Figure 3A). However, iSMNKO muscle exhibited increased fructose 1,6-biphosphate (Fru-1,6PP) and glyceraldehyde 3-phosphate (G-3P) concentrations alongside reduced 3- and 2-phospho glycerate (3P-GA and 2P-GA) levels. Acetyl coenzyme A (CoA) (AcCoA) and isocitrate (I-cit) levels were elevated, whereas the amount of α-ketoglutarate (α-KG) was reduced in iSMNKO muscle, independent of exercise (Figure 3A). Similarly, pentose phosphate pathway (PPP) intermediates ribulose 5-phosphate (Ru-5P), xylulose 5-phosphate (X-5P), and ribose 5-phosphate (R-5P) were reduced in the iSMNKO muscle (Figure 3A). Exercise affected amino acid concentration, glycolysis, TCA, and PPP intermediates similarly in both genotypes (i.e., main effects of exercise) (Figures 3A and 3B).

iSMNKO and WT mice have comparable muscle transcriptomic and proteomic profiles

To obtain a global and unbiased overview of the processes affected by the loss of 85% of muscle NAD, we utilized RNA sequencing (RNA-seq) and mass spectrometry (MS)-based proteomics. Remarkably, WT and iSMNKO muscle had almost identical transcriptomic and proteomic profiles (Figures 3C and 3D). One protein (i.e., NAMPT) and a few genes, which were differentially expressed in iSMNKO muscle, were the transgenic components used to create the model (i.e., *Nampt* and *Esr1*). Other affected transcripts included two predicted genes (*Gm16124* and *Gm11613*), *Trp63*, *Wfikkn2*, and *Gls*, none of which are highly expressed in murine skeletal muscle compared with other tissues.

Muscle mitochondria lacking 50% of their NAD pool are fully functional

Considering that NAD plays a pivotal role in mitochondrial oxidative metabolism, we characterized the mitochondrial function of skeletal muscle fibers from sedentary iSMNKO mice. Surprisingly, oxygen consumption rates (OCRs) were maintained in the iSMNKO fibers despite an ∼50% lower mitochondrial NAD^+ content (Figures 4A and 4B). This was true for both coupled complex I (CI) and I + II (CI + II) respiration of type II (QUAD) and type I (SOL) fibers. The ratio of mitochondrial to genomic DNA content as well as the levels of muscle citrate synthase (CS) activity were preserved in iSMNKO mice, indicating that the number of mitochondria was unchanged compared with WT littermates (Figures 4C and S2A). In addition, expression of the mitochondrial NAD^+ transporter *Slc25a51* was also not affected by genotype (Figure 4D). Considering the stimulating effect of muscle contraction on mitochondrial metabolism and function, we studied the key aspects of mitochondrial characteristics in both basal (sedentary) and stimulated (post exercise) states. As such, NAD-depleted iSMNKO mitochondria from both sedentary and acutely exercised mice demonstrated blunted OCR responses to small ADP boluses, while having normal rates of coupled respiration with high ADP (Figures 4E and S2C). In particular, the respiration induced by 0.01, 0.05, and 0.1 mM ADP was lower in the iSMNKO mitochondria. Acute exercise did not affect OCR regardless of genotype and ADP concentration, except that it lowered the total oxygen consumed to phosphorylate the 0.1 mM ADP bolus specifically in WT mitochondria (Figure S2D). In accordance with the OCR data, IMMP was unchanged in iSMNKO mitochondria (Figures 4E and S2E–S2G). In contrast to the lack of exercise effect on OCR, running increased the maximal IMMP generated by CI + II-linked electron transport and the rate of ATP synthesis by about 10% and 40%, respectively (Figure 4E). The decrease in OCR observed in NAD-depleted mitochondria at low ADP concentrations may be associated with a decrease in IMMP, as differences in IMMP between the genotypes coincided with the differences in OCR at low ADP concentrations (Figure S2H). Additionally, in the same experiment, CS activity, measured in isolated mitochondria, increased by 35% in response to acute exercise but only in samples from WT mice (Figure S2B). Although after exercise CS activity was the same in both genotypes, it was elevated in the mitochondria from the non-exercised iSMNKO muscle. To explain these differences in CS activity, we measured the expression of peroxisome proliferator-activated receptor-gamma co-activator 1 alpha (*Ppargc1a*), a transcriptional co-activator known to regulate mitochondrial biogenesis. *Ppargc1a* mRNA, together with the expression of mitochondrial fission and fusion genes, remained unchanged (Figure 4D). Taken together, these data suggest that although the number of mitochondria in the iSMNKO muscle is unchanged, the activity of some mitochondrial enzymes, such as CS, is affected by *Nampt* ablation.

Computational modeling corroborates that a 50% decrease in mitochondrial NAD content does not cause respiratory dysfunction

Although most reports of the NAD-deficient models describe a direct causal relationship between reduced cellular NAD content and mitochondrial dysfunction,[9,25,35–37] our data do not support this notion. Therefore, we aimed to determine the level at which NAD would be limiting respiration. We used a computational model of mitochondrial respiration and bioenergetics[38] and

Data are presented as mean values ± SEM. For transcriptomics and proteomics data, statistical significance was tested by unpaired two-tailed Student's t test, gene expression and protein abundances are presented as logFC (fold change) of KO over WT, and *p* values are FDR-adjusted using Benjamini-Hochberg method. For targeted metabolomics data, two-way ANOVA with Holm-Šídák post hoc test was used (genotype effect, $^{*}p < 0.05$, $^{**}p < 0.01$, $^{****}p < 0.0001$; running effect, $^{\#}p < 0.05$, $^{\#\#}p < 0.01$, $^{\#\#\#}p < 0.001$, $^{\#\#\#\#}p < 0.0001$). Mice were male and 15–20 weeks of age.

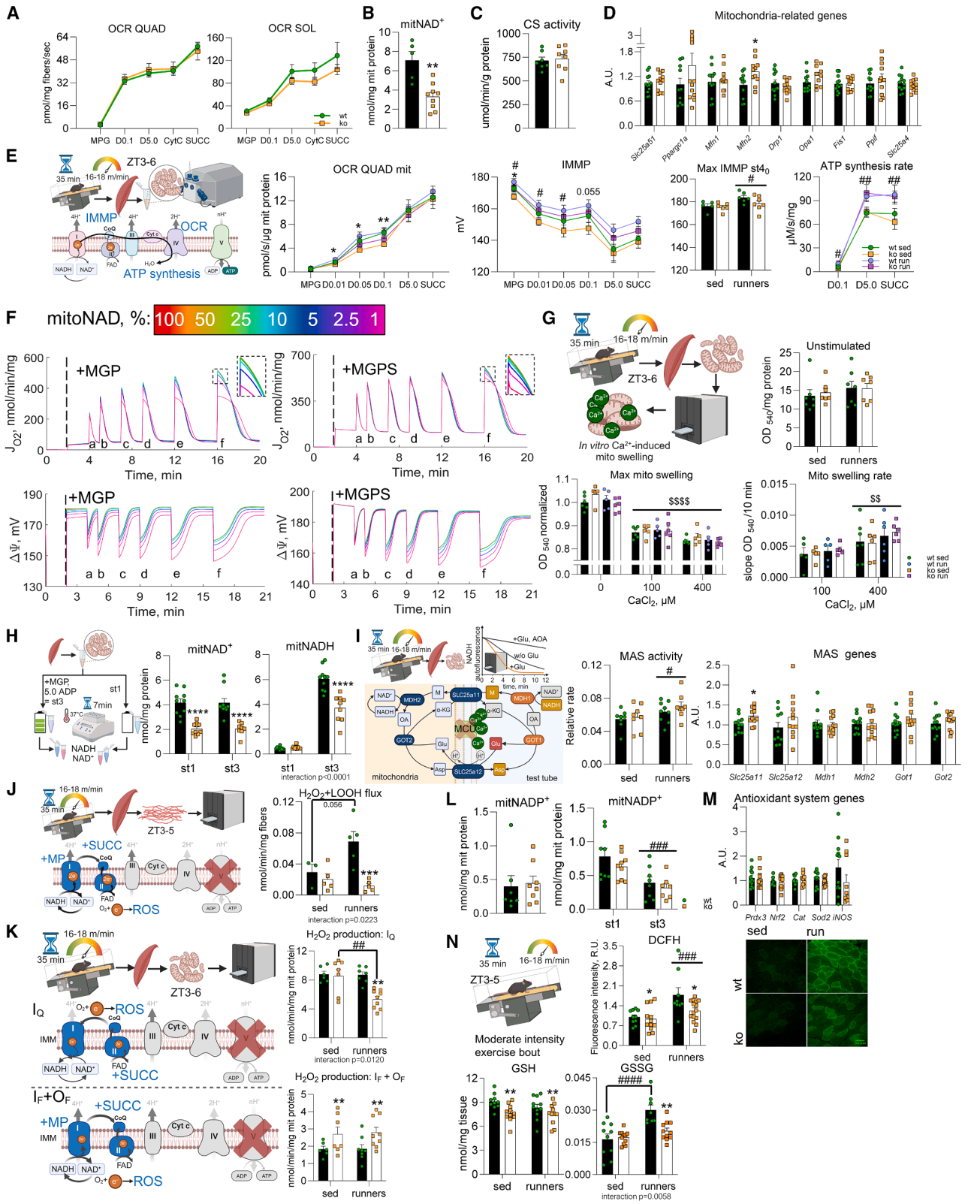

Figure 4. 50% lower muscle mitochondria NAD content does not compromise respiration but alters ROS production capacity

(A) Muscle (QUAD and SOL) oxygen consumption rates (OCRs) with substrates for CI (malate, glutamate, and pyruvate: MGP) and CI + II (MGP + succinate [SUCC]); 0.1 and 5 mM ADP (days 0.1 and 5.0) (n = 7–9).

(legend continued on next page)

evaluated OCR as well as IMMP with either CI or CI + II substrates across a range of NAD and ADP concentrations (Figure 4F). Modeling demonstrated that a 50% reduction in mitochondrial NAD had no impact on OCR and IMMP, aligning with our experimental findings. Even at 10% of normal NAD levels, CI-driven respiration rates and IMMP were only mildly reduced. A 99% depletion of mitochondrial NAD was necessary to elicit a 50% decrease in ORC. When both CI and II were fueled, respiration and IMMP exhibited even greater resilience to NAD depletion.

Ca^{2+}-induced mitochondrial swelling is not affected in iSMNKO mice

Considering the importance of Ca^{2+} for mitochondrial metabolism, and motivated by previous findings on the crucial role of NAMPT and NAD in the regulation of Ca^{2+}-induced mitochondrial permeability transition pore (mPTP) opening,[29] we assessed the extent of mitochondrial swelling in response to Ca^{2+} in mitochondria isolated from iSMNKO mice and WT littermates. Mitochondrial swelling in the absence of exogenous Ca^{2+} (basal) was unaffected in either sedentary or exercised iSMNKO mice (Figure 4G). The maximal level, as well as the rate of swelling in the presence of either 100 or 400 μM of Ca^{2+}, was unaltered. Because mPTP opening is at least partially responsible for the calcium-induced mitochondrial swelling, we assessed *Ppif* and *Ant1* (*Slc25a4*) expression levels that constitute the mPTP but found no differences between genotypes (Figure 4D).

Mitochondria from iSMNKO muscle generate less NADH but maintain normal MAS activity

We hypothesized that the functional robustness of NAD-depleted mitochondria could be attributed to their ability to sustain NADH levels. To test this, we incubated isolated mitochondria from both genotypes with (state 3) or without (state 1) CI substrates and measured NAD^+ and NADH contents. Actively respiring mitochondria from iSMNKO mice exhibited ∼40% lower NADH levels compared with WT (Figures 4H and S2I). We also assessed malate-aspartate shuttle (MAS) activity, which transfers reducing equivalents from cytoplasmic NADH to mitochondrial NAD^+. MAS activity in QUAD mitochondria increased similarly in both genotypes after acute exercise, with no genotype differences in MAS activity or gene expression (Figure 4I).

ROS production capacity is altered in iSMNKO mitochondria

ROS production is a part of normal mitochondrial function. ROS produced both inside and outside mitochondria play an important role as redox mediators in cellular signaling.[39–41] First, we characterized the rate of ROS production in muscle fibers under IMMP-maximizing conditions using a lipid-hydroperoxide- and hydrogen-peroxide-sensitive dye, Amplex UltraRed.[42] Muscle fibers from sedentary mice had comparable hydrogen and lipid hydroperoxide production rates irrespective of the presence of NAMPT (Figure 4J). However, only the WT fibers showed the expected increase in ROS generation post exercise[43] (Figure 4J). Next, we focused on ROS production at specific ETC sites (Figure 4K). At the quinone-binding site of CI (I_Q), ROS production was assessed under the reverse electron transport (RET) conditions. The rates were comparable between genotypes at rest but decreased after acute exercise in iSMNKO mitochondria (Figure 4K). In contrast, the maximal flux of H_2O_2 at the flavin (I_F) and 2-oxoglutarate dehydrogenase (O_F) sites of CI was 30% higher in the iSMNKO mitochondria regardless of exercise (Figure 4K). The iSMNKO mitochondrial $NADP^+$ levels were unchanged in the sedentary state (Figure 4L).

Given that reduced cytoplasmic NADP levels may limit NOX activity,[44] we measured total ROS abundance in iSMNKO muscle sections by dichlorodihydrofluorescein (DCFH) staining. The results showed that exercise increased DCFH fluorescence in WT and iSMNKO muscle, with the level being generally lower in the latter (Figure 4N). To characterize the redox system of iSMNKO muscle further, we assessed concentration of GSH, which is one of the main antioxidant components (Figure 4N). We found that it was significantly lower in the iSMNKO muscle independent of exercise. On the other hand, although similar at rest, exercise increased the level of glutathione disulfide (GSSG) only in the WT muscle (Figure 4N). The gene expression of antioxidant enzymes *Prdx3*, *Cat*, *Sod2l*, and *Nrf2* did not differ between the genotypes (Figure 4M).

(B) NAD^+ in mito fraction isolated from QUAD of rested WT and iSMNKO mice.
(C) Activity of citrate synthase (CS) measured in WT and iSMNKO QUAD homogenates.
(D) Expression of mitochondrial genes in WT and iSMNKO GAS.
(E) Functional tests (respiration, inner mitochondrial membrane potential [IMMP], and ATP synthesis rate) performed on QUAD mitochondria from rested and acutely exercised animals (n = 7–9).
(F) OCR and IMMP modeled for a range of mitochondrial NAD (250–2 μM [100%–1%]) and ADP (25, 50, 75, 100, 150, and 250 μM, A–F) concentrations with MGP (left) and MGP + SUCC (right); lines colors indicate mito NAD concentrations (rainbow legend).
(G) QUAD mitochondrial Ca^{2+}-induced swelling in sedentary and exercised mice: basal and maximal response and swelling rate.
(H) NAD contents of QUAD mitochondria incubated with (state 3) and without (state 1) respiratory substrates (MGP, day 5.0).
(I) MAS activity in mitochondria from sedentary and exercised mice (left) and MAS-component gene expression in GAS of WT and iSMNKO mice (right).
(J) H_2O_2 and lipid hydroperoxide (LOOH) production rate in QUAD muscle fibers after exercise.
(K) Max rates of H_2O_2 production at CI quinone (I_Q) (top) and flavine (I_F) + 2-oxoglutarate dehydrogenase (O_F) sites (bottom) in muscle mitochondria from rested and exercised mice.
(L) QUAD mitochondria $NADP^+$ content in basal (left), state 1, and state 3 (right) conditions.
(M) mRNA levels of antioxidant defense genes in WT and iSMNKO GAS.
(N) Total ROS abundance detected with dichlorodihydrofluorescein (DCFH) diacetate staining on TA sections of rested and exercise mice (left). Scale bar, 50 μm. QUAD concentrations of GSH and GSSG at rest and after running (right).
Mean values ± SEM are plotted. Statistical significance was tested by unpaired two-tailed Student's t test or two-way ANOVA with Holm-Šídák post hoc test (genotype effect, $^*p < 0.05$, $^{**}p < 0.01$, $^{***}p < 0.001$, $^{****}p < 0.0001$; effect of running, $^{\#}p < 0.05$, $^{\#\#}p < 0.01$, $^{\#\#\#}p < 0.001$, $^{\#\#\#\#}$i < 0.0001; effect of Ca^{2+}-loading, $^{\$\$}p < 0.01$, $^{\$\$\$\$}p < 0.0001$). The mice were male and 15–20 weeks of age.

CellPress
OPEN ACCESS

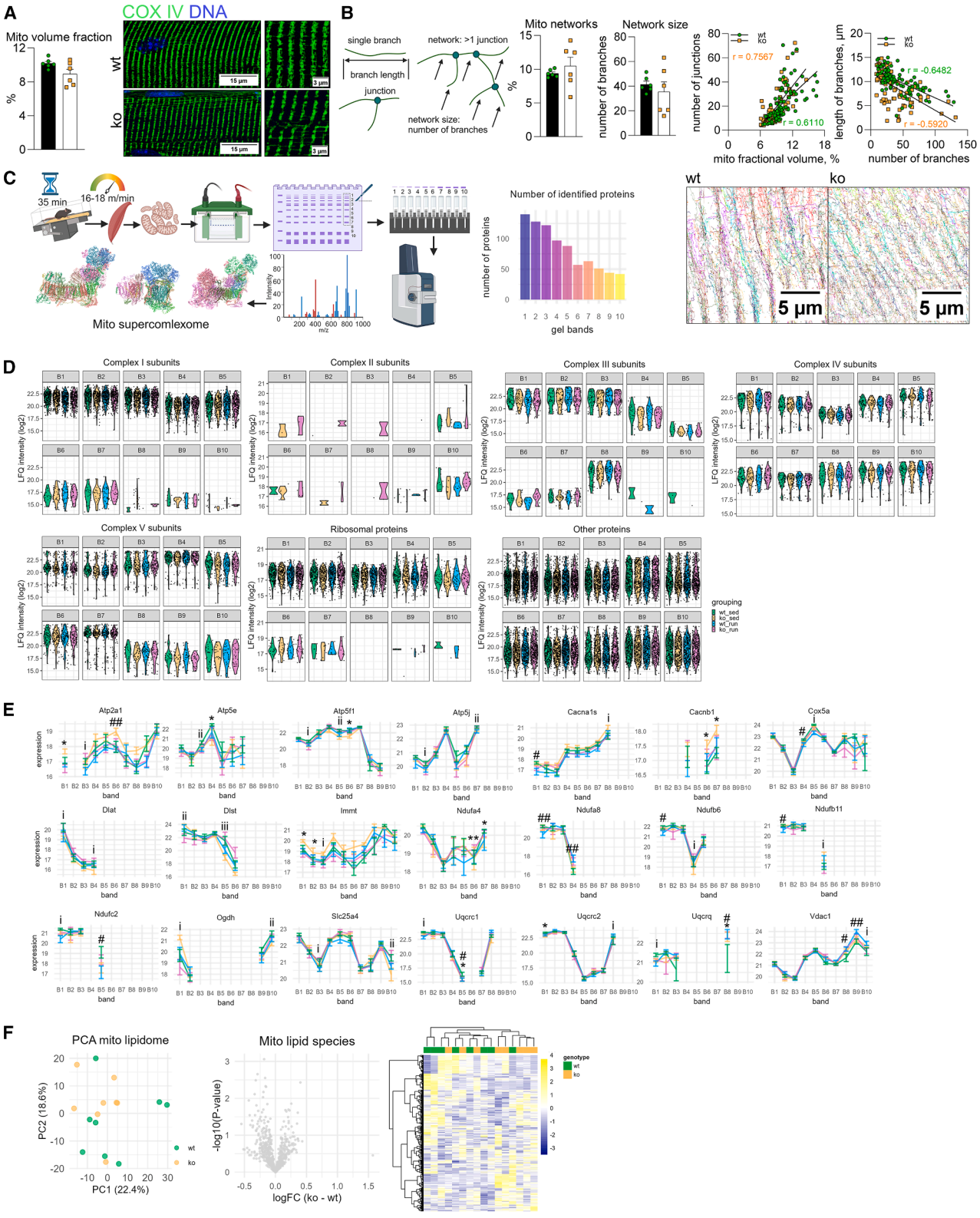

Figure 5. NAD depletion does not affect the structure of muscle mitochondria networks, membranes, and respiratory supercomplexes

(A) Mean fractional volume of mitochondria in QUAD fibers of control and iSMNKO mice and representative pictures of mito networks (immunolabeled COXIV in green, nuclei in blue; scale bar length, 15 µm [left] and 3 µm [right]).

(legend continued on next page)

The mitochondrial network is preserved in iSMNKO muscle

Mitochondria in skeletal muscle form dynamic networks that adapt to their structural organization in response to metabolic challenges. To assess the resilience of mitochondrial structure to NAD depletion, we analyzed mitochondrial networks in the QUAD of sedentary iSMNKO and WT mice. Using fluorescent antibody labeling of mitochondria (COXIV), we obtained super-resolution images of mitochondrial networks (Figures 5A, 5B, and S2J). Quantitative analysis revealed that mitochondrial volume, abundance, complexity, and network size were comparable between iSMNKO and WT muscle fibers (Figures 5A and 5B).

MSC composition and lipidome are unaffected in rested and exercised iSMNKO mice

Mitochondrial respiratory complexes assemble in composite macrostructures known as mitochondrial supercomplexes (MSCs). Interactions between proteins of respiratory complexes and their inclusion into MSCs are thought to be important for the dynamic fine-tuning of mitochondrial fitness.[45–48] Reduced electron leak and augmented production of ROS are associated with optimized mitochondrial functionality. Thus, the altered ROS generation of the iSMNKO mitochondria motivated us to study MSCs. Recently, using a combination of native gel electrophoresis and MS, we have characterized the MSCs composition of mitochondria in response to exercise training.[49] Here, we applied a similar approach to study MSCs composition at basal and activated (acute exercise) states (Figure 5C). The number of identified proteins in the different bands (e.g., 143 for band 1) was similar to the observations published previously[49] (Figure 5C). In agreement with published data, the majority of CI and complex III (CIII) subunits were distributed primarily between the higher molecular weight (MW) bands 1–3, which contain most of the MSCs (Figure 5D).[49] At the same time, our results did not support the proposed integration of complex II into MSCs as we did not detect it in bands 1–4 (Figure 5D). As for complex IV (CIV), we mapped its subunits to bands 1 and 2, where they are likely to be a part of respirasomes. The second and third peaks of CIV abundance were detected in bands 5–6 and bands 8–10, which replicates our earlier observations.[49] On the other hand, the distribution of complex V (CV) subunits was not limited to the lower MW bands as shown before. Instead, in the current dataset, proteins belonging to CV were represented in all analyzed gel bands, although being most abundant in bands 3–7.

Focusing on the individual subunits, we aimed to find proteins that had changed their relative abundance in more than one band. This could be indicative of them shifting between MSCs rather than changing their total abundance. If evident, such modifications could represent the most dynamic part of the MSCs modulation. Here, we identified 21 proteins that were differentially abundant in at least two out of 10 bands for either of the interventions (genotype, exercise, or their interaction) (Figure 5E). However, none of these proteins followed a pattern of redistribution between the tested conditions (i.e., being increased in a low MW band and decreased in a high MW or vice versa). Thus, these data demonstrate that although a 50% lower mitochondrial NAD content is associated with altered formation of ROS, it did not change the molecular organization of respiratory complexes. Furthermore, the activation of mitochondrial metabolism resulting from the increased energetic demands of exercise did not involve major modification of MCSs composition and abundance. Lastly, considering the high importance of mitochondrial membrane lipids for respiratory complex stability and ROS production, we performed an untargeted analysis of mitochondrial lipids of WT and iSMNKO muscle mitochondria (Figure 5F). We identified 735 lipid species, none of which were changed in iSMNKO mice.

Lifelong muscle NAD depletion does not compromise whole-body metabolic fitness in iSMNKO mice

Our comprehensive characterization of adult iSMNKO mice demonstrates that muscle NAD depletion is well tolerated, with no adverse effects on muscle function, exercise capacity, or metabolic health. However, whether chronic NAD deficiency exacerbates age-related decline remains unknown. To address this, we examined old iSMNKO mice (Figure 6A). Body weight and composition were comparable between genotypes, with both WT and iSMNKO mice gaining weight primarily through increased fat and free fluid content (Figure 6A). Although aging reduced QUAD NAD^+ levels by 10% in WT mice, consistent with previous reports,[50,51] its content in iSMNKO muscle remained unchanged (Figure 6B). Among NAD-derived metabolites, only ADPR decreased with age and was consistently lower in iSMNKO muscle (Figure 6C). Accordingly, ADP-ribosylated protein abundance was reduced in iSMNKO muscle regardless of age (Figure 6D), suggesting lower NAD-cleaving ADP-ribosyltransferase activity. In contrast, global protein acetylation, regulated in part by NAD-dependent deacylases, remained unchanged (Figure 6D).

(B) Mito network image analysis. Scheme illustrating the terms (left) and readouts (right): abundance of networks, their average size and complexity, and representative pictures of skeletonized mito networks with labeled components (bottom). Scale bar length, 5 μm (n = 6; average of 3 random locations, 15 single fibers/mouse).

(C–E) Blue native (BN)-PAGE MS-based supercomplexome analysis of muscle mitochondria from sedentary and exercised control and iSMNKO mice.

(C) Number of identified protein groups in analyzed gel bands (n = 8–9).

(D) Distribution of oxidative phosphorylation and ribosomal and other proteins across the gel bands; protein abundance is presented as $\log_2$-transformed label-free quantification (LFQ) intensities, normalized to total LFQ intensity for each band. Violin plot shape illustrates the data distribution in each of the experimental groups with dots showing individual protein groups.

(E) Expression profiles ($\log_2$) of individual proteins differentially abundant in >1 of the analyzed gel bands (effect of exercise, genotype, or both).

(F) Muscle mitochondrial lipids (n = 8): PCA plot, differential abundance plot, and heatmap of all detected lipid species annotated with high certainty shown as mean Z scores.

Data are presented as mean values ± SEM. For mitochondrial complexome, statistical significance was tested by unpaired two-tailed Student's t test and two-way ANOVA, protein abundances are presented as logFC (fold change) of KO over WT (E: raw p values are shown [genotype effect, $^{*}p < 0.05$, $^{**}p < 0.01$; exercise effect, $^{\#}p < 0.05$, $^{\#\#}p < 0.01$; interaction, $^{i}p < 0.05$, $^{ii}p < 0.01$, $^{iii}p < 0.001$]). For lipidomics data (F), unpaired two-tailed Student's t test and p value correction with Benjamini-Hochberg method were used to determine statistical significance. The mice were male and 15–20 weeks of age.

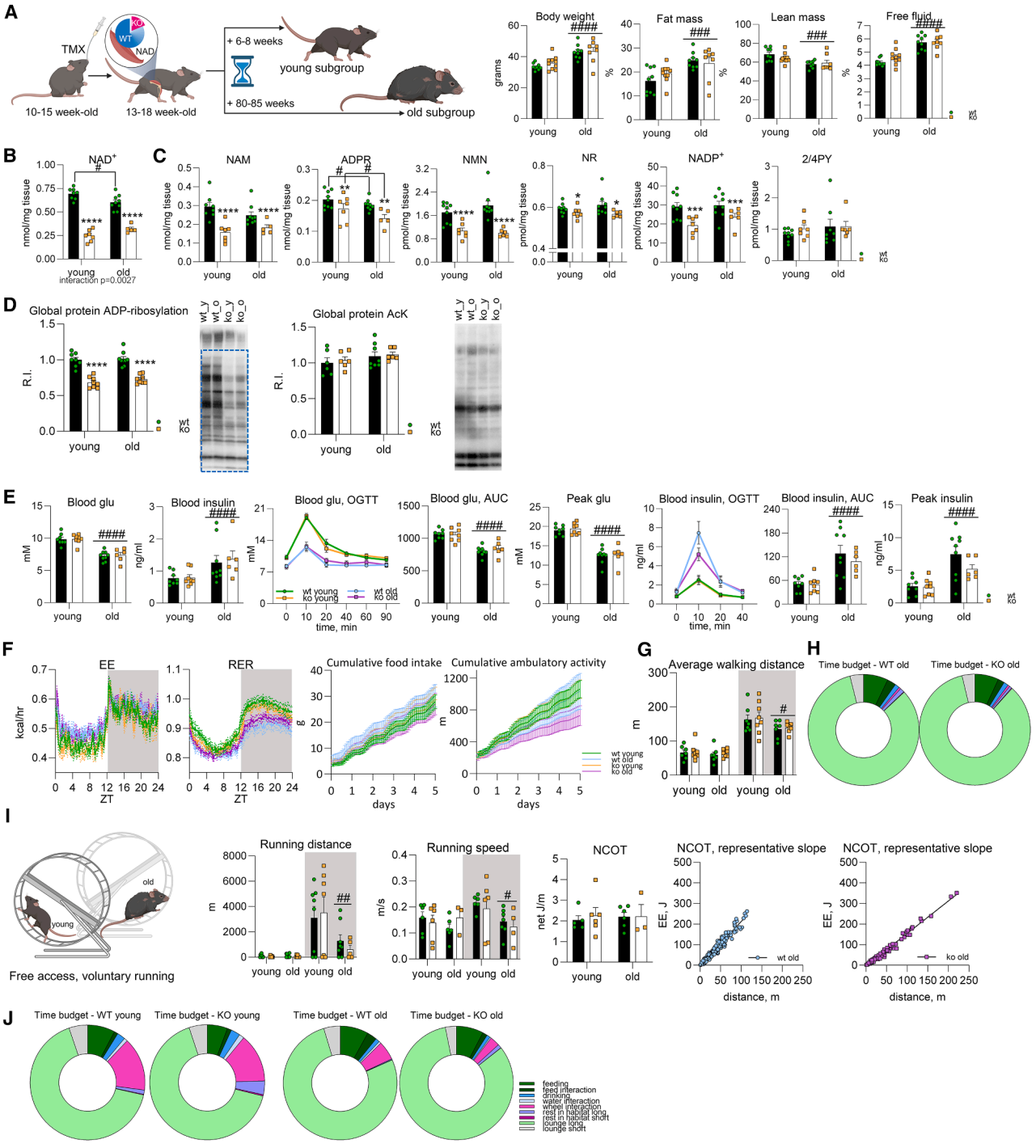

Figure 6. Effect of aging on muscle function is independent of muscle NAD content

(A) Aging experiment setup (left). Body weight and composition of young and old WT and iSMNKO mice (right).

(B) QUAD NAD^+ content determined via cycling assay.

(C) QUAD NAD-related metabolites measured with HPLC-MS (QQQ).

(D) Levels of global protein ADP-ribosylation and lysine acetylation in QUAD.

(E) Oral glucose tolerance test (OGTT): basal blood glucose and insulin levels (left), blood glucose and insulin during OGTT, and corresponding areas under the curve and peak values (center and right) (n = 6–9).

(F) Average EE and RER across 24 h (5 days) (left), cumulative food intake, and activity in young and old WT and iSMNKO (n = 8–9).

(G) Ambulatory activity levels during light and dark phases.

(H) Pie chart of home-cage behavior (see legend in J) of aged WT and iSMNKO mice (5 days average) (n = 7–8).

(legend continued on next page)

To assess metabolic regulation, we conducted an oral glucose tolerance test (OGTT) (Figure 6E). Aged mice exhibited slightly elevated fasting insulin levels and modestly reduced fasted glucose concentrations. Both genotypes displayed similar glucose and insulin responses to a glucose challenge. Notably, older mice displayed improved glucose tolerance, as indicated by lower glucose peaks and AUC, likely due to enhanced insulin secretion (Figure 6E), consistent with previous findings.[52] These trends were also observed in aged female mice (Figure S3A), suggesting that glycemic regulation is maintained by moderate hyperinsulinemia, independent of muscle NAD content.

Metabolic assessments revealed decreased RER and increased EE in aged mice of both genotypes (Figures 6F and S3B), with no differences in feeding behavior or cumulative ambulatory activity (Figure 6F). Although dark-phase walking distance declined with age (Figure 6G), overall activity patterns were similar across groups (Figure 6H). To evaluate voluntary exercise, we provided animals with free access to running wheels (Figure 6I). Aged mice engaged in substantially less running than younger mice, with no genotype-dependent differences in running distance, speed, or NCOT (Figures 6H–6J).

iSMNKO skeletal muscle does not exhibit signs of accelerated aging

TA morphology analysis revealed that fiber size decreased with age regardless of genotype, with no structural abnormalities or pathological changes observed (Figures 7A and S3C). In addition, we assessed the frequency of myoblast incorporation based on the occurrence of centralized nuclei in TA sections and measured the number of muscle stem cells (MuSCs) via fluorescence-activated cell sorting (FACS). Young iSMNKO mice had a higher percentage of fibers with centralized nuclei compared with WT mice, and this difference was even larger in the old mice (Figure 7B). Despite this increased fraction of fibers with centralized nuclei, MuSC quantity was maintained in muscle of young and old iSMNKO mice (Figures 7C and S3D), suggesting that lifelong NAD depletion stimulated myoblast-myofiber fusion but did not exhaust the proliferative capacity of muscle progenitor cells.

Mitochondrial dysfunction is a hallmark of aging-related muscle decline.[53] Therefore, it was important to evaluate the mitochondrial function in aged iSMNKO muscle fibers, as they may have accumulated more damage throughout their lifetime, which could be detected by a mitochondria-focused assay. Strikingly, neither age nor NAD status influenced CI and CI + II OCRs (Figure 7D). Proteomic analyses of QUAD revealed aging as the primary driver of molecular changes, as indicated by the principal-component analysis (PCA), clustering by age rather than genotype (Figure 7E). Aging resulted in 598 differentially abundant proteins, whereas genotype effects were limited to 6 (Figure 7F). No significant genotype-by-age interactions were detected, and hierarchical clustering grouped proteins by age rather than genotype (Figure 7F). Gene set enrichment analysis (GSEA) identified age-related suppression of tissue morphogenesis, development, and fiber organization, alongside upregulation of immune defense and immune response-related processes (Figure 7G). Mitochondrial respiratory complex assembly and organization were among the top downregulated processes in aged muscle. Conversely, genotype effects were limited, with iSMNKO muscle showing enrichment of cell-cycle and division-related proteins. Collectively, aging triggers immune system activation and suppresses tissue growth and mitochondrial maintenance, whereas NAD depletion exerts minimal influence on these changes, indicating no acceleration of muscle aging.

DNA-methylation-based age prediction algorithms, also known as epigenetic clocks, widely used in aging research,[54,55] provide a cumulative marker of biological aging. Muscle NAD depletion did not affect epigenetic aging scores, as both universal and muscle-specific clocks accurately predicted chronological age with no genotype differences (Figure 7H). Although aging iSMNKO muscle exhibited cytosine hypomethylation (Figure 7I), with 805 hypomethylated and 38 hypermethylated loci, these changes did not alter epigenetic age predictions. Thus, lifelong muscle NAD depletion does not accelerate aging at the molecular or functional level.

DISCUSSION

Reduction of NAD content is thought to cause the dysregulation of metabolism, resulting in various disease phenotypes.[6,56–59] In both mice and humans, skeletal muscle NAD content decreases by 10%–30% with age,[60] and NAD abundance positively correlates with muscle fitness.[26,27,61–63] Conversely, our study demonstrates a notable robustness of muscle metabolism and whole-body physiology to a substantial reduction in NAD content. Specifically, although an 85% decrease in NAD achieved via inducible skeletal-muscle-specific knockout of *Nampt* increases the frequency of centrally localized myonuclei occurrence, it does not affect muscle integrity, structure, function, proteome, transcriptome, and aging. Thus, the results of our study suggest that aging-associated muscle NAD decline has a minimal effect on muscle function, aging, and overall healthspan.

In contrast to *Nampt* deletion in adult muscle, embryonic muscle *Nampt* knockout results in aging-like muscle deterioration.[28,29] This striking difference between the models may be attributed to the following two main factors. First, the prolonged presence of nuclear-localized (“active”) CRE recombinase can be detrimental to the targeted tissue due to *loxP*-independent mutagenesis.[64] Notably, *Myh6*-Cre expression in mouse cardiac muscle induces progressive heart dysfunction, detectable at 3 months and worsening by 6 months,[65] a time frame closely matching the degeneration observed in the mNKO model. Because off-target effects of constitutively active CRE were not controlled for in mNKO and SMNKO models, their phenotypes may be at least partly confounded by CRE toxicity. The second factor is the timing of *Nampt* knockout. When deletion occurs embryogenically, NAD depletion also affects developing

(I) Voluntary wheel running test in aged mice: average running distance, speed (left), and NCOT (right) (5 days average).
(J) Pie chart overview of home-cage behavior with free access to running wheels and time distribution (%) (5 days average, $n = 7–8$).
Mean values ± SEM are plotted. Statistical significance was tested by two-way ANOVA with Holm-Šídák post hoc test (genotype effect, $^{**}p < 0.01$, $^{***}p < 0.001$, $^{****}p < 0.0001$; effect of age, $^{\#}p < 0.05$, $^{\#\#}p < 0.01$, $^{\#\#\#}p < 0.001$, $^{\#\#\#\#}p < 0.0001$). The mice were male, 19–26 weeks old (young), and 93–103 weeks old (old).

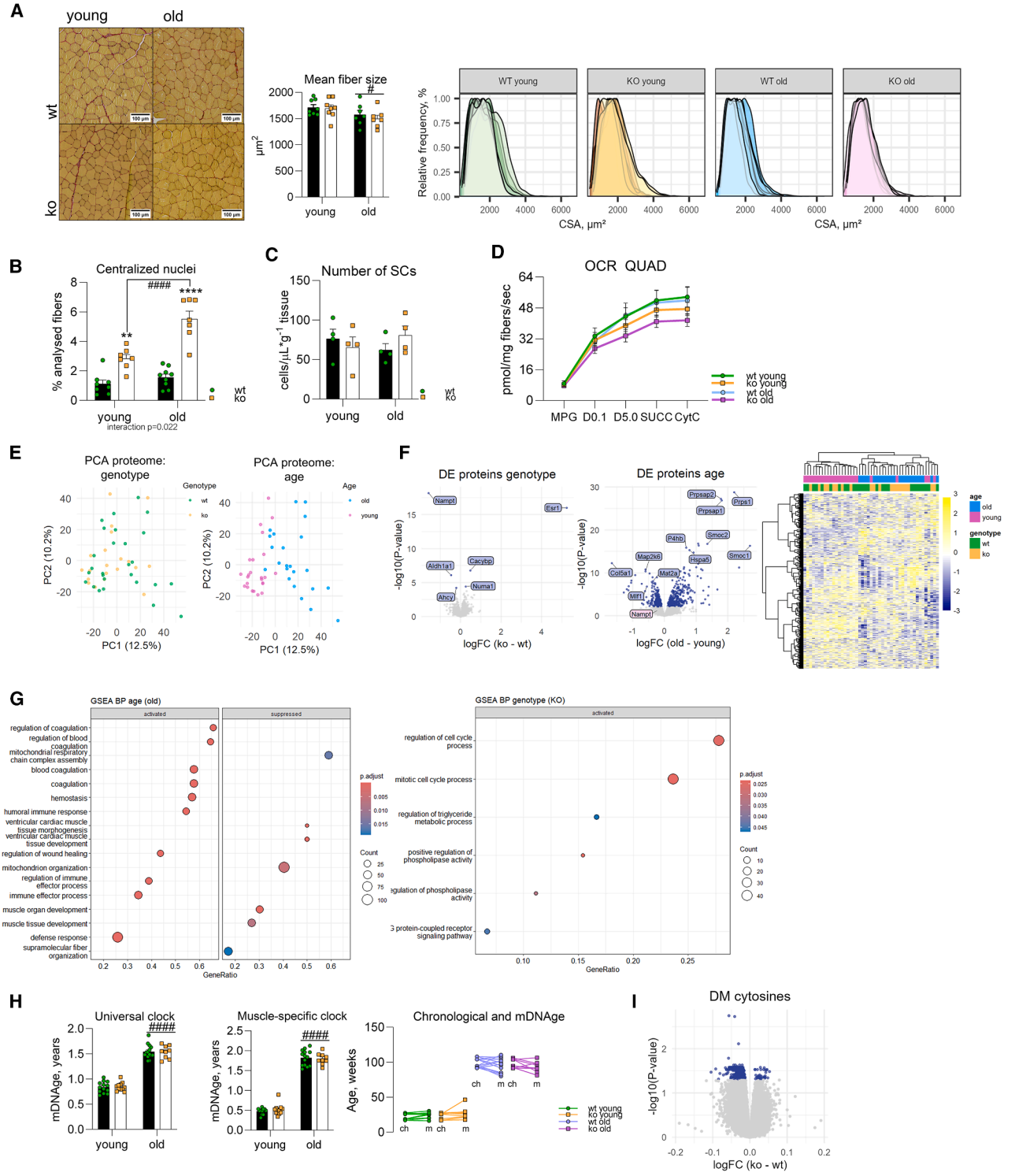

Figure 7. Lowered NAD content does not accelerate muscle aging on a molecular level

(A) Representative images of TA histological sections (PSR; scale bar length, 100 µm) (left), fiber size distributions (center), and mean fiber size (right) (n = 7–8).

(B) Percentage of centralized nuclei in muscle fibers and TA (same images as in A).

(C) Number of progenitor cells (satellite cells [SCs]) in muscle of control and iSMNKO mice (young and old) (n = 4).

(D) QUAD mitochondrial OCR with CI (MGP + days 0.1 and 5.0) and CI + II (+SUCC) substrates (n = 7–8) in young and old WT and iSMNKO mice.

(E–G) QUAD proteome (n = 9–14).

(E) PCA of genotype and aging effects.

(legend continued on next page)

myotubes,[66,67] which may be more vulnerable than mature myofibers. This potential sensitivity, could stem from impaired cell-extracellular-matrix adhesion during early post-natal muscle expansion, possibly linked to attenuated integrin α7β1 ADP-ribosylation.[68,69]

iSMNKO muscle metabolism exhibited only minor modifications. Although a few NAD-dependent reactions were perturbed, no blockage of glycolysis occurred, as all glycolytic intermediates were reduced by exercise regardless of genotype.[28,29] In contracting muscle, NADH generated during glycolysis is re-oxidized to provide energy for mechanical force generation and to sustain glycolytic flux. The recovery of NAD^+ relies on the transfer of reducing equivalents from cytoplasmic NADH into mitochondria via MAS and glycerol-3-phosphate (G3PS) shuttles, as well as the activity of lactate dehydrogenase.[70–72] The latter is particularly active during high-intensity muscle contraction when the rates of MAS and G3PS are saturated.[73] Although the elevated circulating lactate levels in exercised iSMNKO mice may facilitate NAD^+ recovery and help prevent acidosis during sustained muscle contraction, the extent of MAS activation in response to acute exercise was unaffected by genotype.[74,75] However, because the MAS activity assay was conducted in isolated mitochondria, it remains unclear whether the cytoplasmic MAS components respond to NAD depletion.

iSMNKO muscle exhibited higher glycogen content and utilized more glycogen during contraction, which may contribute to the elevated circulating lactate levels. The increased glycogen content in iSMNKO muscle likely necessitates an extended post-exercise resynthesis phase, as the rates of post-contraction glucose uptake and glycogen resynthesis were comparable between genotypes. Our data on post-exercise ^{13}C-labeled CO_2 release and glycogenesis support this hypothesis, although it is also possible that the decreased ^{13}C-labeled CO_2 release in iSMNKO mice is due to label retention in the higher pool of circulating lactate.[76] Further experiments measuring the labeling of glucose, glycogen, and lactate in tissues including blood are needed to explain the effect of NAD depletion on in ^{13}C-labeled CO_2 release.

We did not observe any differences in NCOT between genotypes, despite iSMNKO mice utilizing more muscle glycogen in response to treadmill running and *in situ* contractions. This discrepancy may arise from the methodological limitations of the whole-body indirect calorimetry measurements, which may not detect subtle differences in muscle EE or substrate utilization patterns. Overall, the increased glycogen content appears to be beneficial for muscle function, as we observed reduced fatigue in iSMNKO EDL during repeated tetanic contractions *ex vivo*. Thus, we speculate that the elevated glycogen content in NAD-depleted muscle may be adaptive and could partially account for the unaltered exercise tolerance observed in iSMNKO mice.

Although iSMNKO muscle mitochondria exhibited an ∼50% reduction in NAD^+ level and were capable of generating only ∼60% of WT NADH, their respiratory and ATP generation capacities remained intact, challenging the proposed role of NAD-dependent mitochondrial dysfunction in driving aging.[77] Mitochondrial fitness is characterized by the ability to generate ATP while maintaining appropriate levels of ETC-derived ROS.[41,78,79] Mitochondrial ROS formation is influenced by the reductive state of the ETC, which becomes hyper-reduced under conditions of impaired oxygen consumption or excessive electron supply.[80] Certain sites within the ETC are more potent sources of ROS than others, with the quinol site in CI (I_Q) being dominant under RET and the flavin site in CI (I_F) during aerobic exercise *in vivo*.[81] Because ROS production at both of these sites was affected by NAD depletion and is known to be highly sensitive to IMMP and the redox states of NAD and quinone pools,[82,83] these parameters are most likely altered in iSMNKO mitochondria. Notably, because our assay medium contained auranofin (mitochondrial antioxidants inhibitor), the measurements represent ROS production rate per se. Our findings indicate that mitochondrial NAD depletion alters ROS generation in the absence of MSCs protein composition changes (e.g., CI incorporation), which was shown to affect ROS flux.[84,85] Furthermore, we observed no reorganization of mitochondrial MSCs in response to acute exercise, despite this being a known adaptation to exercise training.[46,49] Our comprehensive MS-based approach provided a detailed characterization of MSCs in both rested and exercised muscles, demonstrating their resilience to NAD depletion.

Although excessive mitochondrial ROS can be damaging, under normal conditions, most ROS in skeletal muscle originates from NADPH oxidases and lipid hydroperoxides rather than mitochondria.[86,87] Notably, exercise-induced ROS elevation is essential for metabolic adaptations to training.[39,88–90] Although iSMNKO muscle exhibited normal hydrogen peroxide and lipid hydroperoxide production at rest, the latter failed to increase post exercise. This suggests that although NAD depletion does not impair exercise tolerance, it may compromise exercise-induced adaptations.

Intracellular ROS abundance is determined by their production and clearance. The latter is dependent on the activity of free radical scavenger systems, which include superoxide dismutase 2 (MnSOD), thioredoxin reductases (TRxs), peroxiredoxin 3 and 5 (Prx3 and Prx5), glutathione peroxidase (GPx), and GRx, as well as tocopherol and GSH.[91–93] We found that muscle NAD depletion resulted in lower GSH levels both at rest and after

(F) Protein DE in old (left) and iSMNKO (center) and hierarchical clustering analysis of all detected proteins (right).
(G) Gene set enrichment analysis (GSEA) of proteins, based on biological processes (BPs) in old (left) and iSMNKO (right) mice.
(H) Epigenetic clock: DNA-methylation-based age predictions for young and old iSMNKO QUAD with Pan2.0 (left) and muscle-specific (center) algorithms. Correspondence between chronological (ch) and epigenetic (methylation [m]) age (right).
(I) Epigenome-wide association study: differentially modified cytosines in QUAD from old iSMNKO mice.
Mean values ± SEM are plotted. Statistical significance was determined with two-way ANOVA and Holm-Šídák post hoc test (genotype effect, $^{**}p < 0.01$, $^{****}p < 0.0001$; age effect, $^{\#}p < 0.05$, $^{\#\#\#\#}p < 0.0001$). Differentially expressed proteins were determined with LIMMA. In short, a linear model with eBayes smoothing was used to test for the main effect of age (old, young), genotype (KO, WT), and their interaction. Multiple hypothesis testing was corrected with Benjamini-Hochberg. The mice were male, 19–26 weeks old (young), and 93–103 weeks old (old).

exercise, suggesting either a reduction in GSH synthesis or an increase in its oxidation or degradation. Given that muscle GSH abundance is reliant on whole-body amino acid homeostasis, it may be altered in iSMNKO mice. Notably, the iSMNKO muscle exhibited no increase in muscle GSSG content following exercise. This observation indicates a lack of exercise-dependent GSH oxidation, potentially attributable to the diminished exercise-induced ROS production in NAD-depleted muscle.

In conclusion, our findings demonstrate that skeletal muscle exhibits markedly greater resilience to NAD depletion than previously thought, as evidenced by morphological, molecular, and functional data. Furthermore, we show that lifelong NAD depletion does not adversely affect overall metabolic health and muscle functionality. These results indicate that different tissues may possess varying sensitivity to NAD depletion, highlighting the necessity for tissue-specific models in the study of NAD metabolism. More broadly, these findings challenge the presumption that NAD deficiency causes aging-associated muscle dysfunction and call for a re-evaluation of the role of NAD in energy metabolism.

Limitations of the study

Our study demonstrates that adult skeletal muscle tolerates NAD depletion, indicating that the previously reported adverse effects of congenital NAD depletion on post-natal muscle health result from disturbed muscle development rather than direct NAD deficiency. However, the specific NAD-dependent processes essential for embryonic muscle development and early post-natal growth remain unidentified and warrant further investigation. Given the similarities between muscle progenitor cell behavior during regeneration and development, muscle regeneration may also be sensitive to NAD depletion, an aspect not addressed in this study.

The resilience of iSMNKO muscle to NAD depletion may arise from either an adaptive response of NAD-dependent processes, inherent insensitivity to NAD levels, or a limited role in core muscle physiology. Although our findings suggest minimal transcriptomic or proteomic adaptation of NAD-consuming enzymes (e.g., ADP-ribosyltransferases and protein deacylases), we assessed only global protein ADP-ribosylation and lysine acetylation rather than specific enzymatic activities.

Finally, although lifelong NAD depletion does not accelerate aging-related muscle decline, it promotes central myonuclei localization, the functional significance of which remains unclear. Additionally, some subtle effects may have been overlooked, as we did not assess muscle force production in aged iSMNKO mice *ex vivo* or evaluate exercise tolerance *in vivo*.

RESOURCE AVAILABILITY

Lead contact

Jonas T. Treebak (jttreebak@sund.ku.dk) is the lead contact and takes full responsibility for the data in this paper. Further information and requests for resources and reagents should be directed to, and will be fulfilled by, the lead contact.

Materials availability

No unique reagents or materials were generated in these studies.

Data and code availability

- All unprocessed data used for plotting the figures and supplemental information in the manuscript are available in Data S1. No proprietary data or code is associated with this manuscript. Any additional information required to reanalyze the data reported in this paper is available from the lead contact upon reasonable request.
- Transcriptomics data: RNA-seq data are available in the Gene Expression Omnibus (GEO): GSE273462.
- DNA methylation data: raw DNA methylation data are available with the GEO: GSE282353. Processed data containing the epigenetic clock predictions are provided in Table S4.
- Lipidomics data: raw lipidomics data are available at Metabolomics Workbench[94] (NMDR): ST003703. Processed data containing the list of lipids detected are provided in Table S5.
- Proteomics data: raw proteomics data are available on Pride Proteome Exchange, PRIDE: PXD061221. Processed data containing protein lists are provided as Tables S6, S7, and S8.

ACKNOWLEDGMENTS

The Novo Nordisk Foundation Center for Basic Metabolic Research (CBMR) is an independent research center at the University of Copenhagen, partially funded by an unconditional donation from the Novo Nordisk Foundation (NNF18CC0034900 and NNF23SA0084103). S.C. was supported by a PhD scholarship from the Copenhagen Bioscience PhD Programme (NNF16CC0020896). J.T.T. was supported by an Excellence Project Award from the Novo Nordisk Foundation (NNF14OC0009315), G.G.L. was supported by a Wellcome Trust Senior Fellowship (104612/Z/14/Z), and J.R.Z. was supported by a Challenge Grant from the Novo Nordisk Foundation (NNF14OC0011493). The authors acknowledge excellent help and support from the Single-Cell Omics Platform, the Rodent Metabolic Phenotyping Platform, and the Metabolomics Platform at CBMR. In addition, we acknowledge the Core Facility for Integrated Microscopy and the Core Facility for Flow Cytometry and Single-Cell Analysis at the Faculty of Health and Medical Sciences, University of Copenhagen, for their technical expertise and support. Mass spectrometry-based proteomics analyses were performed by the Proteomics Research Infrastructure (PRI) at the University of Copenhagen (UCPH), supported by the Novo Nordisk Foundation (NNF19SA0059305). We thank the staff at the Henry Wellcome Building for Biomolecular NMR Spectroscopy at the University of Birmingham for providing access to NMR spectrometers. Finally, we acknowledge the expert help from Robert Brooke and Juozas Gordevicius from the Epigenetic Clock Development Foundation for conducting the biological age prediction analysis by DNA methylation. The graphical abstract and figure schematics were created with BioRender.com.

AUTHOR CONTRIBUTIONS

Conceptualization, S.C. and J.T.T.; investigation and methodology, S.C., I.K., A.M.E., R.M.J., A.L.B., I.K., E.D., D.A., C.Y.Y., S.R.H., K.T., B.S., O.H., R.N.R., J.F.H., F.L.S., S.L., C.H.-O., C.L., D.G., and R.R.; writing – original draft, S.C.; writing – review and editing, all authors provided corrections and comments, and S.C. and J.T.T. prepared the final version of the manuscript; funding acquisition, J.R.Z., Z.G.-H., T.M., K.S., T.E.J., N.J.F., G.G.L., A.S.D., and J.T.T.; project coordination, S.C.; supervision, J.T.T.

DECLARATION OF INTERESTS

J.R.Z. is an advisory board member for *Cell Metabolism*.

STAR★METHODS

Detailed methods are provided in the online version of this paper and include the following:

- KEY RESOURCES TABLE
- EXPERIMENTAL MODEL AND SUBJECT DETAILS
  - Transgenic mouse strains and animal housing
- METHOD DETAILS
  - Body composition

- Treadmill running: acclimation, exercise tolerance test (power test (PWT)), and moderate-intensity exercise bout
- Graded maximal (GRM) exercise performance test
- *In vivo* exercise-induced muscle glucose uptake
- Sable Promethion indirect calorimetry
- TSE indirect calorimetry after an acute exercise bout
- Glucose (oral), AICAR (intraperitoneal) tolerance tests and blood insulin
- *Ex vivo* muscle contractility assay
- ^{13}C-labelled CO_2 release at rest and after exercise
- Mitochondria isolation
- Ca^{2+}-induced mitochondria swelling assay
- Malate-aspartate shuttle activity
- Incubation of mitochondria for NAD assays
- High-resolution respirometry on permeabilized muscle fibers
- High-resolution respirometry on quadriceps mitochondrial fraction with inner mitochondrial membrane potential (IMMP) and ATP synthesis rate
- (Hydro)peroxide production, I_Q + O_F RET and I_F mitochondrial H_2O_2 flux *in vitro*
- Targeted quantification of intermediates of glycolysis, TCA, pentose phosphate pathway and amino acids by combined liquid chromatography tandem mass spectrometry
- Post *in situ* contraction muscle glycogen content, utilization and resynthesis rates
- Single-fiber muscle mitochondria immunofluorescent labeling and super-resolution structured illumination microscopy (SIM) imaging
- RNA extraction and quantitative reverse-transcriptase PCR
- Muscle RNA sequencing
- Glycogen
- NAD^+, $NADP^+$ and NADH assays
- NAD metabolome HPLC-QTOF
- NAD metabolome HPLC-QQQ
- Citrate synthase activity
- Western blot analyses
- DNA extraction and mitochondrial to genomic DNA ratio (mt/nDNA)
- Epigenetic clock and DNA methylation analysis
- Muscle glutathione concentrations
- Nuclear magnetic resonance (NMR)
- Gas chromatography mass spectrometry (GC-MS)
- AMPK activity assay
- Muscle ROS staining
- Muscle histological analysis
- Oxygen consumption rate and mitochondrial inner membrane potential modelling
- Fluorescence-activated cell sorting-based quantification of muscle stem cell number
- Analysis of muscle mitochondria membranes lipid composition
- Proteomics analyses

- QUANTIFICATION AND STATISTICAL ANALYSIS

SUPPLEMENTAL INFORMATION

Supplemental information can be found online at https://doi.org/10.1016/j.cmet.2025.04.002.

Received: October 8, 2024
Revised: February 27, 2025
Accepted: April 8, 2025
Published: April 30, 2025; corrected online: November 5, 2025

REFERENCES

1. Imai, S., and Guarente, L. (2014). NAD^+ and sirtuins in aging and disease. Trends Cell Biol. *24*, 464–471. https://doi.org/10.1016/j.tcb.2014.04.002.
2. Lüscher, B., Ahel, I., Altmeyer, M., Ashworth, A., Bai, P., Chang, P., Cohen, M., Corda, D., Dantzer, F., Daugherty, M.D., et al. (2022). ADP-ribosyltransferases, an update on function and nomenclature. FEBS J. *289*, 7399–7410. https://doi.org/10.1111/febs.16142.
3. Dölle, C., Rack, J.G.M., and Ziegler, M. (2013). NAD and ADP-ribose metabolism in mitochondria. FEBS J. *280*, 3530–3541. https://doi.org/10.1111/febs.12304.
4. Hopp, A.K., and Hottiger, M.O. (2021). Uncovering the invisible: mono-ADP-ribosylation moved into the spotlight. Cells *10*, 680. https://doi.org/10.3390/cells10030680.
5. Covarrubias, A.J., Perrone, R., Grozio, A., and Verdin, E. (2021). NAD^+ metabolism and its roles in cellular processes during ageing. Nat. Rev. Mol. Cell Biol. *22*, 119–141. https://doi.org/10.1038/s41580-020-00313-x.
6. Katsyuba, E., Romani, M., Hofer, D., and Auwerx, J. (2020). NAD^+ homeostasis in health and disease. Nat. Metab. *2*, 9–31. https://doi.org/10.1038/s42255-019-0161-5.
7. Cantó, C., Menzies, K.J., and Auwerx, J. (2015). NAD(+) metabolism and the control of energy homeostasis: a balancing act between mitochondria and the nucleus. Cell Metab. *22*, 31–53. https://doi.org/10.1016/j.cmet.2015.05.023.
8. Agledal, L., Niere, M., and Ziegler, M. (2010). The phosphate makes a difference: cellular functions of NADP. Redox Rep. *15*, 2–10. https://doi.org/10.1179/174329210X12650506623122.
9. Katsyuba, E., Mottis, A., Zietak, M., De Franco, F., van der Velpen, V., Gariani, K., Ryu, D., Cialabrini, L., Matilainen, O., Liscio, P., et al. (2018). De novo NAD^+ synthesis enhances mitochondrial function and improves health. Nature *563*, 354–359. https://doi.org/10.1038/s41586-018-0645-6.
10. Tarragó, M.G., Chini, C.C.S., Kanamori, K.S., Warner, G.M., Caride, A., de Oliveira, G.C., Rud, M., Samani, A., Hein, K.Z., Huang, R., et al. (2018). A potent and specific CD38 inhibitor ameliorates age-related metabolic dysfunction by reversing tissue NAD^+ decline. Cell Metab. *27*, 1081–1095.e10. https://doi.org/10.1016/j.cmet.2018.03.016.
11. Khan, N.A., Auranen, M., Paetau, I., Pirinen, E., Euro, L., Forsström, S., Pasila, L., Velagapudi, V., Carroll, C.J., Auwerx, J., et al. (2014). Effective treatment of mitochondrial myopathy by nicotinamide riboside, a vitamin B3. EMBO Mol. Med. *6*, 721–731. https://doi.org/10.1002/emmm.201403943.
12. Trammell, S.A.J., Weidemann, B.J., Chadda, A., Yorek, M.S., Holmes, A., Coppey, L.J., Obrosov, A., Kardon, R.H., Yorek, M.A., and Brenner, C. (2016). Nicotinamide riboside opposes type 2 diabetes and neuropathy in mice. Sci. Rep. *6*, 26933. https://doi.org/10.1038/srep26933.
13. Cantó, C., Houtkooper, R.H., Pirinen, E., Youn, D.Y., Oosterveer, M.H., Cen, Y., Fernandez-Marcos, P.J., Yamamoto, H., Andreux, P.A., Cettour-Rose, P., et al. (2012). The NAD(+) precursor nicotinamide riboside enhances oxidative metabolism and protects against high-fat diet-induced obesity. Cell Metab. *15*, 838–847. https://doi.org/10.1016/j.cmet.2012.04.022.
14. Elhassan, Y.S., Kluckova, K., Fletcher, R.S., Schmidt, M.S., Garten, A., Doig, C.L., Cartwright, D.M., Oakey, L., Burley, C.V., Jenkinson, N., et al. (2019). Nicotinamide riboside augments the aged human skeletal muscle NAD^+ metabolome and induces transcriptomic and anti-inflammatory signatures. Cell Rep. *28*, 1717–1728.e6. https://doi.org/10.1016/j.celrep.2019.07.043.
15. Vreones, M., Mustapic, M., Moaddel, R., Pucha, K.A., Lovett, J., Seals, D. R., Kapogiannis, D., and Martens, C.R. (2023). Oral nicotinamide riboside raises NAD^+ and lowers biomarkers of neurodegenerative pathology in plasma extracellular vesicles enriched for neuronal origin. Aging Cell *22*, e13754. https://doi.org/10.1111/acel.13754.
16. Zhang, H., Ryu, D., Wu, Y., Gariani, K., Wang, X., Luan, P., D'Amico, D., Ropelle, E.R., Lutolf, M.P., Aebersold, R., et al. (2016). NAD^+ repletion improves mitochondrial and stem cell function and enhances life span in mice. Science *352*, 1436–1443. https://doi.org/10.1126/science.aaf2693.
17. Ryu, D., Zhang, H., Ropelle, E.R., Sorrentino, V., Mázala, D.A.G., Mouchiroud, L., Marshall, P.L., Campbell, M.D., Ali, A.S., Knowels, G.

M., et al. (2016). NAD$^+$ repletion improves muscle function in muscular dystrophy and counters global PARylation. Sci. Transl. Med. *8*, 361ra139. https://doi.org/10.1126/scitranslmed.aaf5504.

18. Pirinen, E., Auranen, M., Khan, N.A., Brilhante, V., Urho, N., Pessia, A., Hakkarainen, A., Kuula, J., Heinonen, U., Schmidt, M.S., et al. (2020). Niacin cures systemic NAD$^+$ deficiency and improves muscle performance in adult-onset mitochondrial myopathy. Cell Metab. *31*, 1078–1090.e5. https://doi.org/10.1016/j.cmet.2020.04.008.
19. Yoshino, M., Yoshino, J., Kayser, B.D., Patti, G.J., Franczyk, M.P., Mills, K.F., Sindelar, M., Pietka, T., Patterson, B.W., Imai, S.I., et al. (2021). Nicotinamide mononucleotide increases muscle insulin sensitivity in prediabetic women. Science *372*, 1224–1229. https://doi.org/10.1126/science.abe9985.
20. Romani, M., Sorrentino, V., Oh, C.M., Li, H., de Lima, T.I., Zhang, H., Shong, M., and Auwerx, J. (2021). NAD$^+$ boosting reduces age-associated amyloidosis and restores mitochondrial homeostasis in muscle. Cell Rep. *34*, 108660. https://doi.org/10.1016/j.celrep.2020.108660.
21. Mills, K.F., Yoshida, S., Stein, L.R., Grozio, A., Kubota, S., Sasaki, Y., Redpath, P., Migaud, M.E., Apte, R.S., Uchida, K., et al. (2016). Long-term administration of nicotinamide mononucleotide mitigates age-associated physiological decline in mice. Cell Metab. *24*, 795–806. https://doi.org/10.1016/j.cmet.2016.09.013.
22. Membrez, M., Migliavacca, E., Christen, S., Yaku, K., Trieu, J., Lee, A.K., Morandini, F., Giner, M.P., Stiner, J., Makarov, M.V., et al. (2024). Trigonelline is an NAD$^+$ precursor that improves muscle function during ageing and is reduced in human sarcopenia. Nat. Metab. *6*, 433–447. https://doi.org/10.1038/s42255-024-00997-x.
23. Migliavacca, E., Tay, S.K.H., Patel, H.P., Sonntag, T., Civiletto, G., McFarlane, C., Forrester, T., Barton, S.J., Leow, M.K., Antoun, E., et al. (2019). Mitochondrial oxidative capacity and NAD$^+$ biosynthesis are reduced in human sarcopenia across ethnicities. Nat. Commun. *10*, 5808. https://doi.org/10.1038/s41467-019-13694-1.
24. Beltrà, M., Pöllänen, N., Fornelli, C., Tonttila, K., Hsu, M.Y., Zampieri, S., Moletta, L., Corrà, S., Porporato, P.E., Kivelä, R., et al. (2023). NAD$^+$ repletion with niacin counteracts cancer cachexia. Nat. Commun. *14*, 1849. https://doi.org/10.1038/s41467-023-37595-6.
25. Gomes, A.P., Price, N.L., Ling, A.J.Y., Moslehi, J.J., Montgomery, M.K., Rajman, L., White, J.P., Teodoro, J.S., Wrann, C.D., Hubbard, B.P., et al. (2013). Declining NAD(+) induces a pseudohypoxic state disrupting nuclear-mitochondrial communication during aging. Cell *155*, 1624–1638. https://doi.org/10.1016/j.cell.2013.11.037.
26. Yeo, D., Kang, C., and Ji, L.L. (2020). Aging alters acetylation status in skeletal and cardiac muscles. GeroScience *42*, 963–976. https://doi.org/10.1007/s11357-020-00171-7.
27. Janssens, G.E., Grevendonk, L., Perez, R.Z., Schomakers, B.V., de Vogel-van den Bosch, J., Geurts, J.M.W., van Weeghel, M., Schrauwen, P., Houtkooper, R.H., and Hoeks, J. (2022). Healthy aging and muscle function are positively associated with NAD$^+$ abundance in humans. Nat Aging *2*, 254–263. https://doi.org/10.1038/s43587-022-00174-3.
28. Frederick, D.W., Loro, E., Liu, L., Davila, A., Jr., Chellappa, K., Silverman, I.M., Quinn, W.J., 3rd, Gosai, S.J., Tichy, E.D., Davis, J.G., et al. (2016). Loss of NAD homeostasis leads to progressive and reversible degeneration of skeletal muscle. Cell Metab. *24*, 269–282. https://doi.org/10.1016/j.cmet.2016.07.005.
29. Basse, A.L., Agerholm, M., Farup, J., Dalbram, E., Nielsen, J., Ørtenblad, N., Altıntaş, A., Ehrlich, A.M., Krag, T., Bruzzone, S., et al. (2021). Nampt controls skeletal muscle development by maintaining Ca^{2+} homeostasis and mitochondrial integrity. Mol. Metab. *53*, 101271. https://doi.org/10.1016/j.molmet.2021.101271.
30. Dutta, T., Kapoor, N., Mathew, M., Chakraborty, S.S., Ward, N.P., Prieto-Farigua, N., Falzone, A., DeLany, J.P., Smith, S.R., Coen, P.M., et al. (2023). Source of nicotinamide governs its metabolic fate in cultured cells, mice, and humans. Cell Rep. *42*, 112218. https://doi.org/10.1016/j.celrep.2023.112218.
31. Hargreaves, M., and Spriet, L.L. (2020). Skeletal muscle energy metabolism during exercise. Nat. Metab. *2*, 817–828. https://doi.org/10.1038/s42255-020-0251-4.
32. Barnes, B.R., Marklund, S., Steiler, T.L., Walter, M., Hjälm, G., Amarger, V., Mahlapuu, M., Leng, Y., Johansson, C., Galuska, D., et al. (2004). The 5′-AMP-activated protein kinase gamma3 isoform has a key role in carbohydrate and lipid metabolism in glycolytic skeletal muscle. J. Biol. Chem. *279*, 38441–38447. https://doi.org/10.1074/jbc.M405533200.
33. Rhein, P., Desjardins, E.M., Rong, P., Ahwazi, D., Bonhoure, N., Stolte, J., Santos, M.D., Ovens, A.J., Ehrlich, A.M., Sanchez Garcia, J.L., et al. (2021). Compound- and fiber type-selective requirement of AMPKγ3 for insulin-independent glucose uptake in skeletal muscle. Mol. Metab. *51*, 101228. https://doi.org/10.1016/j.molmet.2021.101228.
34. Jørgensen, N.O., Kjøbsted, R., Larsen, M.R., Birk, J.B., Andersen, N.R., Albuquerque, B., Schjerling, P., Miller, R., Carling, D., Pehmøller, C.K., et al. (2021). Direct small molecule ADaM-site AMPK activators reveal an AMPKγ3-independent mechanism for blood glucose lowering. Mol. Metab. *51*, 101259. https://doi.org/10.1016/j.molmet.2021.101259.
35. Sun, C., Seranova, E., Cohen, M.A., Chipara, M., Roberts, J., Astuti, D., Palhegyi, A.M., Acharjee, A., Sedlackova, L., Kataura, T., et al. (2023). NAD depletion mediates cytotoxicity in human neurons with autophagy deficiency. Cell Rep. *42*, 112372. https://doi.org/10.1016/j.celrep.2023.112372.
36. Sarkar, A., Dutta, S., Sur, M., Chakraborty, S., Dey, P., and Mukherjee, P. (2023). Early loss of endogenous NAD$^+$ following rotenone treatment leads to mitochondrial dysfunction and Sarm1 induction that is ameliorated by PARP inhibition. FEBS J. *290*, 1596–1624. https://doi.org/10.1111/febs.16652.
37. Kataura, T., Sedlackova, L., Otten, E.G., Kumari, R., Shapira, D., Scialo, F., Stefanatos, R., Ishikawa, K.I., Kelly, G., Seranova, E., et al. (2022). Autophagy promotes cell survival by maintaining NAD levels. Dev. Cell *57*, 2584–2598.e11. https://doi.org/10.1016/j.devcel.2022.10.008.
38. Sadri, S., Zhang, X., Audi, S.H., Cowley, A.W., Jr., and Dash, R.K. (2023). Computational modeling of substrate-dependent mitochondrial respiration and bioenergetics in the heart and kidney cortex and outer medulla. Function (Oxf) *4*, zqad038. https://doi.org/10.1093/function/zqad038.
39. Bouviere, J., Fortunato, R.S., Dupuy, C., Werneck-de-Castro, J.P., Carvalho, D.P., and Louzada, R.A. (2021). Exercise-stimulated ROS sensitive signaling pathways in skeletal muscle. Antioxidants (Basel) *10*, 537. https://doi.org/10.3390/antiox10040537.
40. Zorov, D.B., Juhaszova, M., and Sollott, S.J. (2014). Mitochondrial reactive oxygen species (ROS) and ROS-induced ROS release. Physiol. Rev. *94*, 909–950. https://doi.org/10.1152/physrev.00026.2013.
41. Debattisti, V., Gerencser, A.A., Saotome, M., Das, S., and Hajnóczky, G. (2017). ROS control mitochondrial motility through p38 and the motor adaptor Miro/Trak. Cell Rep. *21*, 1667–1680. https://doi.org/10.1016/j.celrep.2017.10.060.
42. Pharaoh, G., Brown, J.L., Sataranatarajan, K., Kneis, P., Bian, J., Ranjit, R., Hadad, N., Georgescu, C., Rabinovitch, P., Ran, Q., et al. (2020). Targeting cPLA$_2$ derived lipid hydroperoxides as a potential intervention for sarcopenia. Sci. Rep. *10*, 13968. https://doi.org/10.1038/s41598-020-70792-7.
43. Laker, R.C., Drake, J.C., Wilson, R.J., Lira, V.A., Lewellen, B.M., Ryall, K.A., Fisher, C.C., Zhang, M., Saucerman, J.J., Goodyear, L.J., et al. (2017). Ampk phosphorylation of Ulk1 is required for targeting of mitochondria to lysosomes in exercise-induced mitophagy. Nat. Commun. *8*, 548. https://doi.org/10.1038/s41467-017-00520-9.
44. Henríquez-Olguin, C., Knudsen, J.R., Raun, S.H., Li, Z., Dalbram, E., Treebak, J.T., Sylow, L., Holmdahl, R., Richter, E.A., Jaimovich, E., et al. (2019). Cytosolic ROS production by NADPH oxidase 2 regulates muscle glucose uptake during exercise. Nat. Commun. *10*, 4623. https://doi.org/10.1038/s41467-019-12523-9.
45. Morant-Ferrando, B., Jimenez-Blasco, D., Alonso-Batan, P., Agulla, J., Lapresa, R., Garcia-Rodriguez, D., Yunta-Sanchez, S., Lopez-Fabuel, I., Fernandez, E., Carmeliet, P., et al. (2023). Fatty acid oxidation

organizes mitochondrial supercomplexes to sustain astrocytic ROS and cognition. Nat. Metab. *5*, 1290–1302. https://doi.org/10.1038/s42255-023-00835-6.

46. Greggio, C., Jha, P., Kulkarni, S.S., Lagarrigue, S., Broskey, N.T., Boutant, M., Wang, X., Conde Alonso, S., Ofori, E., Auwerx, J., et al. (2017). Enhanced respiratory chain supercomplex formation in response to exercise in human skeletal muscle. Cell Metab. *25*, 301–311. https://doi.org/10.1016/j.cmet.2016.11.004.
47. Stein, C.S., Jadiya, P., Zhang, X., McLendon, J.M., Abouassaly, G.M., Witmer, N.H., Anderson, E.J., Elrod, J.W., and Boudreau, R.L. (2018). Mitoregulin: a lncRNA-Encoded microprotein that supports mitochondrial supercomplexes and respiratory efficiency. Cell Rep. *23*, 3710–3720.e8. https://doi.org/10.1016/j.celrep.2018.06.002.
48. Mitsopoulos, P., Chang, Y.H., Wai, T., König, T., Dunn, S.D., Langer, T., and Madrenas, J. (2015). Stomatin-like protein 2 is required for in vivo mitochondrial respiratory chain supercomplex formation and optimal cell function. Mol. Cell. Biol. *35*, 1838–1847. https://doi.org/10.1128/MCB.00047-15.
49. Gonzalez-Franquesa, A., Stocks, B., Chubanava, S., Hattel, H.B., Moreno-Justicia, R., Peijs, L., Treebak, J.T., Zierath, J.R., and Deshmukh, A.S. (2021). Mass-spectrometry-based proteomics reveals mitochondrial supercomplexome plasticity. Cell Rep. *35*, 109180. https://doi.org/10.1016/j.celrep.2021.109180.
50. McReynolds, M.R., Chellappa, K., Chiles, E., Jankowski, C., Shen, Y., Chen, L., Descamps, H.C., Mukherjee, S., Bhat, Y.R., Lingala, S.R., et al. (2021). NAD^+ flux is maintained in aged mice despite lower tissue concentrations. Cell Syst. *12*, 1160–1172.e4. https://doi.org/10.1016/j.cels.2021.09.001.
51. Seldeen, K.L., Shahini, A., Thiyagarajan, R., Redae, Y., Leiker, M., Rajabian, N., Dynka, A., Andreadis, S.T., and Troen, B.R. (2021). Short-term nicotinamide riboside treatment improves muscle quality and function in mice and increases cellular energetics and differentiating capacity of myogenic progenitors. Nutrition *87–88*, 111189. https://doi.org/10.1016/j.nut.2021.111189.
52. Slavin, B.G., and Lerner, S.P. (1990). Age-related immunohistochemical studies of A and D cells in pancreatic islets of C57BL/6J mice. Anat. Rec. *228*, 53–57. https://doi.org/10.1002/ar.1092280109.
53. Sun, N., Youle, R.J., and Finkel, T. (2016). The mitochondrial basis of aging. Mol. Cell *61*, 654–666. https://doi.org/10.1016/j.molcel.2016.01.028.
54. Moqri, M., Herzog, C., Poganik, J.R., Ying, K., Justice, J.N., Belsky, D.W., Higgins-Chen, A.T., Chen, B.H., Cohen, A.A., Fuellen, G., et al. (2024). Validation of biomarkers of aging. Nat. Med. *30*, 360–372. https://doi.org/10.1038/s41591-023-02784-9.
55. Jones, R.G., 3rd, Dimet-Wiley, A., Haghani, A., da Silva, F.M., Brightwell, C.R., Lim, S., Khadgi, S., Wen, Y., Dungan, C.M., Brooke, R.T., et al. (2023). A molecular signature defining exercise adaptation with ageing and in vivo partial reprogramming in skeletal muscle. J. Physiol. *601*, 763–782. https://doi.org/10.1113/JP283836.
56. Zapata-Pérez, R., Wanders, R.J.A., van Karnebeek, C.D.M., and Houtkooper, R.H. (2021). NAD^+ homeostasis in human health and disease. EMBO Mol. Med. *13*, e13943. https://doi.org/10.15252/emmm.202113943.
57. Lautrup, S., Sinclair, D.A., Mattson, M.P., and Fang, E.F. (2019). NAD^+ in brain aging and neurodegenerative disorders. Cell Metab. *30*, 630–655. https://doi.org/10.1016/j.cmet.2019.09.001.
58. Reiten, O.K., Wilvang, M.A., Mitchell, S.J., Hu, Z., and Fang, E.F. (2021). Preclinical and clinical evidence of NAD^+ precursors in health, disease, and ageing. Mech. Ageing Dev. *199*, 111567. https://doi.org/10.1016/j.mad.2021.111567.
59. Zheng, M., Schultz, M.B., and Sinclair, D.A. (2022). NAD^+ in COVID-19 and viral infections. Trends Immunol. *43*, 283–295. https://doi.org/10.1016/j.it.2022.02.001.
60. Peluso, A., Damgaard, M.V., Mori, M.A.S., and Treebak, J.T. (2021). Age-dependent decline of NAD^+-universal truth or confounded consensus? Nutrients *14*, 101. https://doi.org/10.3390/nu14010101.
61. de Guia, R.M., Agerholm, M., Nielsen, T.S., Consitt, L.A., Søgaard, D., Helge, J.W., Larsen, S., Brandauer, J., Houmard, J.A., and Treebak, J. T. (2019). Aerobic and resistance exercise training reverses age-dependent decline in NAD^+ salvage capacity in human skeletal muscle. Physiol. Rep. *7*, e14139. https://doi.org/10.14814/phy2.14139.
62. Camacho-Pereira, J., Tarragó, M.G., Chini, C.C.S., Nin, V., Escande, C., Warner, G.M., Puranik, A.S., Schoon, R.A., Reid, J.M., Galina, A., et al. (2016). CD38 dictates age-related NAD decline and mitochondrial dysfunction through an SIRT3-dependent mechanism. Cell Metab. *23*, 1127–1139. https://doi.org/10.1016/j.cmet.2016.05.006.
63. Chubanava, S., and Treebak, J.T. (2023). Regular exercise effectively protects against the aging-associated decline in skeletal muscle NAD content. Exp. Gerontol. *173*, 112109. https://doi.org/10.1016/j.exger.2023.112109.
64. Forni, P.E., Scuoppo, C., Imayoshi, I., Taulli, R., Dastrù, W., Sala, V., Betz, U.A.K., Muzzi, P., Martinuzzi, D., Vercelli, A.E., et al. (2006). High levels of Cre expression in neuronal progenitors cause defects in brain development leading to microencephaly and hydrocephaly. J. Neurosci. *26*, 9593–9602. https://doi.org/10.1523/JNEUROSCI.2815-06.2006.
65. Pugach, E.K., Richmond, P.A., Azofeifa, J.G., Dowell, R.D., and Leinwand, L.A. (2015). Prolonged Cre expression driven by the alpha-myosin heavy chain promoter can be cardiotoxic. J. Mol. Cell. Cardiol. *86*, 54–61. https://doi.org/10.1016/j.yjmcc.2015.06.019.
66. Miniou, P., Tiziano, D., Frugier, T., Roblot, N., Le Meur, M., and Melki, J. (1999). Gene targeting restricted to mouse striated muscle lineage. Nucleic Acids Res. *27*, e27. https://doi.org/10.1093/nar/27.19.e27.
67. Rosenthal, N., Kornhauser, J.M., Donoghue, M., Rosen, K.M., and Merlie, J.P. (1989). Myosin light chain enhancer activates muscle-specific, developmentally regulated gene expression in transgenic mice. Proc. Natl. Acad. Sci. USA *86*, 7780–7784. https://doi.org/10.1073/pnas.86.20.7780.
68. Zolkiewska, A., and Moss, J. (1997). The alpha 7 integrin as a target protein for cell surface mono-ADP-ribosylation in muscle cells. Adv. Exp. Med. Biol. *419*, 297–303. https://doi.org/10.1007/978-1-4419-8632-0_39.
69. Zhao, Z., Gruszczynska-Biegala, J., and Zolkiewska, A. (2005). ADP-ribosylation of integrin alpha7 modulates the binding of integrin alpha7-beta1 to laminin. Biochem. J. *385*, 309–317. https://doi.org/10.1042/BJ20040590.
70. Gaude, E., Schmidt, C., Gammage, P.A., Dugourd, A., Blacker, T., Chew, S.P., Saez-Rodriguez, J., O'Neill, J.S., Szabadkai, G., Minczuk, M., et al. (2018). NADH shuttling couples cytosolic reductive carboxylation of glutamine with glycolysis in cells with mitochondrial dysfunction. Mol. Cell *69*, 581–593.e7. https://doi.org/10.1016/j.molcel.2018.01.034.
71. Svedružić, Z.M., and Spivey, H.O. (2006). Interaction between mammalian glyceraldehyde-3-phosphate dehydrogenase and L-lactate dehydrogenase from heart and muscle. Proteins *63*, 501–511. https://doi.org/10.1002/prot.20862.
72. Schantz, P.G., Sjöberg, B., and Svedenhag, J. (1986). Malate-aspartate and alpha-glycerophosphate shuttle enzyme levels in human skeletal muscle: methodological considerations and effect of endurance training. Acta Physiol. Scand. *128*, 397–407. https://doi.org/10.1111/j.1748-1716.1986.tb07993.x.
73. Brooks, G.A. (2018). The science and translation of lactate shuttle theory. Cell Metab. *27*, 757–785. https://doi.org/10.1016/j.cmet.2018.03.008.
74. Nilsson, A., Björnson, E., Flockhart, M., Larsen, F.J., and Nielsen, J. (2019). Complex I is bypassed during high intensity exercise. Nat. Commun. *10*, 5072. https://doi.org/10.1038/s41467-019-12934-8.
75. Holloszy, J.O., Oscai, L.B., Molé, P.A., and Don, I.J. (1971). Biochemical adaptations to endurance exercise in skeletal muscle. In Muscle Metabolism During Exercise. Advances in Experimental Medicine and Biology, B. Pernow and B. Saltin, eds. (Springer), pp. 51–61. https://doi.org/10.1007/978-1-4613-4609-8_5.
76. Hui, S., Ghergurovich, J.M., Morscher, R.J., Jang, C., Teng, X., Lu, W., Esparza, L.A., Reya, T., Le, Z., Yanxiang Guo, J., et al. (2017). Glucose

feeds the TCA cycle via circulating lactate. Nature *551*, 115–118. https://doi.org/10.1038/nature24057.

77. Lima, T., Li, T.Y., Mottis, A., and Auwerx, J. (2022). Pleiotropic effects of mitochondria in aging. Nat Aging *2*, 199–213. https://doi.org/10.1038/s43587-022-00191-2.
78. He, F., Li, J., Liu, Z., Chuang, C.C., Yang, W., and Zuo, L. (2016). Redox mechanism of reactive oxygen species in exercise. Front. Physiol. *7*, 486. https://doi.org/10.3389/fphys.2016.00486.
79. Barbeau, P.A., Miotto, P.M., and Holloway, G.P. (2018). Mitochondrial-derived reactive oxygen species influence ADP sensitivity, but not CPT-I substrate sensitivity. Biochem. J. *475*, 2997–3008. https://doi.org/10.1042/BCJ20180419.
80. Wong, H.S., Dighe, P.A., Mezera, V., Monternier, P.A., and Brand, M.D. (2017). Production of superoxide and hydrogen peroxide from specific mitochondrial sites under different bioenergetic conditions. J. Biol. Chem. *292*, 16804–16809. https://doi.org/10.1074/jbc.R117.789271.
81. Goncalves, R.L.S., Quinlan, C.L., Perevoshchikova, I.V., Hey-Mogensen, M., and Brand, M.D. (2015). Sites of superoxide and hydrogen peroxide production by muscle mitochondria assessed ex vivo under conditions mimicking rest and exercise. J. Biol. Chem. *290*, 209–227. https://doi.org/10.1074/jbc.M114.619072.
82. Brand, M.D. (2020). Riding the tiger - physiological and pathological effects of superoxide and hydrogen peroxide generated in the mitochondrial matrix. Crit. Rev. Biochem. Mol. Biol. *55*, 592–661. https://doi.org/10.1080/10409238.2020.1828258.
83. Quinlan, C.L., Perevoshchikova, I.V., Hey-Mogensen, M., Orr, A.L., and Brand, M.D. (2013). Sites of reactive oxygen species generation by mitochondria oxidizing different substrates. Redox Biol. *1*, 304–312. https://doi.org/10.1016/j.redox.2013.04.005.
84. Lopez-Fabuel, I., Le Douce, J., Logan, A., James, A.M., Bonvento, G., Murphy, M.P., Almeida, A., and Bolaños, J.P. (2016). Complex I assembly into supercomplexes determines differential mitochondrial ROS production in neurons and astrocytes. Proc. Natl. Acad. Sci. USA *113*, 13063–13068. https://doi.org/10.1073/pnas.1613701113.
85. Maranzana, E., Barbero, G., Falasca, A.I., Lenaz, G., and Genova, M.L. (2013). Mitochondrial respiratory supercomplex association limits production of reactive oxygen species from complex I. Antioxid. Redox Signal. *19*, 1469–1480. https://doi.org/10.1089/ars.2012.4845.
86. Palma, F.R., Gantner, B.N., Sakiyama, M.J., Kayzuka, C., Shukla, S., Lacchini, R., Cunniff, B., and Bonini, M.G. (2024). ROS production by mitochondria: function or dysfunction? Oncogene *43*, 295–303. https://doi.org/10.1038/s41388-023-02907-z.
87. Peoples, J.N., Saraf, A., Ghazal, N., Pham, T.T., and Kwong, J.Q. (2019). Mitochondrial dysfunction and oxidative stress in heart disease. Exp. Mol. Med. *51*, 1–13. https://doi.org/10.1038/s12276-019-0355-7.
88. Merry, T.L., and Ristow, M. (2016). Do antioxidant supplements interfere with skeletal muscle adaptation to exercise training? J. Physiol. *594*, 5135–5147. https://doi.org/10.1113/JP270654.
89. Barbieri, E., and Sestili, P. (2012). Reactive oxygen species in skeletal muscle signaling. J. Signal Transduct. *2012*, 982794. https://doi.org/10.1155/2012/982794.
90. Henríquez-Olguín, C., Boronat, S., Cabello-Verrugio, C., Jaimovich, E., Hidalgo, E., and Jensen, T.E. (2019). The emerging roles of nicotinamide adenine dinucleotide phosphate oxidase 2 in skeletal muscle redox signaling and metabolism. Antioxid. Redox Signal. *31*, 1371–1410. https://doi.org/10.1089/ars.2018.7678.
91. Chan, K.M., and Decker, E.A. (1994). Endogenous skeletal muscle antioxidants. Crit. Rev. Food Sci. Nutr. *34*, 403–426. https://doi.org/10.1080/10408399409527669.
92. Jackson, M.J. (2011). Control of reactive oxygen species production in contracting skeletal muscle. Antioxid. Redox Signal. *15*, 2477–2486. https://doi.org/10.1089/ars.2011.3976.
93. Marí, M., Morales, A., Colell, A., García-Ruiz, C., and Fernández-Checa, J.C. (2009). Mitochondrial glutathione, a key survival antioxidant. Antioxid. Redox Signal. *11*, 2685–2700. https://doi.org/10.1089/ARS.2009.2695.
94. Sud, M., Fahy, E., Cotter, D., Azam, K., Vadivelu, I., Burant, C., Edison, A., Fiehn, O., Higashi, R., Nair, K.S., et al. (2016). Metabolomics Workbench: An international repository for metabolomics data and metadata, metabolite standards, protocols, tutorials and training, and analysis tools. Nucleic Acids Res. *44*, D463–D470. https://doi.org/10.1093/nar/gkv1042.
95. Schneider, C.A., Rasband, W.S., and Eliceiri, K.W. (2012). NIH Image to ImageJ: 25 years of image analysis. Nat. Methods *9*, 671–675. https://doi.org/10.1038/nmeth.2089.
96. Cox, J., and Mann, M. (2008). MaxQuant enables high peptide identification rates, individualized p.p.b.-range mass accuracies and proteome-wide protein quantification. Nat. Biotechnol. *26*, 1367–1372. https://doi.org/10.1038/nbt.1511.
97. Tyanova, S., Temu, T., Sinitcyn, P., Carlson, A., Hein, M.Y., Geiger, T., Mann, M., and Cox, J. (2016). The Perseus computational platform for comprehensive analysis of (prote)omics data. Nat. Methods *13*, 731–740. https://doi.org/10.1038/nmeth.3901.
98. Agerholm, M., Dall, M., Jensen, B.A.H., Prats, C., Madsen, S., Basse, A. L., Graae, A.S., Risis, S., Goldenbaum, J., Quistorff, B., et al. (2018). Perturbations of NAD^+ salvage systems impact mitochondrial function and energy homeostasis in mouse myoblasts and intact skeletal muscle. Am. J. Physiol. Endocrinol. Metab. *314*, E377–E395. https://doi.org/10.1152/ajpendo.00213.2017.
99. McCarthy, J.J., Srikuea, R., Kirby, T.J., Peterson, C.A., and Esser, K.A. (2012). Inducible Cre transgenic mouse strain for skeletal muscle-specific gene targeting. Skelet. Muscle *2*, 8. https://doi.org/10.1186/2044-5040-2-8.
100. Petrosino, J.M., Heiss, V.J., Maurya, S.K., Kalyanasundaram, A., Periasamy, M., LaFountain, R.A., Wilson, J.M., Simonetti, O.P., and Ziouzenkova, O. (2016). Graded maximal exercise testing to assess mouse cardio-metabolic phenotypes. PLoS One *11*, e0148010. https://doi.org/10.1371/journal.pone.0148010.
101. Hingst, J.R., Kjøbsted, R., Birk, J.B., Jørgensen, N.O., Larsen, M.R., Kido, K., Larsen, J.K., Kjeldsen, S.A.S., Fentz, J., Frøsig, C., et al. (2020). Inducible deletion of skeletal muscle AMPKalpha reveals that AMPK is required for nucleotide balance but dispensable for muscle glucose uptake and fat oxidation during exercise. Mol. Metab. *40*, 101028. https://doi.org/10.1016/j.molmet.2020.101028.
102. Dalbram, E., Basse, A.L., Zierath, J.R., and Treebak, J.T. (2019). Voluntary wheel running in the late dark phase ameliorates diet-induced obesity in mice without altering insulin action. J. Appl. Physiol. (1985) *126*, 993–1005. https://doi.org/10.1152/japplphysiol.00737.2018.
103. Basse, A.L., Dalbram, E., Larsson, L., Gerhart-Hines, Z., Zierath, J.R., and Treebak, J.T. (2018). Skeletal muscle insulin sensitivity show circadian rhythmicity which is independent of exercise training status. Front. Physiol. *9*, 1198. https://doi.org/10.3389/fphys.2018.01198.
104. Small, L., Ehrlich, A., Iversen, J., Ashcroft, S.P., Trošt, K., Moritz, T., Hartmann, B., Holst, J.J., Treebak, J.T., Zierath, J.R., et al. (2022). Comparative analysis of oral and intraperitoneal glucose tolerance tests in mice. Mol. Metab. *57*, 101440. https://doi.org/10.1016/j.molmet.2022.101440.
105. Ayala, J.E., Samuel, V.T., Morton, G.J., Obici, S., Croniger, C.M., Shulman, G.I., Wasserman, D.H., and McGuinness, O.P.; NIH Mouse Metabolic Phenotyping Center Consortium (2010). Standard operating procedures for describing and performing metabolic tests of glucose homeostasis in mice. Dis. Model. Mech. *3*, 525–534. https://doi.org/10.1242/dmm.006239.
106. Moorwood, C., Liu, M., Tian, Z., and Barton, E.R. (2013). Isometric and eccentric force generation assessment of skeletal muscles isolated from murine models of muscular dystrophies. J. Vis. Exp. e50036. https://doi.org/10.3791/50036.
107. Bhattacharya, S.K., Thakar, J.H., Johnson, P.L., and Shanklin, D.R. (1991). Isolation of skeletal muscle mitochondria from hamsters using

an ionic medium containing ethylenediaminetetraacetic acid and nagarse. Anal. Biochem. *192*, 344–349. https://doi.org/10.1016/0003-2697(91)90546-6.

108. Du, H., Guo, L., Fang, F., Chen, D., Sosunov, A.A., McKhann, G.M., Yan, Y., Wang, C., Zhang, H., Molkentin, J.D., et al. (2008). Cyclophilin D deficiency attenuates mitochondrial and neuronal perturbation and ameliorates learning and memory in Alzheimer's disease. Nat. Med. *14*, 1097–1105. https://doi.org/10.1038/nm.1868.

109. Jalil, M.A., Begum, L., Contreras, L., Pardo, B., Iijima, M., Li, M.X., Ramos, M., Marmol, P., Horiuchi, M., Shimotsu, K., et al. (2005). Reduced N-acetylaspartate levels in mice lacking aralar, a brain- and muscle-type mitochondrial aspartate-glutamate carrier. J. Biol. Chem. *280*, 31333–31339. https://doi.org/10.1074/jbc.M505286200.

110. Cheeseman, A.J., and Clark, J.B. (1988). Influence of the malate-aspartate shuttle on oxidative metabolism in synaptosomes. J. Neurochem. *50*, 1559–1565. https://doi.org/10.1111/j.1471-4159.1988.tb03044.x.

111. Palmeira, C.M., and Rolo, A.P. (2012). Mitochondrial membrane potential ($\Delta\Psi$) fluctuations associated with the metabolic states of mitochondria. Methods Mol. Biol. *810*, 89–101. https://doi.org/10.1007/978-1-61779-382-0_6.

112. Hey-Mogensen, M., Gram, M., Jensen, M.B., Lund, M.T., Hansen, C.N., Scheibye-Knudsen, M., Bohr, V.A., and Dela, F. (2015). A novel method for determining human ex vivo submaximal skeletal muscle mitochondrial function. J. Physiol. *593*, 3991–4010. https://doi.org/10.1113/JP270204.

113. Salin, K., Villasevil, E.M., Auer, S.K., Anderson, G.J., Selman, C., Metcalfe, N.B., and Chinopoulos, C. (2016). Simultaneous measurement of mitochondrial respiration and ATP production in tissue homogenates and calculation of effective P/O ratios. Physiol. Rep. *4*, e13007. https://doi.org/10.14814/phy2.13007.

114. Chinopoulos, C., Vajda, S., Csanády, L., Mándi, M., Mathe, K., and Adam-Vizi, V. (2009). A novel kinetic assay of mitochondrial ATP-ADP exchange rate mediated by the ANT. Biophys. J. *96*, 2490–2504. https://doi.org/10.1016/j.bpj.2008.12.3915.

115. Flensted-Jensen, M., Gram, M., Dela, F., Helge, J.W., and Larsen, S. (2021). Six weeks of high intensity cycle training reduces H_2O_2 emission and increases antioxidant protein levels in obese adults with risk factors for type 2 diabetes. Free Radic. Biol. Med. *173*, 1–6. https://doi.org/10.1016/j.freeradbiomed.2021.07.020.

116. Wong, H.S., Monternier, P.A., Orr, A.L., and Brand, M.D. (2018). Plate-based measurement of superoxide and hydrogen peroxide production by isolated mitochondria. Methods Mol. Biol. *1782*, 287–299. https://doi.org/10.1007/978-1-4939-7831-1_16.

117. Fisher-Wellman, K.H., Davidson, M.T., Narowski, T.M., Lin, C.T., Koves, T.R., and Muoio, D.M. (2018). Mitochondrial diagnostics: a multiplexed assay platform for comprehensive assessment of mitochondrial energy fluxes. Cell Rep. *24*, 3593–3606.e10. https://doi.org/10.1016/j.celrep.2018.08.091.

118. Hodek, O., Henderson, J., Argemi-Muntadas, L., Khan, A., and Moritz, T. (2023). Structural elucidation of 3-nitrophenylhydrazine derivatives of tricarboxylic acid cycle acids and optimization of their fragmentation to boost sensitivity in liquid chromatography-mass spectrometry. J. Chromatogr. B Analyt. Technol. Biomed. Life Sci. *1222*, 123719. https://doi.org/10.1016/j.jchromb.2023.123719.

119. Rende, U., Niittylä, T., and Moritz, T. (2019). Two-step derivatization for determination of sugar phosphates in plants by combined reversed phase chromatography/tandem mass spectrometry. Plant Methods *15*, 127. https://doi.org/10.1186/s13007-019-0514-9.

120. Dollerup, O.L., Chubanava, S., Agerholm, M., Søndergård, S.D., Altıntaş, A., Møller, A.B., Høyer, K.F., Ringgaard, S., Stødkilde-Jørgensen, H., Lavery, G.G., et al. (2020). Nicotinamide riboside does not alter mitochondrial respiration, content or morphology in skeletal muscle from obese and insulin-resistant men. J. Physiol. *598*, 731–754. https://doi.org/10.1113/JP278752.

121. Ewels, P.A., Peltzer, A., Fillinger, S., Patel, H., Alneberg, J., Wilm, A., Garcia, M.U., Di Tommaso, P., and Nahnsen, S. (2020). The nf-core framework for community-curated bioinformatics pipelines. Nat. Biotechnol. *38*, 276–278. https://doi.org/10.1038/s41587-020-0439-x.

122. Patel, H., Ewels, P., Peltzer, A., Hammarén, R., Botvinnik, O., Sturm, G., Moreno, D., Vemuri, P., silviamorins, Pantano, L., et al. (2022). nf-core/rnaseq: nf-core/rnaseq v3.8.1 - Plastered Magnesium Mongoose (3.8.1). Zenodo. https://doi.org/10.5281/zenodo.6587789.

123. Frankish, A., Diekhans, M., Ferreira, A.M., Johnson, R., Jungreis, I., Loveland, J., Mudge, J.M., Sisu, C., Wright, J., Armstrong, J., et al. (2019). GENCODE reference annotation for the human and mouse genomes. Nucleic Acids Res. *47*, D766–D773. https://doi.org/10.1093/nar/gky955.

124. Robinson, M.D., McCarthy, D.J., and Smyth, G.K. (2010). edgeR: a Bioconductor package for differential expression analysis of digital gene expression data. Bioinformatics *26*, 139–140. https://doi.org/10.1093/bioinformatics/btp616.

125. Small, L., Lundell, L.S., Iversen, J., Ehrlich, A.M., Dall, M., Basse, A.L., Dalbram, E., Hansen, A.N., Treebak, J.T., Barrès, R., et al. (2023). Seasonal light hours modulate peripheral clocks and energy metabolism in mice. Cell Metab. *35*, 1722–1735.e5. https://doi.org/10.1016/j.cmet.2023.08.005.

126. Damgaard, M.V., Nielsen, T.S., Basse, A.L., Chubanava, S., Trost, K., Moritz, T., Dellinger, R.W., Larsen, S., and Treebak, J.T. (2022). Intravenous nicotinamide riboside elevates mouse skeletal muscle NAD^+ without impacting respiratory capacity or insulin sensitivity. iScience *25*, 103863. https://doi.org/10.1016/j.isci.2022.103863.

127. Jensen, J.B., Dollerup, O.L., Møller, A.B., Billeskov, T.B., Dalbram, E., Chubanava, S., Damgaard, M.V., Dellinger, R.W., Trošt, K., Moritz, T., et al. (2022). A randomized placebo-controlled trial of nicotinamide riboside and pterostilbene supplementation in experimental muscle injury in elderly individuals. JCI Insight *7*, e158314. https://doi.org/10.1172/jci.insight.158314.

128. Alp, P.R., Newsholme, E.A., and Zammit, V.A. (1976). Activities of citrate synthase and NAD^+-linked and $NADP^+$-linked isocitrate dehydrogenase in muscle from vertebrates and invertebrates. Biochem. J. *154*, 689–700. https://doi.org/10.1042/bj1540689.

129. Eigentler, A., Draxl, A., and Gnaiger, E. (2020). Laboratory Protocol: Citrate Synthase a Mitochondrial Marker Enzyme (Mitochondrial Physiology Network), pp. 1–12. https://www.bioblast.at/images/4/40/MiPNet17.04_CitrateSynthase.pdf.

130. Malik, A.N., Shahni, R., Rodriguez-de-Ledesma, A., Laftah, A., and Cunningham, P. (2011). Mitochondrial DNA as a non-invasive biomarker: accurate quantification using real time quantitative PCR without co-amplification of pseudogenes and dilution bias. Biochem. Biophys. Res. Commun. *412*, 1–7. https://doi.org/10.1016/j.bbrc.2011.06.067.

131. Sustarsic, E.G., Ma, T., Lynes, M.D., Larsen, M., Karavaeva, I., Havelund, J.F., Nielsen, C.H., Jedrychowski, M.P., Moreno-Torres, M., Lundh, M., et al. (2018). Cardiolipin synthesis in brown and beige fat mitochondria is essential for systemic energy homeostasis. Cell Metab. *28*, 159–174.e11. https://doi.org/10.1016/j.cmet.2018.05.003.

132. Arneson, A., Haghani, A., Thompson, M.J., Pellegrini, M., Kwon, S.B., Vu, H., Maciejewski, E., Yao, M., Li, C.Z., Lu, A.T., et al. (2022). A mammalian methylation array for profiling methylation levels at conserved sequences. Nat. Commun. *13*, 783. https://doi.org/10.1038/s41467-022-28355-z.

133. Zhou, W., Dinh, H.Q., Ramjan, Z., Weisenberger, D.J., Nicolet, C.M., Shen, H., Laird, P.W., and Berman, B.P. (2018). DNA methylation loss in late-replicating domains is linked to mitotic cell division. Nat. Genet. *50*, 591–602. https://doi.org/10.1038/s41588-018-0073-4.

134. Du, P., Zhang, X., Huang, C.C., Jafari, N., Kibbe, W.A., Hou, L., and Lin, S.M. (2010). Comparison of beta-value and M-value methods for quantifying methylation levels by microarray analysis. BMC Bioinformatics *11*, 587. https://doi.org/10.1186/1471-2105-11-587.

135. Ritchie, M.E., Phipson, B., Wu, D., Hu, Y., Law, C.W., Shi, W., and Smyth, G.K. (2015). limma powers differential expression analyses for RNA-sequencing and microarray studies. Nucleic Acids Res. *43*, e47. https://doi.org/10.1093/nar/gkv007.

136. Risso, D., Ngai, J., Speed, T.P., and Dudoit, S. (2014). Normalization of RNA-seq data using factor analysis of control genes or samples. Nat. Biotechnol. *32*, 896–902. https://doi.org/10.1038/nbt.2931.

137. Giustarini, D., Dalle-Donne, I., Milzani, A., Fanti, P., and Rossi, R. (2013). Analysis of GSH and GSSG after derivatization with N-ethylmaleimide. Nat. Protoc. *8*, 1660–1669. https://doi.org/10.1038/nprot.2013.095.

138. Ludwig, C., and Günther, U.L. (2011). MetaboLab–advanced NMR data processing and analysis for metabolomics. BMC Bioinformatics *12*, 366. https://doi.org/10.1186/1471-2105-12-366.

139. Bultot, L., Jensen, T.E., Lai, Y.C., Madsen, A.L.B., Collodet, C., Kviklyte, S., Deak, M., Yavari, A., Foretz, M., Ghaffari, S., et al. (2016). Benzimidazole derivative small-molecule 991 enhances AMPK activity and glucose uptake induced by AICAR or contraction in skeletal muscle. Am. J. Physiol. Endocrinol. Metab. *311*, E706–E719. https://doi.org/10.1152/ajpendo.00237.2016.

140. Merry, T.L., Steinberg, G.R., Lynch, G.S., and McConell, G.K. (2010). Skeletal muscle glucose uptake during contraction is regulated by nitric oxide and ROS independently of AMPK. Am. J. Physiol. Endocrinol. Metab. *298*, E577–E585. https://doi.org/10.1152/ajpendo.00239.2009.

141. Schindelin, J., Arganda-Carreras, I., Frise, E., Kaynig, V., Longair, M., Pietzsch, T., Preibisch, S., Rueden, C., Saalfeld, S., Schmid, B., et al. (2012). Fiji: an open-source platform for biological-image analysis. Nat. Methods *9*, 676–682. https://doi.org/10.1038/nmeth.2019.

142. Liu, L., Cheung, T.H., Charville, G.W., and Rando, T.A. (2015). Isolation of skeletal muscle stem cells by fluorescence-activated cell sorting. Nat. Protoc. *10*, 1612–1624. https://doi.org/10.1038/nprot.2015.110.

143. Folch, J., Lees, M., and Sloane Stanley, G.H. (1957). A simple method for the isolation and purification of total lipides from animal tissues. J. Biol. Chem. *226*, 497–509. https://doi.org/10.1016/S0021-9258(18)64849-5.

144. Kind, T., Liu, K.H., Lee, D.Y., DeFelice, B., Meissen, J.K., and Fiehn, O. (2013). LipidBlast in silico tandem mass spectrometry database for lipid identification. Nat. Methods *10*, 755–758. https://doi.org/10.1038/nmeth.2551.

145. Luan, H., Ji, F., Chen, Y., and Cai, Z. (2018). statTarget: A streamlined tool for signal drift correction and interpretations of quantitative mass spectrometry-based omics data. Anal. Chim. Acta *1036*, 66–72. https://doi.org/10.1016/j.aca.2018.08.002.

146. Pang, Z., Chong, J., Zhou, G., de Lima Morais, D.A., Chang, L., Barrette, M., Gauthier, C., Jacques, P.É., Li, S., and Xia, J. (2021). MetaboAnalyst 5.0: narrowing the gap between raw spectra and functional insights. Nucleic Acids Res. *49*, W388–W396. https://doi.org/10.1093/nar/gkab382.

147. Hostrup, M., Lemminger, A.K., Stocks, B., Gonzalez-Franquesa, A., Larsen, J.K., Quesada, J.P., Thomassen, M., Weinert, B.T., Bangsbo, J., and Deshmukh, A.S. (2022). High-intensity interval training remodels the proteome and acetylome of human skeletal muscle. eLife *11*, e69802. https://doi.org/10.7554/eLife.69802.

148. Moreno-Justicia, R., Gonzalez-Franquesa, A., Stocks, B., and Deshmukh, A.S. (2022). Protocol to characterize mitochondrial supercomplexes from mouse tissues by combining BN-PAGE and MS-based proteomics. Star Protoc. *3*, 101135. https://doi.org/10.1016/j.xpro.2022.101135.

149. Batth, T.S., Tollenaere, M.X., Rüther, P., Gonzalez-Franquesa, A., Prabhakar, B.S., Bekker-Jensen, S., Deshmukh, A.S., and Olsen, J.V. (2019). Protein aggregation capture on microparticles enables multipurpose proteomics sample preparation. Mol. Cell. Proteomics *18*, 1027–1035. https://doi.org/10.1074/mcp.TIR118.001270.

STAR★METHODS

KEY RESOURCES TABLE

REAGENT or RESOURCE	SOURCE	IDENTIFIER
Antibodies		
Rabbit anti-NAMPT/PBEF/Visfatin	Bethyl Laboratories	Cat# A300-372A
Rabbit anti-COX IV	Abcam	Cat# ab16056; RRID:AB_443304
Goat anti-rabbit IgG (H + L)-HRP conjugate	Bio-Rad	Cat# 1706515; RRID:AB_11125142
Rabbit anti-AMPKγ1	YenZym	YZ5115
Rabbit anti-AMPKγ3	YenZym	YZ4698
APC anti-mouse CD31 clone MEC13.3	Biolegend	Cat# 102510; RRID:AB_312917
APC anti-mouse CD45 clone 30-F11	Biolegend	Cat# 103112; RRID:AB_312977
BV421 anti-mouse Ly-6A/E (Sca-1) clone D7	Biolegend	Cat# 108128; RRID:AB_2563064
PE/Cy7 anti-mouse CD106 (VCAM1) clone 429	Biolegend	Cat# 105719; RRID:AB_2214047
Goat anti-rabbit Alexa Fluor 488 conjugate	Invitrogen	Cat# A11008; RRID: AB_143165
Poly/Mono-ADP Ribose (D9P7Z) anti-rabbit	Cell Signaling Technology	Cat# 89190
Acetylated-Lysine anti-rabbit	Cell Signaling Technology	Cat# 9441; RRID:AB_331805
Chemicals, peptides, and recombinant proteins		
[^{3}H]-2-deoxy-D-glucose	Perkin Elmer	N/A
[U-^{13}C] D-glucose	Cambridge Isotope Laboratories	N/A
[U-^{14}C] D-glucose	Perkin Elmer	N/A
2-hydroxyglutaric acid	Sigma-Aldrich	90790
2-hydroxyglutaric acid-$^{13}C_5$	Cambridge Isotope Laboratories (MA, USA)	CLM-10351
2-methyl-2-butanol	Sigma Aldrich	52463
2-oxoglutaric acid	Sigma-Aldrich	75890
2-oxoglutaric acid-$^{13}C_4$	Cambridge Isotope Laboratories (MA, USA)	CLM-4442
2,2,2-tribromethanol	Sigma Aldrich	T48402
2,7-dichlorofluorescein diacetate PBS solution	Molecular Probes, Eugene	N/A
3′-Dephosphocoenzyme A	Sigma-Aldrich	D3385
5,50-dithiobis (2-nitrobenzoic acid)	Sigma-Aldrich	D8130
5-aminoimidazole-4-carboxamide ribonucleotide	Apollo Scientific	OR1170T
5-HTP (5-Hydroxy-L-tryptophan)	Sigma-Aldrich	N/A
Acetonitrile	Biosolve	01204102
Acetyl-CoA sodium salt	Sigma-Aldrich	A2181
Acetyl coenzyme A trisodium salt	Sigma-Aldrich	A2056
Acetyl-1,2-$^{13}C_2$ coenzyme A lithium salt	Sigma-Aldrich	658650
Acivicin	Sigma-Aldrich	A2295
Adenosine 5′-diphosphate sodium salt	Sigma-Aldrich	A2754
Adenosine 5′-monophosphate monohydrate	Sigma-Aldrich	A2252
Adenosine 5′-triphosphate, 100 mM solution	Thermo Fisher Scientific	10304340
Adenosine-$^{13}C_{10}$ $^{15}N_5$ 5′-monophosphate disodium salt	Sigma-Aldrich	650676
Adenosine-$^{13}C_{10}$ $^{15}N_5$ 5′-triphosphate disodium salt	Sigma-Aldrich	645702
Adenosine-$^{15}N_5$ 5′-diphosphate disodium salt	Sigma-Aldrich	741167
ADP	Merck (Calbiochem)	117105
Alanine	Sigma-Aldrich	A9906
Alanine-13C3, 15N	Cambridge Isotope Laboratories	MSK-A2-1.2
Alcohol dehydrogenase from *Saccharomyces cerevisiae*	Sigma-Aldrich	A7011
alpha-D(+)Mannose 1-phosphate sodium salt hydrate	Sigma-Aldrich	M1755

(*Continued on next page*)

Continued

REAGENT or RESOURCE	SOURCE	IDENTIFIER
alpha-D-Glucose 1-phosphate disodium salt hydrate	Sigma-Aldrich	G1259
AMARA peptide	Anaspec	AS-62596
Ammonium formate ≥99%	VWR Chemicals	84884.180
Amplex UltraRed	Life Technologies	A36006
Amyloglucosidase from *Aspergillus niger*	Merck	A1602
Antimycin A	Sigma-Aldrich	A8674
Arginine	Sigma-Aldrich	A9907
Arginine-13C6, 15N4	Cambridge Isotope Laboratories	MSK-A2-1.3
Aspartic acid-13C4, 15N	Cambridge Isotope Laboratories	MSK-A2-1.4
Asparagine	Sigma-Aldrich	A9908
Asparagine	Sigma-Aldrich	11180
Aspartic acid	Sigma-Aldrich	A9909
Auranofin	Sigma-Aldrich	A6733
Boric acid	Sigma-Aldrich	B6768
Brilliant III Ultra-Fast SYBR Green QPCR Master Mix	Agilent Technologies	600882
Carboxyatractyloside potassium salt	Sigma-Aldrich	C4992
cis-aconitic acid	Sigma-Aldrich	A3412
Citric acid	Acros Organics	AC220340000
Citric acid-D_4	Cambridge Isotope Laboratories (MA, USA)	DLM-3487
Citrulline	Sigma-Aldrich	A9924
Coenzyme A sodium salt hydrate	Sigma-Aldrich	27593
Collagenase, Type II	Gibco	17101015
Corn oil	Sigma-Aldrich	C8267
CountBright Absolute Counting Beads	Invitrogen	C36950
Cystine	Sigma-Aldrich	A9910
Cystine-13C6, 15N2	Cambridge Isotope Laboratories	MSK-A2-1.5
D-Erythrose 4-phosphate sodium salt	Sigma-Aldrich	E0377
D-Fructose 1,6-bisphosphate sodium salt hydrate	Sigma-Aldrich	F4757
D-Fructose 6-phosphate disodium salt hydrate	Sigma-Aldrich	F3627
D-Glucose 6-phosphate disodium salt hydrate	Sigma-Aldrich	G7250
D-Glycerate 2-phosphatesodium salt	Sigma-Aldrich	79470
D-Glycerate 3-phosphate disodium salt	Sigma-Aldrich	P8877
Diaphorase from *Clostridium kluyveri*	Sigma-Aldrich	D5540
Dihydroxyacetone phosphate lithium salt	Sigma-Aldrich	37442
Dispase II (neutral protease, grade II)	Roche	4942078001
DL-Glyceraldehyde 3-phosphate solution	Sigma-Aldrich	G5251
D-Mannose 6-phosphate disodium salt hydrate	Sigma-Aldrich	M6876
D-Ribofuranose 5-phosphate disodium salt	Sigma-Aldrich	R7750
D-Ribulose 1,5-bisphosphate sodium salt hydrate	Sigma-Aldrich	R0878
D-Ribulose 5-phosphate disodium salt	Sigma-Aldrich	83899
D-Sedoheptulose-7-phosphate barium salt	Santa Cruz Biotechnology	sc-285389
D-Xylulose 5-phosphate lithium salt	Sigma-Aldrich	15732
FCCP	Sigma-Aldrich	C2920
Formic acid 0.1%	Biosolve	23244102
Formic acid 0.1% in acetonitrile	Biosolve	01934102
Formic acid 99%	Biosolve	06914143
fumaric acid	ICN Biomedicals Inc.	101742
fumaric acid-$^{13}C_4$	Cambridge Isotope Laboratories (MA, USA)	CLM-1529
GABA	Sigma-Aldrich	A2129

(*Continued on next page*)

Continued

REAGENT or RESOURCE	SOURCE	IDENTIFIER
GABA-13C4	Cambridge Isotope Laboratories	CLM-8666-0
Glucose-6-phosphate dehydrogenase from *Saccharomyces cerevisiae*	Sigma-Aldrich	G6378
Glutamate	Sigma-Aldrich	G1626
Glutamic acid	Sigma-Aldrich	A9911
Glutamic acid-^{13}C5, 15N	Cambridge Isotope Laboratories	MSK-A2-1.6
Glutamine	ICN Biomedicals Inc	101806
Glutamic-oxalacetic transaminase from porcine heart	Sigma-Aldrich	G2751
Glyceric acid	Sigma-Aldrich	367494
Glycine	Sigma-Aldrich	A9912
Glycine-^{13}C2, 15N	Cambridge Isotope Laboratories	MSK-A2-1.7
Glycolic acid	Merck	104106
H_20	Biosolve	23214102
HEPES buffer	Sigma-Aldrich	H3375
Histidine	Sigma-Aldrich	A9913
Hoescht 33342	Thermo Fisher Scientific	N/A
Horse radish peroxidase	Sigma-Aldrich	P8250
Immobilon-P PVDF Membrane	Millipore	IPVH00010
Inosine 5′-monophosphate disodium salt hydrate	Sigma-Aldrich	57510
Isocitric acid	Sigma-Aldrich	I1252
Isoleucine	Sigma-Aldrich	A9914
Isoleucine-^{13}C6, 15N	Cambridge Isotope Laboratories	MSK-A2-1.9
Isopropanol	Biosolve	16264102
Itaconic acid	Merck	8,04812
Kynurenin	Sigma-Aldrich	K8625
Lactic acid	Alfa Aesar	L13242
Lactic acid-$^{13}C_3$	Cambridge Isotope Laboratories (MA, USA)	CLM-1579
L-Asparagine-^{13}C4	Cambridge Isotope Laboratories	CLM-8699-H
L-Citrulline-4,4,5,5-D4	Cambridge Isotope Laboratories	DLM-6039
Leucine	Sigma-Aldrich	A9915
Leucine-^{13}C6, 15N	Cambridge Isotope Laboratories	MSK-A2-1.10
L-Glutamine-^{13}C5	Cambridge Isotope Laboratories	CLM-1822
L-histidine-^{13}C6, 15N3	Cambridge Isotope Laboratories	MSK-A2-1.8
L-Kynurenine-D6	Cambridge Isotope Laboratories	DLM-7842
L-Ornithine-D6	Cambridge Isotope Laboratories	DLM-2969
Luminata Immobilon Forte Western HRP Substrate	Millipore	WBLUF0100
Lysine	Sigma-Aldrich	A9916
Lysine-^{13}C6, 15N2	Cambridge Isotope Laboratories	MSK-A2-1.11
Magnesium Green, Pentapotassium Salt, cell impermeant	Thermo Fischer Scientific	M3733
Malate	Sigma-Aldrich	M1000
Malate dehydrogenase from porcine heart	Sigma-Aldrich	442610
Malic acid	Sigma-Aldrich	100382
Malic acid-$^{13}C_4$	Cambridge Isotope Laboratories (MA, USA)	CLM-8065
Malonyl coenzyme A lithium salt	Sigma-Aldrich	685518
Malonyl-$^{13}C_3$ coenzyme A lithium salt	Sigma-Aldrich	655759
Methionine	Sigma-Aldrich	A9917
Methionine-^{13}C5, 15N	Cambridge Isotope Laboratories	MSK-A2-1.12

(*Continued on next page*)

Continued

REAGENT or RESOURCE	SOURCE	IDENTIFIER
NA-D4	CDN Isotopes	D4368
Nam-D4	CDN Isotopes	D-3457
NAD-D4,	TRC	N407783
MeNam-D4	CDN Isotopes	D-7642
NADH-D4	TRC	N201487
NAD^+	Sigma-Aldrich	N0632
NADH	Sigma-Aldrich	N8129
$NADP^+$	Sigma-Aldrich	N5755
NADPH	Sigma-Aldrich	N7505
Nagarse, proteinase from *Bacillus licheniformis*	Sigma-Aldrich	P8038
NativePAGE 3 to 12%, Bis-Tris, 1.0 mm, Mini Protein Gels	Invitrogen	BN1001BOX
N-ethylmaleimide	Sigma-Aldrich	E1271
OCT TissueTec	Sakura Finetek	4583
Oligomycin	Sigma-Aldrich	O4876
Ornithine	Sigma-Aldrich	A9925
Oxalic acid	Sigma-Aldrich	194131
Oxaloacetic acid	Sigma-Aldrich	171255
Oxaloacetic acid	Sigma-Aldrich	O4126
P1,P5-Di(adenosine-5′) pentaphosphate pentasodium salt	Sigma-Aldrich	D4022
Perchloric acid	Sigma-Aldrich	100519
Phenylalanine	Sigma-Aldrich	A9918
Phenylalanine-^{13}C9, 15N	Cambridge Isotope Laboratories	MSK-A2-1.13
Proline	Sigma-Aldrich	A9919
Proline-^{13}C5, 15N	Cambridge Isotope Laboratories	MSK-A2-1.14
ProLong Glass Antifade Mountant	Thermo Fisher Scientific	P36980
Pyruvate	Sigma-Aldrich	P2256
Pyruvic acid	Sigma-Aldrich	107360
Pyruvic acid-$^{13}C_3$	Cambridge Isotope Laboratories (MA, USA)	CLM-2440
Quick Start Bradford 1x Dye Reagent	Bio-Rad	5000205
RNase A	Thermo Fisher Scientific	EN0531
Rotenone	Sigma-Aldrich	R8875
Ruthenium red	Sigma-Aldrich	557450
Serine	Sigma-Aldrich	S4500
Serine	Sigma-Aldrich	A9920
Serine-^{13}C3, 15N	Cambridge Isotope Laboratories	MSK-A2-1.15
SIGMAFAST Protease Inhibitor	Sigma-Aldrich	S8820
SPLASH LIPIDOMIX Mass Spec Standard	Merck	330707
Succinate	Sigma-Aldrich	S2378
Succinic acid	Merck	100681
Succinic acid-D_4	Sigma-Aldrich	293075
Succinyl coenzyme A sodium salt	Sigma-Aldrich	S1129
Sucrose 6'-monophosphate dipotassium salt	Sigma-Aldrich	S3387
Superoxide dismutase	Sigma-Aldrich	S8160
Tamoxifen	Sigma-Aldrich	T5648
Tetramethylrhodamine methyl ester perchlorite	Sigma-Aldrich	T5428
Threonine	Sigma-Aldrich	A9921
Threonine-^{13}C4, 15N	Cambridge Isotope Laboratories	MSK-A2-1.16
Trehalose 6-phosphate dipotassium salt	Sigma-Aldrich	T4272

(*Continued on next page*)

Continued

REAGENT or RESOURCE	SOURCE	IDENTIFIER
Trizma Base	Sigma-Aldrich	T4661
Trizma Hydrochlorid-hydrochlorid	Sigma-Aldrich	108315
TRIzol reagent	Thermo Fisher Scientific	15596026
Tryptophan	Sigma-Aldrich	A9926
Tryptophan-D5	CDN Isotopes	D-7416
Tryptophan-D8	Cambridge Isotope Laboratories	DLM-6903
Tyrosine	Sigma-Aldrich	A9922
Tyrosine-^{13}C9, 15N	Cambridge Isotope Laboratories	MSK-A2-1.17
Valine	Sigma-Aldrich	A9923
Valine-^{13}C5, 15N	Cambridge Isotope Laboratories	MSK-A2-1.18
Vectashield mounting medium	Vector Laboratories	H-1000
ZombieYellow dye	Biolegend	423103
Critical commercial assays		
RNeasy Kit mini	Qiagen	74104
Lactate Pro 2	Arkray	LT-1730
Contour XT	Bayer	C2 84157385
Ultra-Sensitive Mouse Insulin ELISA Kit	Crystal Chem	90080
Pierce BCA Protein Assay Kit	Thermo Scientific	23227
iScript cDNA Synthesis Kit	Bio-Rad	1708890
GOD-PAP glucose assay	Randox	GL364
DNeasy Blood & Tissue Kit	Qiagen	69504
RNase-Free DNase Set	Qiagen	79254
NativePAGE Sample Prep Kit	Invitrogen	BN2008
Deposited data		
RNA-seq at GEO	This paper	GEO: GSE273462
DNA methylation at GEO	This paper	GEO: GSE282353
Lipidomics data at Metabolomics Workbench	This paper	NMDR: ST003703
Proteomics data at Pride Proteome Exchange	This paper	PRIDE: PXD061221
Experimental models: Organisms/strains		
Mouse: B6.BomTac-Tg(HSA-creMCM)-*Nampt*^{tm1Jtree}	This paper	N/A
Mouse diet: chow	Altromin	1310
Mouse diet: chow	SAFE Diets	D30
Mass spectrometry columns/equipment		
ACQUITY Premier CSH (2.1 × 100 mm, 1.7 μM) column	Waters	186009461
ACQUITY UPLC CSH C18 VanGuard Pre-column (2.1 × 5 mm, 1.7 μM)	Waters	186005303
iHILIC-(P) Classic, 50×2.1 mm, 5 μm	HILICON AB	160.052.0520
BEH C18, 100×2.1 mm, 1.7 μm	Waters	176000864
ACQUITY Premier BEH Amide column	Waters	186009509
HSS T3, 100×2.1 mm, 1.7 μm	Waters	186009468
Oligonucleotides		
Oligonucleotides used for real-time quantitative PCR, Table S2	This paper	N/A
Software and algorithms		
ImageJ (Fiji)	Schneider et al.[95]	https://imagej.nih.gov/ij/
Prism 10	GraphPad Software	https://www.graphpad.com
MATLAB R2023a	MathWorks	https://www.mathworks.com/products/matlab.html

(*Continued on next page*)

Continued

REAGENT or RESOURCE	SOURCE	IDENTIFIER
Bio-Rad CFX Maestro	Bio-Rad	https://www.bio-rad.com/en-dk/product/cfx-maestro-software-for-cfx-real-time-pcr-instruments?ID=OKZP7E15
Spectronaut version 18.4	Biognosys AG	https://biognosys.com/software/spectronaut/
ExpeData	Sable Systems International	https://www.sablesys.com/products/classic-line/expedata-p-data-analysis-software/#product-downloads
MaxQuant version 2.1.4.0	Cox and Mann[96]	https://www.maxquant.org/maxquant/
Perseus	Tyanova et al.[97]	https://www.maxquant.org/perseus/
FlowJo version 10.8	BD Life Sciences	https://www.flowjo.com/solutions/flowjo/downloads
R version 4.3.1	R Foundation	https://cran.r-project.org/bin/windows/base/old/4.3.1/

EXPERIMENTAL MODEL AND SUBJECT DETAILS

Transgenic mouse strains and animal housing

All animal experiments were performed following the European directive 2010/63/EU of the European Parliament and the Council of the protection of animals used for scientific purposes, approved by the Danish Animal Experiments Inspectorate (license numbers: 2015-15-0201-00796, 2018-15-0201-01493, 2020-15-0201-00764). Previously generated homozygous *Nampt*-floxed carrying mice (*Nampt*^{tm1Jtree})[98] were crossed with animals heterozygous for the inducible human α-skeletal actin promoter-driven *MCM Cre* (HSA^{CreMCM}).[99] After induction, Cre$^{+/-}$ mice were knockouts (i.e., iSMNKO), while the Cre$^{-/-}$ littermates were used as controls. All animals used in the experiments were on the C57BL/6JBomTac background (Taconic, Denmark). Both iSMNKO and control animals at the age of 9-15 weeks were dosed orally with 2 mg/day of tamoxifen (Sigma-Aldrich T5648) suspended in corn oil (Sigma-Aldrich C8267) for three consecutive days. All animals were housed in standard conditions with controlled temperature (22 +/- 1°C), 12 h light-dark cycle and received water and chow diet (Altromin 1310 or equivalent SAFE DS D30) *ad libitum*. Experiments were performed on 16-25-week-old male mice unless stated otherwise.

METHOD DETAILS

Body composition

Animal body composition was determined with an NMR scanner (EchoMRI 4-1; EchoMRI). Fat and lean mass were presented as a percentage of body weight.

Treadmill running: acclimation, exercise tolerance test (power test (PWT)), and moderate-intensity exercise bout

Acutely exercised animals were used for several experiments in the current study. In preparation for those experiments, mice were familiarized with treadmill (Exer 3/6 Treadmill (Columbus Instruments, USA)) running for 3 days (day 1: 5 min, no running; day 2: 5 min, belt speed 6 m/min, 5 min at 10 m/min, no electric grid stimulation; day 3: 2 min at 6 m/min, 3 min at 10 m/min, 2 min from 10 to 16 min, 3 min 16 m/min, electric grid at 1 Hz, 0.1 mA). Two days after acclimation, animals were used for experiments. The treadmill belt inclination was set to 10°. Exercise tolerance test (Power test) was performed on non-fasted animals roughly in the middle of the light phase at ZT 6. The running protocol included a warm-up stage (5 min at 6 m/min, 5 min at 10 m/min, 3 min at 12 m/min, 3 min at 14 m/min) and a test stage (speed increased by 2 m/min every 3rd min). The treadmill belt inclination was set to 10°, and the electric grid stimulation was at 3 Hz and 1.5 mA. A mouse was deemed fatigued when it did not resume running after three consecutive stimuli (contact with the electric grid or a gentle nudge). After running, the animals were returned to their home cages, and in some experiments their tail blood was drawn for direct lactate (Lactate Pro 2, Arkray, Japan) and glucose (Contour XT, Bayer, Germany) checks. Moderate intensity running bout consisted of a brief warm-up (2 min at 6 m/min, 2 min at 10 m/min, 1 min from 10 to 16 m/min) and a 30 min-long steady running stage (10 min at 16 m/min followed by 20 min at 18 m/min). The treadmill belt inclination was set to 10°, and the electric grid stimulation was at 3 Hz and 0.5-1.0 mA. In post-exercise TSE indirect calorimetry experiment as well as in glucose oxidation experiment, mice ran for a 1 hour at moderate speed. As such, the running bout consisted of a warm-up (2 min at 6 m/min, 2 min at 10 m/min, 1 min from 10 to 16 m/min) and a 55 min-long steady stage at 16 m/min, with other parameters set to as described above.

Graded maximal (GRM) exercise performance test

The GRM test was performed on non-fasted animals at ZT5-7. Insulated Maze Engineers single-lane automated treadmills (MazeEngineers, USA) combined with Sable Promethion gas analyzer systems (Sable Systems, USA) were used to record animal respiration during running. Prior to the test, animals were familiarized with treadmill running as described above. The treadmill belt inclination was set to 15°. The protocol included a warm-up stage (2 min at 6 m/min, 2 min at 9 m/min, 2 min at 12 m/min, 2 min at 15 m/min) and a test stage (1 min at 18 m/min, 1 min at 21 m/min, followed by a 1 m/min increase every minute till the end of the test).[100] Similarly to the PWT described above, an animal was considered fatigued when it was no longer able to re-engage in running after receiving 3 consecutive stimuli (contact with the electric grid at the back of the treadmill belt, set to 3 Hz, 1.0 mA). Animals were tested in randomly assigned pairs and their respiration was recorded before (basal), during and right after (immediate recovery) the completion of the test. VO_{2peak} was determined as the maximal rate of oxygen consumption measured during exercise.

In vivo exercise-induced muscle glucose uptake

Animals received an intraperitoneal injection of [^{3}H]-2-deoxy-D-glucose (8 mL/kg, 2.22 MBq/mL, Perkin Elmer, USA) 20 min prior to the exercise bout.[101,102] Then, mice from the exercise group ran at moderate intensity for 35 min (the running protocol is described above). Sedentary animals were placed on mock treadmills for the duration of the exercise bout. Blood was sampled from the tail vein to measure glucose levels (Contour XT, Bayer, Germany) shortly before and after the completion of the exercise bout. Animals were euthanized by cervical dislocation; muscle tissue was dissected and snap-frozen in liquid nitrogen. Muscle 2-DG uptake was determined as [^{3}H]-2-deoxy-D-glucose-6-phosphate content via the Somogyi and perchloric acid precipitations of QUAD muscle homogenates, as previously described.[103] The radioactivity in the lysates was measured by liquid scintillation counting (Hidex 300SL, Hidex, Finland). The experiment was performed at ZT3-6.

Sable Promethion indirect calorimetry

Animals of both genotypes were single-housed in metabolic Sable Promethion Core cages (Sable Systems, USA) with or without running wheels (n=8). Gas exchange, food and water intake, wheel-running, ambulatory activity and inactivity were recorded for 3 weeks. The data were analyzed with One-Click macro (TimeSeries, Macro 13 and Ethoscan) following the recommendations provided in the Data Analysis Guide, Promethion, Sable Systems.

TSE indirect calorimetry after an acute exercise bout

Control and knockout mice (n=8) were single-housed into TSE metabolic cages and allowed to acclimate to the new environment for 4 days before the start of the measurements. During the same period, the animals were familiarized with treadmill running as described above. Then, oxygen consumption, carbon dioxide production, food intake and ambulatory activity were measured with the LabMaster system (TSE Systems) for three following days (basal, rested state). After that, mice ran on a treadmill for 1 h, at 16 m/min, 10° inclination (more details in the protocol described above). Running took place in the middle of the light phase, around ZT7. After running, the animals were returned to their home cages and the data were collected for the next four days. The collected gas exchange data were used to calculate RER and EE.

Glucose (oral), AICAR (intraperitoneal) tolerance tests and blood insulin

Mice were fasted for four hours (8:00-12:00), after which 2 g/kg body weight glucose solution (25% glucose solution in sterile water) was administered via oral gavage.[104,105] Glucose levels in the tail-drawn blood were measured with a test-strip-based glucometer (Contour XT, Bayer) in the basal state and 5, 15, 30, 45, 60, 90, 100 and 120 min after glucose administration. Samples for insulin measurement were collected in the basal state and 5, 15, 30, 45 and 60 min after glucose injection. A commercial insulin ELISA kit (Ultra-Sensitive Mouse insulin ELISA Kit, Crystal Chem, #90080) was used to measure the whole-blood insulin following the manufacturer's manual with the broad range calibration curve. AICAR tolerance test was performed by administering 5-aminoimidazole-4-carboxamide ribonucleotide (Apollo Scientific, #OR1170T) or vehicle (sterile saline) intraperitoneally to fasted mice at 250 mg/kg body weight. Tail blood was drawn every 15 min for 2 h and glucose concentration was assessed as described above.

Ex vivo muscle contractility assay

The setup was similar to the one described previously.[29] Briefly, SOL and EDL muscles were obtained from 23-week-old (12 weeks after tamoxifen) control and mutant animals anesthetized with an intraperitoneal injection of Avertin (2,2,2-Tribromoehtanol and 2- methyl-2-butanol (Sigma Aldrich #T48402 and #152463)). Measurements were performed in Krebs-Ringer buffer supplemented with 0.1% bovine serum albumin, 8 mM mannitol, and 5 mM glucose (117 mM NaCl, 4.7 mM KCl, 2.5 mM $CaCl_2$, 1.2 mM KH_2PO_4, 1.2 mM $MgSO_4$, 24.6 mM $NaHCO_3$), which was kept oxygenated (95% O_2, 5% CO_2) and warmed to 30°C. DMT 820MS myograph system (Denmark) was used to record muscle force outputs. Prior to measurement, the optimal muscle length was determined. It was considered optimal when the maximal isometric twitch response was achieved (pulse voltage 12 V, pulse width 0.5 ms). Maximal single twitch force (the average of three twitches separated by > 30 s, 12 V, pulse width 0.5 ms) was assessed by measuring peak isometric twitch force along with the time to peak twitch force and the half-relaxation time. The area under the curve derived from the tetanic contraction data (pulse voltage 12 V, pulse width 0.2 ms, interval 6.50 ms, frequency 150 Hz, 75 pulse counts in each train, 540 ms total train time, 5,000 ms pause between trains for a total of 55 trains for soleus and 23 for EDL) was determined by summating the products of peak force and contraction duration from each tetanic contraction. Two consecutive rounds of tetanic

contraction per muscle were conducted to determine force recovery. All absolute force measurements were normalized using a muscle cross-sectional area (CSA) to find specific force. Muscle CSA was determined as described previously.[106]

^{13}C-labelled CO_2 release at rest and after exercise

Rate of ^{13}C-labelled CO_2 release at rest: 4 mg of [U-^{13}C] D-glucose (Cambridge Isotope Laboratories, USA) tracer in saline was orally gavaged to control and iSMNKO mice after a 4-hour-long fast (8:00-12:00). Animals were returned to their home cages with no access to food and water, and ^{13}C levels were measured in their exhaled CO_2 during the next 5 hours (Stable Isotope Gas Analyzer with Promethion Core system, Sable Systems, USA). Rate of ^{13}C-labelled CO_2 release after an exercise bout: the control and iSMNKO mice after a 4-hour-long fast (8:00-12:00) were exercised on a treadmill following a 1-hour-long protocol, as described above. At the end of a running bout, animals received an oral gavage with 4 mg of ^{13}C-uniformly labelled D-glucose (Cambridge Isotope Laboratories, USA) tracer and were returned to their home cages. Access to food and water was closed during the measurement, which lasted for the next 4 hours.

Mitochondria isolation

Mitochondrial fraction was isolated from muscle tissue with nagarse digestion and differential centrifugation, as previously described.[49,107] Briefly, 100 mg of the freshly dissected muscle tissue was homogenized after mechanical (crude) and enzymatic digestion. Followed by two centrifugation steps, the mitochondria-enriched pellet was washed, resuspended, and its protein content was determined with the Bradford method (BioRad #5000205). After the final centrifugation, the mitochondrial pellet was either snap-frozen in liquid nitrogen or suspended in an appropriate assay buffer. When a large quantity of mitochondrial material was required (more than 250 μg), isolation was performed on up to 1 g of muscle tissue per isolation round, with the according upscaling of the reagents volumes.

Ca^{2+}-induced mitochondria swelling assay

The assay was performed according to a previously published method.[29,108] Briefly, 20 μg of muscle mitochondria were resuspended in 200 μL of 150 mM KCl, 5 mM HEPES, and 2 mM K_2HPO_4, pH 7.2 buffer, and absorbance was monitored at λ540 nm (Hidex Sense plate reader, Hidex, Finland). The swelling response was induced with the addition of either 100 μM or 400 μM $CaCl_2$, and the absorbance was recorded for 40 min at 30 s intervals. Absorbance in basal, unstimulated state was first normalized to the sample protein content and then was used for normalization of the calcium-induced response rates.

Malate-aspartate shuttle activity

The assay is based on the previously published method.[109,110] Mitochondria (20 μg) were re-suspended in the assay buffer (75 mM mannitol, 25 mM sucrose, 5 mM Tris-H_3PO_4, 20 mM Tris-HCl, 0.5 mM EDTA, 100 mM KCl, pH 7.4) containing 4 U/mL aspartate aminotransferase, 6 U/mL malate dehydrogenase, 5 mM aspartate, 5 mM malate, 0.5 mM ADP, 200 nM ruthenium red and 50 uM NADH. The NADH autofluorescence decay was recorded at λ360 +/- 10 nm over λ460 +/- 15 nm (CLARIOstar Plus, SMG Labtech, Germany). The MAS activity was initiated by the addition of 5 mM glutamate and was measured for 30 min at 30 s intervals. The linear parts of the NADH decay curves were used to calculate the activity rates.

Incubation of mitochondria for NAD assays

Mitochondria obtained from quadriceps muscle of the control and knockout animals (200 μg protein) was suspended in warm MiR05 respiratory buffer with (st3) or without (st4) 400 mM malate, 2 M glutamate, 2.5 M pyruvate and 500 mM ADP, and incubated with agitation (500 rpm) for 7 min in open tubes. Samples were spun quickly in a pre-cooled centrifuge, re-suspended and lysed immediately with 0.6 M perchloric acid (PCA) or 0.1 M NaOH for NAD^+ and NADH measurements, respectively. NAD extracts were buffered with 100 mM Na_2HPO_4 (pH 8), while 10 mM Tris-HCl (pH 6) was used to dilute the NADH extracts. Diluted samples were then frozen and stored at -80°C. Protein pellets left from the PCA extraction were solubilized in 0.2 M NaOH with heating (95°C, 10 min) and used to measure the protein content with bicinchoninic acid assay (Thermo Fisher Scientific #23227).

High-resolution respirometry on permeabilized muscle fibers

Rates of oxygen consumption (OCR) were measured on permeabilized fibres from quadriceps and soleus muscles, following a standard protocol using Oxygraphs-O2k (Oroboros Instruments, Austria). MiR05 respiratory buffer was supplemented with substrates (2 mM malate, 10 mM glutamate and 5 mM pyruvate), followed by 0.1 mM and 5.0 mM ADP additions. Cytochrome c was added to check for the outer membrane integrity. Next, 10 mM succinate was added to achieve the maximal coupled complex I+II respiration. The protocol was concluded with the inhibition of respiration with 2.5 μM antimycin A. Measurements were conducted at high oxygen levels (450-200 nmol/mL) with the chamber temperature set to 37°C and each sample was assayed in duplicate. OCR data were normalized to wet muscle fiber weight (mg).

High-resolution respirometry on quadriceps mitochondrial fraction with inner mitochondrial membrane potential (IMMP) and ATP synthesis rate

Mitochondria isolated from quadriceps muscle were used for measurements of IMMP, ATP synthesis rate and OCR with an O2k-FluoRespirometer (Oroboros Instruments, Austria). All measurements were performed in mitochondrial respiration medium, MiR05

(Oroboros Instruments, Austria). To assess IMMP at different respiratory states, 500 nM tetramethylrhodamine methyl ester perchlorite (TMRM) (Sigma-Aldrich #T5428) was added to MiR05 (unquenching mode). TMRM fluorescence was detected using Fluorescence-Sensor Green, Filter Set AmR, with the following settings: light intensity: Amp Polarization voltage = 200, Amp Gain = 1000. To evaluate mitochondrial respiration and IMMP, respiratory substrates, uncouplers, and inhibitors were titrated into O2k chambers as described in SUIT-01 Fluo mt D036 protocol, Bioblast,[111] with modifications, and TMRM fluorescence and respiratory rates were measured. Briefly, 2 mM malate, 5 mM pyruvate and 10 mM glutamate additions were first injected into the O2k chambers to assess leak respiration, followed by ADP titration (0.01 mM, 0.05 mM, 0.1 mM and 5.0 mM) and 10 mM succinate injection. Subsequently, ATP synthesis was inhibited with oligomycin (Omy, 2.5 μM) to achieve maximal IMMP. Maximal respiratory capacity and lowest IMMP values were induced by titration of FCCP. The protocol was finished with a titration of 2.5 μM rotenone (maximal flux through complex II, without complex I) and complete mitochondrial respiration inhibition by 2.5 μM antimycin A. TMRM fluorescence values were converted to TMRM concentration using TMRM calibration curves (separate for each O2k chamber and fluorescence sensor pair used in the experiment). TMRM concentrations were converted into IMMP in mV as described previously.[112] The total amount of oxygen consumed per ADP bolus was calculated as area under the curve (O_2 over time) with python script *find_peaks* function from the SciPy signal library.

To evaluate the rate of ATP synthesis in respiring mitochondria, 1.1 μM Magnesium Green dye M3733 (Magnesium Green, Pentapotassium Salt, cell impermeant, Thermo Fischer Scientific) was used.[113,114] Magnesium Green fluorescence was measured with Fluorescence-Sensor Blue/Filter Set MgG/CaG, with the following settings: light intensity: Amp Polarization voltage = 500, Amp Gain = 1000. Modified Mir05 buffer containing 1 mM $MgCl_2$ supplemented with 50 μM inhibitor of adenylate kinase P1,P5-Di(adenosine-5') pentaphosphate (Ap5A) was used to avoid ATP degradation. Titrations of the respiratory substrates, uncoupler, and inhibitors were performed as described above with the exception that adenine nucleotide translocator inhibitor carboxyatractyloside (5.5 μM) was used to inhibit ATP synthesis instead of antimycin A at the final stage of the protocol. To assess the ATP production rate, calibration curves were generated by performing titrations of $MgCl_2$, ATP or ADP in presence of Magnesium Green as described in the following DLP files: MgG_Calibration_and_Kd_determination_ADP_Mg.DLP and MgG_Calibration_and_Kd_determination_ATP_Mg.DLP in DatLab 7.4. Using the generated values, the dissociation constants (K_d) of ADP and ATP to Mg_2^+ were calculated with an Excel template provided by Oroboros instruments located in the folder DL-Protocols\Instrumental of DatLab 7.4: Template_MgG_Calibration_and_Kd_determination_ADP_and_ATP_to_Mg.

From there, the ATP production rate was determined by using the K_d data and an Excel template provided by Oroboros instruments located in the folder DL-Protocols\Instrumental of DatLab 7.4: ''Template – MgG_ATP_production_analysis_prepared''.

(Hydro)peroxide production, I_Q + O_F RET and I_F mitochondrial H_2O_2 flux *in vitro*

Maximal hydrogen peroxide and lipid hydroperoxides (H_2O_2+LOOH) flux was assessed on quadriceps muscle fibers, as described previously.[115] Their emission was monitored via 50 μM Amplex UltraRed (Life Technologies #A36006) fluorescence detection (λ560 nm / λ590 nm) and was stimulated by supplying substrates for complex I+II: 5 mM pyruvate, 2 mM malate and 1 mM succinate in presence of 10 g/mL oligomycin. The emission rate was converted to H_2O_2 production using a standard curve. Mitochondrial H_2O_2 fluxes through I_Q and I_F + O_F sites were measured on muscle mitochondria following the method described previously.[116,117] Briefly, 100 μg/mL of isolated mitochondria were suspended in buffer D (105 mM potassium-MES, 30 mM KCl, 10 mM KH_2PO_4, 5 mM $MgCl_2$, 1 mM EGTA, 2.5 g/l BSA, pH = 7.2) supplemented with 25 μM Amplex UltraRed (Life Technologies #A36006), 1 U/mL horseradish peroxidase, 20 U/mL superoxide dismutase and 100 μg/mL auranofin. Fluorescence was recorded at +37°C with a Hidex Sense plate reader (Hidex, Finland) at λ544 +/- 10 nm over λ595 +/- 5 nm. Mitochondrial H_2O_2 flux through I_Q was assayed in the presence of 10 mM succinate and 1 μM oligomycin (RET ROS). In parallel, the same substrates, but in the presence of 1 μM rotenone, were used to measure the I_Q-independent ROS generation. The rates of H_2O_2 emission were calculated by the use of a standard curve, and the rotenone-independent ROS rates were subtracted from the RET rates. Similarly, rate of H_2O_2 emission at the I_F + O_F sites was measured with 2 mM malate, 10 mM glutamate, 1 μM oligomycin and 1 μM rotenone. Calibration performed under matching conditions was used to convert Amplex UltraRed signal into H_2O_2 flux.

Targeted quantification of intermediates of glycolysis, TCA, pentose phosphate pathway and amino acids by combined liquid chromatography tandem mass spectrometry

Metabolites were extracted from app. 20 mg of muscle pulverized tissue in 1 mL of $CHCl_3$/H_2O/MeOH (20/20/60, *v/v/v*) by shaking with tungsten carbide beads at 30 kHz for 3 min. Subsequently, the bead was removed from each sample and the samples were centrifuged at 14,000 *g* for 10 min and the supernatant was transferred into the LC vials and split for analysis of (i) free amino acids, (ii) phosphorylated sugars, and (iii) nucleotides and coenzymes (50 μL were taken for amino acids analysis, 300 μL for phosphorylated sugar analysis, 200 μL for 3-NPH derivatized carboxylates, and 300 μL for the HILIC analysis) and all extracts were dried on a centrifugal concentrator (Thermo Fisher Scientific, Waltham, USA). The metabolites analyzed are listed in Table S1. The quality control samples were prepared by pooling 30 μL of each sample. The TCA carboxylates were derivatized and analyzed as in Hodek et al.[118] Briefly, the dried extracts were dissolved in 20 μL of 50% MeOH containing isotopically labelled internal standards for majority of carboxylic acids with exception of *cis*-aconitate, isocitrate, itaconate, and oxaloacetate (these acids were quantified based on an external calibration curve). Following this, derivatization was conducted by the addition of 20 μL of 200 mM 3-NPH and 120 mM EDC, samples were incubated for 1 h at room temperature and the reaction was quenched by addition of 40 μL of 0.05 mg/mL BHT in pure methanol. The separation was achieved by injecting 5 μL of a sample to an analytical column (HSS T3, 100×2.1 mm,

1.7 μm, Waters, Milford, MA, USA). The gradient elution was conducted with a mobile phase consisting of (A) 0.1% formic acid in water and (B) 0.1% formic acid in acetonitrile at a flow rate of 0.35 mL/min with the following gradient program: 0 min (5% B), 12 min (100% B), 13 min (100% B), 14 min (5% B), 17 min (5% B). For measurement of nucleotides and coenzymes, the dried extracts were dissolved in 20 μL of 50% MeOH containing a mix of 10 μM internal standards. The nucleotides and coenzymes were analyzed by injection of 3 μL of an extract into an analytical column (iHILIC-(P) Classic, 50×2.1 mm, 5 μm, HILICON AB, Umeå, Sweden). The mobile phase consisted of (A) 10 mM ammonium acetate in water and (B) 10 mM ammonium acetate in 90/10 acetonitrile/water, and was delivered to the column by a flow rate of 0.35 mL/min at the following gradient: 0 min (85% B), 5 min (60% B), 7 min (30% B), 8 min (30% B), 9 min (85% B), 15 min (85% B). the free amino acids were quantified after derivatization with AccQ-Tag reagent (Waters, Milford, MA, USA) as follows: The dried extracts were dissolved in 20 μL of 20 mM HCl and 60 μL of borate buffer containing the internal standards and norvaline were added. Finally, 20 μL of AccQ-Tag reagent was added to each sample and the samples were vortex mixed then incubated at room temperature for 10 min, followed by incubation at 55°C for 10 min. The derivatized amino acids were analyzed by injection of 1 μL of a sample into an analytical column (BEH C18, 100×2.1 mm, 1.7 μm, Waters, Milford, MA, USA). The samples were eluted with a gradient elution of the mobile phase consisting of (A) 0.1% formic acid in water and (B) 0.1% formic acid in acetonitrile at the following gradient: 0 min (0% B), 0.54 min (0% B), 3.5 min (9.1% B), 7 min (17% B), 8 min (19.7% B), 8.5 min (19.7% B), 9 min (21.2% B), 10 min (59.6% B), 11 min (95% B), 11.5 min (95% B), 12 min (0% B), 15 min (0% B). The phosphorylated sugars were subjected to a two-step derivatization according to Rende et al.[119] Briefly, the dried extract was derivatized with 20 μL of methoxyamine for 30 min at 60°C and incubated overnight at room temperature. Then, 12 μL *N*-methylimidazole and 6 μL of propionic acid anhydride were added and the extracts were kept at 37°C for 30 min. Finally, samples were dried down to 10 μL and they were mixed with 90 μL of 0.1% formic acid in water and 1 μL was injected onto the analytical column (BEH C18, 100×2.1 mm, 1.8 μm, Waters, Milford, MA, USA). Quantification of all metabolites was achieved on an LC-MS/MS system consisting of an Agilent 1290 UHPLC connected to an Agilent 6490 triple quadrupole (Agilent, CA, USA) operated in the multiple reaction monitoring mode (MRM).

Post *in situ* contraction muscle glycogen content, utilization and resynthesis rates

Contraction of GAS, SOL, TA, and EDL *in situ* was achieved by the direct electrical stimulation of the sciatic nerve, performed on pentobarbital (70 mg/kg) anaesthetized mice. The animals were fasted for 4 h prior to the start of the experiment. The unilateral stimulation was applied for 15 min and consisted of 0.5 ms trains starting every 1.5 sec with 5 V, pulse width 0.1 ms at 100 Hz. To assess the effect of contraction on muscle and liver glycogen content, the stimulation protocol was performed on one half of the cohort. The other half served as rested controls. All mice were euthanized by cervical dislocation immediately after 15 min of contraction/rest. When measuring the post-contraction muscle glucose uptake, a 3 mg/mouse glucose bolus with 0.74 MBq/mouse [^{3}H]-2-deoxy-D-glucose (Perkin Elmer, USA) was injected retro-orbitally right at the end of the contraction bout. Twenty min later, muscle tissue was harvested and snap-frozen in liquid nitrogen. Blood glucose levels were monitored with a glucometer (Contour XT, Bayer) and tail blood samples were collected every 5 min to assess the tracer disappearance rates. Collected samples (blood and muscle) were processed as described above (*in vivo* exercise-stimulated muscle glucose uptake). To study the glycogen incorporation rates after contraction, a 3 mg/mouse glucose bolus supplemented with 10 μCi/mouse [U-^{14}C] D-glucose (Perkin Elmer, USA) was injected retro-orbitally at the end of contractions. After 30 min, muscles were collected and processed as described above. Circulating glucose levels were assessed and tail blood was sampled every 10 min.

Single-fiber muscle mitochondria immunofluorescent labeling and super-resolution structured illumination microscopy (SIM) imaging

Fixation, permeabilization and staining of mitochondria in single muscle fibers was performed as previously described.[120] Briefly, a quarter of freshly dissected QUAD muscle was secured with two pins onto the bottom of a silicon-covered petri dish and submerged in 5 mM procaine in Krebs buffer (pH 7.4) for 5 min. Next, the procaine solution was substituted for Zamboni fixative (2% formaldehyde, 0.15% picric acid) and left for 30 min at RT. After ON fixation, the samples were washed with PBS and teased into smaller bundles of muscle fibers (20-30 fibers), which were then transferred into new vials filled with 50% (v/v) glycerol PBS solution. After an ON incubation at 4°C, the vials were moved to -20°C and stored there until further processing. Single muscle fibers were dissected from these prefixed biopsies under a stereomicroscope. The isolated fibers were washed with PBS and permeabilized with 0.1% Triton X-100 in PBS for 10 min at RT. Samples were then incubated with a primary rabbit polyclonal IgG antibody against complex IV (ab16056, Abcam, Cambridge, MA, USA) diluted 1:500 in the immune buffer (50 mM glycine, 0.25% BSA, 0.03% saponin, 0.05% NaN_3 in PBS; pH 7.3-7.4) ON at RT on a table shaker. Then, the fibers were washed with PBS three times for 60 min each and left ON with a secondary Ab conjugate goat anti-rabbit Alexa Fluor 488 (A11008, Invitrogen) diluted 1:500 in the immune buffer on a table shaker and protected from light. To label the nuclei, a DNA dye Hoescht 33342 (Thermo Fisher Scientific) was applied on the muscle fibers for 20 min (1:1000, immune buffer). After two 60 min washes in the immune buffer, the latter was substituted with PBS, and samples were washed for another 20 min before being mounted onto the glass microscopy slides (15-20 fibers/slide) with ProLong Glass Antifade Mountant, (P36980, ThermoFisher) and coverslips of 0.17 ± 0.001 mm thickness (#1.5). The slides were kept in the dark at -20°C and were RT-equilibrated for a few hours prior to imaging. Image acquisition was performed on Elyra 7 Super Resolution Microscope (Zeiss, Germany) in the SIM mode, using Plan-Apochromat 63x objective (NA 1.4, oil immersion) and ZEN Black (Zeiss, Germany) software.

For each biological replicate, 15-17 muscle fibers were imaged at three randomly selected locations. The images were acquired as ZStacks with 100 nm between optical planes. The thickness of the analyzed muscle fibers was in the range between 20 to 45 μm. The fluorophores were excited by the 405 (Hoechst) and 488 (Alexa Fluor 488) HR Diode lasers and the following set of filters was used on the emission: BP490-560/LP640 and BP420-480/BP495-550/LP650. The settings for the Lattice SIM reconstruction were optimized on a subset of samples before these parameters were applied to all images (ZEN Black, Zeiss). The reconstruction of the images resulted in significantly improved x-y resolution (up to 120 nm). Further analysis was done in Fiji.[95] For the quantification of mitochondrial fractional volume, the images were first thresholded with Otsu method and then mitochondrial area was measured for every slice of the stack. Since the distance between stacks was constant, average mitochondrial area normalized to fiber area (total area) was considered equal to the mitochondrial fractional volume. For the mitochondrial network analysis, thresholded images were skeletonized and the skeletons were analyzed with Skeletonize 2D/3D and Analyze Skeleton 2D/3D plugins. Mitochondrial network was defined as mitochondria connected through more than one junction. Mitochondrial network size was assessed by the quantification of its branches number. Mitochondrial network complexity was evaluated by correlating the average number of junctions to the mitochondrial fractional volume. In addition, the correlation between the average length of mitochondrial branches and the number of branches was evaluated.

RNA extraction and quantitative reverse-transcriptase PCR

Pulverized muscle tissue samples were lysed in Trizol Reagent (Thermo Fisher Scientific) following the manufacturer's protocol. Upon chloroform addition and subsequent centrifugation, the aqueous upper phase containing RNA was collected and mixed with 70% ethanol. The extraction and further purification of the total RNA pool were achieved by using the columns-based RNeasy kit, including the DNase treatment (Qiagen, Germany). The quantity of the extracted RNA was assessed on a NanoDrop 2000 spectrophotometer (Thermo Fisher Scientific). cDNA from 1 μg of extracted RNA was synthesized in the reverse-transcription reaction via an iScript cDNA Synthesis Kit (Bio-Rad). The qPCRs were performed using Brilliant III Ultra-Fast SYBR Green QPCR Master Mix (Agilent Technologies, USA) and the following sets of primers (Table S2). For every primer pair, we prepared a standard curve to check for the linearity of the relationship between the log(concentration) of the input cDNA and the obtained CT values. Data on each sample were normalized to the expression of the housekeeping gene (*18s*).

Muscle RNA sequencing

Total RNA was isolated from QUAD with Trizol and RNeasy kit (Qiagen), and its quality was verified with 2100 Bioanalyzer Instrument (Agilent). Messenger RNA sequencing was performed by the Single-Cell Omics platform at the Novo Nordisk Foundation Center for Basic Metabolic Research. Libraries were prepared using the Universal Plus mRNA-seq protocol (Tecan) as recommended by the manufacturer. Libraries were quantified with NuQuant using the Qubit fluorometer (Thermo Fisher Scientific), quality checked using a TapeStation instrument (Agilent Technologies) and subjected to 52-bp paired-end sequencing on a NovaSeq 6000 (Illumina).

The nf-core[121] RNA-seq pipeline[122] v.3.8.1 was used to align RNAseq reads against the GRCm38 genome assembly and ENSEMBL release 75 transcripts,[123] using default alignment and quantification. Testing for differential expression was performed using edgeR[124] v.3.38.0. Raw counts were filtered to retain genes with sufficient expression across samples using the *filterByExpr()* function. Normalization to account for differences in library sizes was performed using *calcNormFactors()*.To estimate the dispersion of the data, the *estimateDisp()* function was applied. Following normalization, gene counts were transformed into log counts per million (logCPM) for visualization purposes, including the generation of heatmaps and multi-dimensional scaling (MDS) plots. For the identification of differentially expressed genes, a generalized linear model quasi-likelihood (GLM-QL) approach was used via the *glmQLFit()* function, using a group means model of the form ~ group, where "group" encoded the genotype. Contrasts were constructed so that a positive logFC indicated an increase in the "KO" condition. The quasi-likelihood F-test was applied to determine differential expression between experimental conditions, ensuring robust control over false positives. Genes with a false discovery rate (FDR) < 0.05 were considered significantly differentially expressed.

Glycogen

Glycogen content in muscle and liver was measured with the amyloglucosidase method after glycogen precipitation in ethanol as previously described.[125] Mice were either randomly fed (Figures 1I and 2D) or fasted for 4 h (Figures 2G–2I). Briefly, a portion of frozen pulverized tissue (30 mg for muscle and 15 mg for liver) was lysed in 200 μL of 1M KOH by incubation at 70°C until completely digested. Next, 75 μL of Na_2SO_4 (saturated) and 1.7 mL of absolute ethanol were added, and the samples were centrifuged at 18,000 *g* for 15 min at 4°C after mixing. The resulting pellet was then dissolved in 200 μL of H_2O. To aid dissolving, the samples were incubated at 70°C for about 20 min. The resulting solution was mixed with 1.8 mL of absolute ethanol, and after mixing the samples were centrifuged as above. The pellet was resuspended in 1 mL of 250 mM acetic acid neutralized to pH 4.75 with NaOH. Next, supplemented with one unit of amyloglucosidase (Merck A1602) per mL of buffer the samples were incubated at 37°C with shaking (800 rpm), ON. Free glucose was detected colorimetrically with a commercial GOD-PAP glucose assay (Randox), following the kit's manual. The values were normalized by tissue weight.

NAD^+, $NADP^+$ and NADH assays

The concentrations of NAD^+, $NADP^+$, NADH and NADPH were measured using the cycling assay, as previously described.[120] When performed on mitochondrial isolates, no mechanical homogenization was required. The data were normalized to tissue weight or protein content of the mitochondrial lysates measured with the bicinchoninic acid assay (Thermo Fisher Scientific #23227).

NAD metabolome HPLC-QTOF

LC-MS was used to profile NAD metabolites following the method described previously.[126,127] Briefly, frozen muscle tissue was cryo-pulverized and re-suspended in extraction solvent which was 80% methanol. The ratio between tissue and solvent was 1:20 (w:V). Extraction solvent contained heavy isotope labelled internal standards in concentration of 0.5 ng/μL. The IS mix contained: NA-d_4, NAM-d_4, NAD-d_4, NADH-d_4, ATP-$13C_{10}$, MeNAM-d_4, adenosine-$^{13}C_5$ and tryptophan-d_5. Suspension was sonicated in icy water for 15 min and left to precipitate on ice for another 15 min. Samples were centrifuged for 3 min with 11,292 g (Eppendorf Centrifuge 5810R) at 4°C and 200 μL of the supernatant was transferred in HPLC vial and evaporated until dryness. Sample was reconstituted with 50 μL of 50% methanol. The remaining extract after centrifugation was used to create pooled samples used for control purposes. Calibration curves were prepared so part of the extraction solvent was replaced with dilution series of native standards.

Samples were analyzed using Agilent 1290 Infinity II ultra-high performance liquid chromatograph coupled with Bruker Timstof pro mass spectrometer. Samples (2 μL) were injected into ACQUITY Premier BEH Amide VanGuard FIT Column (1.7 μm, 2.1 mm X 150 mm), with mobile phases consisted of (A) 10 mM ammonium acetate in water and 5 μM of medronic acid, and (B) 10 mM ammonium acetate in 90/10 acetonitrile/water and 5 μM of medronic acid. The mobile phase was delivered to the column by a flow rate of 0.2 mL/min at the following gradient: 0 min (95% B), 2 min (95% B), 10 min (55% B), 12 min (55% B), 12.5 min (95% B), 18 min (95% B). The column temperature was 40°C.

Mass spectra were acquired by positive electrospray ionization using scanning mode ranging from 50 to 1,000 Da with 1Hz scan speed. Raw data was converted into MzML format using Proteowizard and peak extraction was made with MzMine 2.53 using targeted extraction protocol. Extraction protocol included the following steps: Mass detection, target metabolite extraction, join aligner, peak filtering and gap filling. Concentrations were calculated using linear equations based on standard curves.

NAD metabolome HPLC-QQQ

NAD labelled internal standard mix containing NA-d4, Nam-d4, NAD-d4, MeNam-d4, adenosine-$^{13}C_5$, tryptophan-d5, NADH-d4, ADP-$^{15}N_5$, ATP-$^{13}C_{10}$ and AMP-$^{13}C_{10}{}^{15}N_5$ (10 μg/mL) in MeOH was prepared. For the extraction solvent, the NAD labelled standard mix was mixed with MeOH and 0.1 M formic acid (2:2:1). Three (3) ceramic beads (2.8 mm) were added to each sample tube containing powdered muscle tissue. For every 10 mg of tissue, 180 μL of extraction solvent was added. The tubes were placed in a tissue-lyser (TissueLyser II, QIAGEN) and lysed at 30 Hz for 4 x 30 s intervals. After lysis, 20 μL of 15% ammonium carbonate solution was added to each tube (ratio of extraction solvent: 15% NH_4CO_3 is 9:1).

The contents were transferred to 1.5 mL Eppendorf tubes and incubated on ice for 30 min to allow proteins to precipitate. The tubes were centrifuged at 11,292 *g* for 3 min (Eppendorf Centrifuge 5810R), at 4°C. Finally, 50 μL of the supernatant was transferred to an LC vial, and 25 μL was transferred to a 2.0 mL Eppendorf tube for pooled samples. Aliquots of 50 μL of the pooled samples were transferred to LC vials. NAD calibration standard mix for calibration was prepared in MeOH (final concentration 40 μg/mL). A dilution series were prepared with 100% MeOH for a calibration curve in the range of 0.001-40 μg/mL.

The samples were analyzed by a Waters ACQUITY Premier UPLC coupled with the Waters Xevo TQ-XS triple quadrupole mass spectrometer (Waters Corporation, Milford, Massachusetts). Samples (1 μL) were injected into a Waters ACQUITY Premier BEH Amide column (1.7 μm, 2.1 x 150 mm), with mobile phases consisted of (A) 10 mM ammonium acetate in water and 5 μM of medronic acid, and (B) 10 mM ammonium acetate in 90/10 acetonitrile/water and 5 μM of medronic acid. The mobile phase was delivered to the column by a flow rate of 0.2 mL/min at the following gradient: 0 min (90% B), 1.5 min (90% B), 11 min (50% B), 11.5 min (35% B), 15 min (35% B), 15.5 min (90% B) 19 min (90% B). The column temperature was 40°C. Samples were analyzed in positive electrospray ionization mode, using MRM (transitions listed in Table S3). Raw data were processed in Waters TargetLynx software. Calibration curves were used for the quantification of the compounds, with limits of detection determined based on a signal to noise (S/N) ratio >3.

Citrate synthase activity

Citrate synthase (CS) activity was measured on the muscle tissue lysate or mitochondrial extracts, as described previously.[128,129] Quadriceps muscle was pulverized and lysed with steel beads using a Tissuelyzer II (Qiagen, Germany), 2 × 90 s at 30 Hz. The lysis buffer contained 10% glycerol, 1% IGEPAL, 50 mM HEPES, 150 mM NaCl, 10 mM NaF, 1 mM EDTA, 1 mM EGTA, 20 mM sodium pyrophosphate, 2 mM sodium orthovanadate, 1 mM sodium-pyrophosphate, 5 mM nicotinamide, 4 mM Thiamet G and protease inhibitors (Sigma #S8820) pH 7.4. Lysates were incubated on the end-over-end rotator for 45 min at 4°C, and the supernatant was collected after 10 min of centrifugation (16,000 *g*, 4°C). Protein concentration was determined using the bicinchoninic acid assay (Thermo Fisher Scientific #23227) and a standard curve. The citrate synthase activity was assayed in the reaction mix (0.1 M This HCl, pH 8.1, 0.4 mM acetyl-CoA sodium salt (Sigma-Aldrich, #A2181) and 1 mM 5,50-dithiobis(2-nitrobenzoic acid) (Sigma-Aldrich, #D8130)) containing 0.02 mg/mL of mitochondrial or 0.2 mg/mL of the total muscle protein extract. The optical density was measured at λ412 nm for 5 min at 30 s intervals (basal slope) followed by the addition of 10 mM oxaloacetic acid (Sigma-Aldrich, #O4126), after which the measurement was resumed and continued for another 10 min at 30 s intervals (reaction slope). The citrate synthase activity was calculated from the delta of the reaction and the basal slopes (linear parts).

Western blot analyses

Quadriceps muscle lysates were prepared as described above. Protein samples (10-35 μg) were separated via SDS-PAGE, followed by semi-dry transfer on the activated PVDF membranes (Millipore #Ipvh 00010), which, after blocking with 3% skim milk or 3% BSA in

TBS-T buffer, were incubated overnight with one of the following primary antibodies: NAMPT (Bethyl lab #372A), poly- and mono-ADP ribose (Cell Signaling Technology D9P7Z #89190), acetyl lysine (Cell Signaling Technology #9441). Rinsed membranes were incubated with the anti-rabbit (Bio-Rad, #170-6515) HRP-conjugated antibody according to the manufacturer's protocol. Membranes were developed and imaged with Chemidoc XRS+ (Bio-Rad) and Lumina Forte Western HRP Substrate (Millipore). Images were analyzed in Image Lab software (Bio-Rad) .

DNA extraction and mitochondrial to genomic DNA ratio (mt/nDNA)

The mitochondrial to genomic DNA ratio was estimated following the previously published protocol.[130,131] First, total DNA samples were obtained from pulverized quadriceps muscle with the DNeasy Blood & Tissue Kit (Qiagen, Germany). Samples were treated with RNase A (Thermo Scientific #EN0531) upon extraction following the manufacturer's protocol. Then, the samples were sonicated at 4°C for 10 cycles (30 s rest each cycle) using Bioruptor Plus sonication device (Diagenode). The DNA concentration was measured on a NanoDrop 2000 spectrophotometer (Thermo Fisher Scientific) and further dilution of the samples to 4 ng/μl was made. The qPCRs were performed using Brilliant III Ultra-Fast SYBR Green QPCR Master Mix (Agilent Technologies, USA) and the following primers: genomic *Ucp1*, *Pparg*; mitochondrial *Cytb* (for the sequences of the oligonucleotide primers used here, see Table S2). The mDNA/nDNA was calculated using $2^{*}2^{\wedge}(Ct_{n}DNA\text{-}Ct_{m}DNA)$, and the ratio of control samples was set to one.

Epigenetic clock and DNA methylation analysis

DNA from QUAD of young and old control and *Nampt* KO mice was isolated with the DNeasy Blood & Tissue Kit (Qiagen, Germany). The epigenetic age analysis was performed by Clock Foundation, USA. Briefly, DNA methylation of 320,000 genomic regions was measured using the custom mammalian array 'HorvathMammalMethylChip320', combining HorvathMammalMethylChip40 and the 285k Illumina Mouse Methylation BeadChip.[132]

Raw data were transformed into methylation estimates (beta values) by normalization with the SeSAMe R package.[133] Beta values were derived from the ratio of the fluorescence intensity of a methylated probe for a specific CpG to the total probe intensity (the sum of the signal from both the methylated and unmethylated probes plus a constant).[134] These values fell in the range from zero to one, where zero indicated no methylation. A beta value was generated for each probe of the array for every animal and was supported by a detection p-value corresponding to the confidence in the normalized beta value.

For the age predictive analysis, a 320k array was transformed into a 40k one by selecting the probes, which aligned between both arrays with a correlation exceeding 0.8. For the missing probes, the gold median values determined from a substantial mouse reference dataset were used. A series of quality control steps were performed to ensure the adequacy of the input data for the analysis. Probes with both methylated and unmethylated channels reporting background signal levels were marked as failed using the p-value threshold of $p > 0.01$. The proportion of failed probes was calculated for each sample. Samples with a scaled proportion of failed probes greater than 2 were considered outliers. PCA of the centered, unnormalized beta-value matrix was computed, and samples with higher than 2 SDs of the first three principal components were marked as outliers. The hierarchical clustering of the samples and the inter-array correlation were calculated and the samples deviating more than 2 SDs from the mean were excluded from the analysis as the outliers. In total, three samples out of 47 were removed based on these criteria. Figure 7E presents age prediction results based on the general and skeletal muscle-specific CpG methylation clocks (Universal and Muscle-specific clock, respectively).

The DNA methylation data generated for all 320k sites were included in a separate analysis (epigenome-wide association study) and were used to identify differentially methylated CpGs between young and old control and NAD-deficient animals. Differentially modified cytosines (DMCs) analysis assumed that methylation patterns across the genome were independent. Normalized beta values were used to fit the linear regression model using the R package limma v3.50.3.[135] The model was adjusted for Age, Genotype and Sentrix_ID. The adjustments for the unknown confounders were performed using the R package RUVSeq v1.28.0 with 3 RUVg vectors.[136] The models were fitted using the least-squares method by running lmFit function. Empirical Bayes statistics were estimated using *eBayes* function. Benjamini-Hochberg method was used to correct for the multiple testing and q-value < 0.05 was considered statistically significant. Epigenetic clock predictions are provided in Table S4.

Muscle glutathione concentrations

Muscle tissue GSSG content was determined spectrophotometry with the GSH recycling method, while GSH was measured with HPLC, as shown previously.[137] Importantly, upon quadriceps muscle excision, it was promptly homogenized in the N-ethylmaleimide (NEM) containing buffer to convert GSH to GS-NEM, which protects it from oxidation and avoids significant GSSG overestimation.

Nuclear magnetic resonance (NMR)

NMR was used for the quantification of NAD^{+} and nicotinamide (NAM) in the gastrocnemius muscle samples harvested from the control and knockout animals. First, polar metabolites were extracted. For that, tissue was pulverized and ~30 mg of tissue powder was further homogenized using a TissueLyser II (Qiagen, Germany). The lysate was cleared by centrifugation (4°C, 2,371 *g*, 5 min) and transferred into a glass tube containing 1.4 mL of 2:1 acetone:isopropanol mix (HPLC grade). Tubes were vortexed briefly and placed on an orbital shaker (750 rpm 10 min) (Fisherbrand multi-tube vortexer, Fisher Scientific, UK). Samples were then centrifuged (1,376 *g*, 5 min), and the supernatant was transferred into a new glass tube followed by the addition of 1 mL water and 500 μL chilled (-20°C) chloroform (HPLC grade). Tubes were once again agitated (750 rpm 10 min) and centrifuged (2,150 *g*, 5 min). The polar

aqueous layer (2 mL) was transferred into a new tube and placed into a SpeedVac (ThermoFisher Scientific, UK) (30°C 4-5 h). The resulting dried pellet was stored reconstituted in 60 μL of 100 mM sodium phosphate buffer, pH 7.0. After brief vortexing, samples were sonicated for 5 min, and a 50 μL portion was transferred into the champagne vials. A Gilson liquid handling robotic system (Cortecnet, USA) then transferred 35 μL from the vials into the 1.7 mm NMR tubes. NMR tubes were loaded into Bruker Neo 800 MHz NMR spectrometer, equipped with a 1.7 mm z-PFG TCI Cryoprobe. A NOESY1d pulse sequence was used to achieve water suppression. Automatic tuning and matching was used and all samples were shimmed to a TMSP line-width of <1 Hz. In total 128 transients with 16,384 complex data points (1.31 s FID acquisition time) were recorded for each sample, with a total of 16 steady-state scans per sample. The interscan relaxation delay was set to 4 seconds and the spectral width of 12500 Hz (15.63 ppm). Total acquisition time for each spectrum was approximately 13 min. The data were acquired in the form of ^{1}H 1D-NMR spectra, which were analyzed via using MetaboLab (version 2021.0401.1752).[138] The D4-TMSP signal was set at 0 ppm and chemical shifts were calibrated accordingly. Spectra for all samples were first manually phased and then baseline corrected. The area under each peak of interest was integrated and compared to the integrated area under the TMSP peak to calculate the concentration of the metabolites of interest. The original powdered tissue weight was used for data normalization.

Gas chromatography mass spectrometry (GC-MS)

GC-MS was utilized for targeted ion quantification of the metabolites of interest. Samples were prepared as described above (NMR). An aliquot of the polar phase (200 μL) was placed into a SpeedVac (ThermoFisher Scientific, UK) (30°C, 1-2 h) and yielded a dried pellet, which was further put through a two-stage derivatization protocol. At first, pelleted samples were treated with 40 μL of 2% methoxamine in pyridine (1 h, 60°C). Next, 50 μL of 1% (w/v) tertbutyldimethyl-chlorosilane in N-tertbutyldimethylsilyl-N-methyltrifluoroacetamide was added (1 h, 60°C). The tubes were left closed during both incubation steps to prevent evaporation. The samples were then transferred to a GC-MS chromatography vial with a glass insert (ThermoFisher Scientific, UK). Agilent 8890 GC and 5977B MSD (Agilent Technologies UK Limited, UK) were used to perform the analysis. 1 μL of sample was injected into the chromatographer (splitless mode, helium carrier gas at a rate of 1.0 mL min^{-1}). The oven temperature was set to 100°C for 1 min, then to increase to 170°C (rate 10°C min^{-1}), then to further increase to 200°C (rate 5°C min^{-1}) with a final stage of 320°C (rate 10°C min^{-1}) and a 5 min hold. Metabolites were detected in the scan mode, with the subsequent total ion count of each metabolite being normalized to the internal standard D6-glutaric acid. The original powdered tissue weight was used for ion counts normalization.

AMPK activity assay

AMPK activity was assayed as previously described.[139] Quadriceps and EDL muscles lysates were incubated with protein G-Sepharose coupled antibodies for 1 hour at 4°C. The antibodies used here were custom-made: AMPKγ1 (YenZym #YZ5115) and AMPKγ3 (YenZym #YZ4698).[33] The immune complexes were pelleted by centrifugation (500 *g*, 1 min) and washed twice in 0.5 mL lysis buffer supplemented with 500 mM NaCl, followed by a second wash with 0.5 mL buffer A (50 mM HEPES pH 7.4, 150 mM NaCl, 1 mM EGTA, and 1 mM DTT), which was performed twice. The immune-complex suspension was then incubated for 45 min at 30°C under agitation in buffer A supplemented with 10 mM magnesium acetate, 100 μM ATP and 200 μM AMARA peptide (NH_2-AMARAASAAALARRR-COOH) in presence of [γ-^{32}P]ATP (1 μCi). Reactions were terminated by spotting the reaction mixtures onto P81 filters and immersing in 75 mM phosphoric acid. Washed filters were dried, and ^{32}P substrate AMARA incorporation was measured by Cherenkov counting (5 min) using a scintillation counter (Hidex 300SL, Hidex, Finland).

Muscle ROS staining

Staining of the total TA muscle ROS was performed as described previously.[140] Briefly, TA muscles were excised immediately after an exercise bout and frozen embedded in OCT TissueTec (#4583, Sakura Finetek, USA) in the liquid nitrogen pre-cooled isopentane. Samples were kept at -80°C until further processing. Later, 10 μm thick muscle cryosections were incubated with 10 μM of 2′,7′-dichlorofluorescin diacetate in PBS (Molecular Probes, Eugene) and left to dry ON at room temperature in the dark. Vectashield mounting medium (H-1000; Vector Laboratories) was used to prepare all slides. Images were acquired with LSM 710 with ×20 0.8 NA Plan Apo objective (Zeiss), Zen 2012. Data are presented as the fluorescence ratio (λ480/535 nm) normalized to the levels of rested control group.

Muscle histological analysis

TA muscles were fixed in 4% buffered paraformaldehyde solution, embedded into paraffin, sectioned into 10 μm thick sections and placed on the microscopy glass slides. Pircosirius red staining was performed by overnight incubation in Bouin's fixative followed by Weigert's reagent and DirectRed80 in picric acid water solution. Imaging was performed on Zeiss Axio Scan Z.1 Slide Scanner microscope (Zeiss, Germany), with a 20x magnification objective. Images were processed in Fiji.[141] Fiber size was quantified in a semi-automated user-supervised manner. For centralized nuclei quantification, the images were first segmented via Cellpose cyto 3 with default parameters and a typical cell size was set to 150px. To quantify the nuclei position, the images were then processed using the color deconvolution function with a H&E DAB template. The first channel was denoised using a median filter of size 5 and and MaxEntropy algorithm was applied to create a binary mask of all the nuclei. To quantify the position of the nuclei relative to the fiber center, the maximum value of the distance mask was used as a reference point indicating the middle of a cell (100%). The plotted ratio was calculated by dividing the maximum value of the nucleus mask applied on the distance mask, and the center value obtained as

indicated above. A nucleus was considered centralized if its position was within 15% of a fiber's center and only fibers containing a single nucleus were analyzed. The script can be found here: https://github.com/rdemets/Cellpose_Nuclei_Position-ImageJ.

Oxygen consumption rate and mitochondrial inner membrane potential modelling

The computational modelling of OCR and IMMP was performed in MatLab and used the published model of mitochondrial bioenergetics for heart muscle.[38] OCR and IMMP were modelled for a range (7) of mitochondrial NAD concentrations with 250 μM representing 100%. Respiratory substrates and ADP concentrations used in the model were selected to fit the conditions under which the experimental data were obtained.

Fluorescence-activated cell sorting-based quantification of muscle stem cell number

The quantification of muscle stem cell abundance in skeletal muscle of young and old WT and iSMNKO mice was measured with fluorescence-activated cell sorting (FACS) as previously described.[142] In brief, hindlimb and triceps muscles were excised from the animals and cleaned by removing fat and tendons. Muscle tissue was minced with scissors and enzymatically digested using a combination of Collagenase II and Dispase (Invitrogen). With several washing and filtering steps, a suspension of mononucleated cells was obtained. These cells were next stained with the following combination of conjugated antibodies for 40 min: APC anti-mouse CD31 (clone MEC13.3; Biolegend, cat. no. 102510), APC anti-mouse CD45 (clone 30-F11; Biolegend, cat. no. 103112), BV421 anti-mouse Ly-6A/E (anti-Sca1, clone D7; Biolegend, cat. no. 108128), and PE/Cy7 anti-mouse CD106 (anti-VCAM1, clone 429; Biolegend, cat. no. 105719). In addition, the cells were stained with the viability dye ZombieYellow (1:100, Biolegend, cat. no. 423103) for 15 min. After staining, the cells were spiked with a suspension of counting beads (CountBright Absolute Counting Beads (Invitrogen)) and sorted using a FACS Aria-II (BD Biosciences). An unstained control sample was used to adjust voltages on the cell sorter. In addition, single channel and fluorescence minus one (FMO) staining controls for each channel as well as appropriate antibody isotype controls were used to ensure that positive populations could be distinctly separated from background. The population of single $VCAM1^+$, $CD31^-$, $CD45^-$, $Sca1^-$ cells was measured and the counts were normalized to the beads count and input tissue weight.

Analysis of muscle mitochondria membranes lipid composition

Lipids were extracted from muscle mitochondrial fraction (isolated as described above) using Folch extraction[143] with 8-12 replicates from each experimental group at each timepoint. Prior to lysis, Splash mix (Merck) was added to the extraction solvent, and mitochondrial samples were lysed by beat beating in a FastPrep-24 homogenizer. After centrifugation and phase separation, the apolar and polar phases were transferred to separate tubes, and the apolar phase dried under N_2. Samples were resuspended in 30 μL methanol/chloroform (1:1) and centrifuged (5 min/16,000 *g*, 22°C) before transferring to HPLC vials. A quality control sample was constructed by pooling 3 μL of each sample. Samples (0.5 μL) were injected using a Vanquish Horizon UPLC (Thermo Fisher Scientific) equipped with a Waters ACQUITY Premier CSH (2.1 × 100 mm, 1.7 μM) column operated at 55°C. The analytes were eluted using a flow rate of 400 μL/min and the following composition of eluent A (Acetonitrile/water (60:40), 10 mM ammonium formate, 0.1% formic acid) and eluent B (Isopropanol/acetonitrile (90:10), 10 mM ammonium formate, 0.1% formic acid): 40% B from 0 to 0.5 min, 40–43% B from 0.5 to 0.7 min, 43–65% B from 0.7 to 0.8 min, 65–70% B from 0.8 to 2.3 min, 70–99% B from 2.3 to 6 min, 99% B from 6–6.8 min, 99–40% B from 6.8–7 min before equilibration for 3 min with the initial conditions. The flow from the UPLC was coupled to a TimsTOF Flex (Bruker) instrument for mass spectrometric analysis, operated in both positive and negative ion modes.

Compounds were annotated in Metaboscape (Bruker) using both an in-built rule-based annotation approach and the LipidBlast MS2 library.[144] Features were removed if their average signals were $\leq 5\times$ in QC samples than in blanks (water extraction). The signals were normalized to internal standards in the SPLASH mix before correction for signal drift using the statTarget R package.[145] Finally, signals were normalized using the QC samples.[146] Peak intensities from each measured metabolite were scaled using Pareto scaling with *MetabolAnalyze* (version 1.3.1) and $\log_2$ transformed. Differentially abundant lipid species were identified with a two-tailed paired t-test and Benjamini-Hochberg p-value correction. The processed data are provided in Table S5.

Proteomics analyses

Global proteome analysis of skeletal muscle from WT and iSMNKO (Figure 3D)

Skeletal muscle samples were lysed in 4% sodium dodecyl sulfate (SDS) in 100 mM Tris pH 8.5, 10mM Tris(2-carboxyethyl)phosphine (TCEP), 40mM chloroacetamide (CAA) using an Ultra Turrax homomgenizer (IKA). Lysates were boiled for 10 min at 95°C, sonicated using a tip sonicator, centrifuged at 16,000 *g* for 10 min and the supernatant collected. Samples were acetone precipitated and resuspended in 1% sodium deoxycholate. Protein digestion occurred via the addition of LysC and trypsin (1:100 w/w) at 37°C overnight. Digested peptides were acidified via the addition of 1% trifluoroacetic acid (TFA) and precipitated SDC removed via centrifugation. Peptides were purified using Sep-pak C18 cartridges (Waters). Mass spectrometry and data processing was performed as described previously.[147] Bioinformatics analyses were performed in Perseus software.[97] Quantified proteins were filtered to have at least 70% valid values in at least one group. Missing data were imputed by drawing random numbers from a Gaussian distribution with a standard deviation of 30% and a downshift of 1.8 standard deviations from the mean. To identify differentially regulated

proteins, a two-tailed paired t-test was performed with a permutation-based false discovery correction applied (FDR = 0.05). Samples were measured and quantified alongside additional groups, however, only WT and iSMNKO data are included in this manuscript. The processed data are provided in Table S6.

Mitochondrial supercomplexome analysis (Figures 5C–5F)

Mitochondrial fractions for blue native polyacrylamide gel electrophoresis (BN-PAGE) were prepared as previously described.[148] In brief, mitochondrial pellets (control and iSMNKO, sedentary and exercised mice), containing 75 μg protein each, were lysed in NativePAGE sample buffer 1.5% digitonin, mixed with NativePAGE 5% G-250, and loaded into NativePAGE 3-12% Mini Protein Gels (Invitrogen). The outer and the inner chambers of the electrophoresis system were filled with anode buffer (1X NativePAGE Running buffer) and cathode buffer (0.01% Coomassie Brilliant Blue G-250 in anode buffer), respectively. The electrophoresis was set to run at 150 V, 4°C. After 30 min, the dark blue cathode buffer was replaced with light blue cathode buffer (9% dark blue cathode buffer in anode buffer) and the electrophoresis run continued for another 60 min at 250 V. Then, the gels were rinsed in water, and 10 selected bands out of each gel lane were cut out with a scalpel and collected into bar-coded tubes.[49] Next, samples were randomized to minimize potential batch effects before being loaded in a Hamilton robot, where automated in-gel protein digestion with trypsin and LysC was performed.

The resulting tryptic peptides were separated on a Pepsep 8 cm, 150 μM ID column packed with C18 beads (1.5 μm) using an Evosep ONE HPLC system applying the default 60-SPD (60 samples per day) method. Column temperature was maintained at 35°C. Upon elution, peptides were injected via a CaptiveSpray source and 20 μm emitter into a timsTOF pro2 or SCP mass spectrometer (Bruker) operated in PASEF mode. MS data were collected over a 100-1700 m/z range with TIMS mobility range of 0.6-1.6 1/K0. Ion mobility was calibrated using three Agilent ESI-L Tuning Mix ions 622.0289, 922.0097 and 1221.9906. TIMS ramp and accumulation times were set to 100 ms each with 10 PASEF ramps recorded for a total cycle time of 1.17sec. MS/MS target intensity and intensity threshold were set to 20,000 and 2,500, respectively. An exclusion list of 0.4 min for precursors within 0.015 m/z and 0.015 V cm^{-2} width was activated.

Raw spectra were processed using the MaxQuant software[96] (version 2.1.4.0). The analysis was performed with default settings with the exception of the match between runs option. For protein group inference, a reference UniProt mouse FASTA file was provided (October 2022). Downstream bioinformatics were conducted within the R environment (R version 4.3.1). Label-free quantification columns from the ProteinGroups.txt file were uploaded to R studio before $\log_2$ transformation and filtered so only the proteins that were detected in $\geq$70% of the samples of at least one experimental group (in 6 samples out of 8-9) were kept for the analysis. Then, samples were grouped by animal ID, quantile normalized, and merged back into a single data frame. To visualize the different respiratory complexes across bands, the proteins corresponding to each respiratory complex and the mitochondrial ribosome were filtered and displayed as violin plots. Differential abundance analysis was performed using a LIMMA-based workflow adapted for multiple comparisons ($\sim$ genotype * condition). From the resulting differentially abundant proteins, those showing a statistically significant difference between at least two gel bands were selected for visualization. The processed data are provided in Table S7.

Global proteome analysis of skeletal muscle from young, old WT and iSMNKO (Figures 7E–7G)

Muscle samples were lysed in 4% SDS 100 mM Tris with the BeatBox homogenizer (PreOmics) followed by boiling at 95°C for 5 min on a thermomixer. The homogenates were sonicated with a probe sonicator (Bioruptor) set to 50% intensity for 15 cycles (1 sec on, 1 sec off). The lysates were cleared by centrifugation by spinning for 10 min at 20,000 *g*. The protein content in the supernatants was determined with the DC assay (Thermo Fisher). An equal amount of protein (40 μg) from each sample was reduced and alkylated by adding 40 mM chloroacetamide (CAA) 10 mM pH-neutral Tris(2-carboxyethyl)phosphine hydrochloride (TCEP) and incubating at 45°C for 5 min on a shaking thermomixer. Protein digestion was performed on the KingFisher Flex robot (Thermo Fisher) following the protein aggregation capture protocol with the protein to MagReSyn Hydroxyl Beads ratio of 1:4 (Resyn Biosciences).[149] The samples were washed with 100% acetonitrile (twice), and 70% ethanol (once). The proteolytic enzymes Trypsin and LysC in 100 mM Tris were used in 1:100 and 1:500 enzyme-to-protein ratios, respectively. After the overnight incubation, their activity was quenched with 1% trifluoroacetic acid (TFA) (twice). The digests were centrifuged at 20,000 *g* for 10 min and the supernatants were desalted on the Sep-Pak C18 plates (Waters). After a two-step elution (40% and 60% acetonitrile), the peptides were dried with SpeedVac and resuspended in the MS injection buffer. The peptide concentration was determined with Lunatic spectrophotometer (Unchained Labs). Equilibrated Evotips (Evosep) were loaded with 200 ng of peptides.

Peptides were separated on a Pepsep 15 cm, 150 μM ID column packed with C18 beads (1.5 μm) using an Evosep ONE HPLC system applying the default 30-SPD (30 samples per day) method. Column temperature was maintained at 50°C. Upon elution, peptides were injected via a CaptiveSpray source and 20 μm emitter into a timsTOF Pro 2 mass spectrometer (Bruker) operated in diaPASEF mode. MS data were collected over a 100-1,700 m/z range. During each MS/MS data collection each PASEF cycle was 1.8 seconds. Ion mobility was calibrated using three Agilent ESI-L Tuning Mix ions 622.0289, 922.0097, and 1221.9906. For diaPASEF we used the long-gradient method which included 16 diaPASEF scans with two 25 Da windows per ramp, mass range 400.0-1,201.0 Da, and mobility range 1.43-0.6 1/K0. The collision energy was decreased linearly from 59 eV at 1/K0 = 1.6 to 20 eV at 1/K0 = 0.6 Vs cm-2. Both accumulation time and PASEF ramp time were set to 100 ms.

Raw data were quantified in Spectronaut version 18.4 using DirectDIA mode and default settings. The data were searched against the reviewed UniProt Mouse FASTA file (downloaded on 24.01.2023, 17,137 entries). Data processing and analysis were performed in R studio (R version 4.3.1). Data were $\log_2$ transformed and median scaled. Batch correction was performed using *prcomp()* and the dataset was filtered for 55% of valid values for proteins in at least one group. Differentially expressed proteins were determined with LIMMA. In short, a linear model with eBayes smoothing was used to test for the main effect of age (old, young), genotype (KO, WT),

and their interaction. Multiple hypothesis testing was corrected with Benjamini-Hochberg. GSEA of gene ontology (GO) was performed using the clusterProfiler package and GO terms with more than 70% significance were filtered out with the *simplify()* function. The processed data are provided in Table S8.

QUANTIFICATION AND STATISTICAL ANALYSIS

Data are presented as mean +/- standard error of the mean (SEM). Significance was defined as $p < 0.05$ and the significance level is indicated in figure legends. The statistical parameter "n" represents the sample size in each experiment, and it is reported in the figure legends. For comparisons between two groups (1 factor) a two-tailed unpaired Student's t-test was applied. A two-way analysis of variance (ANOVA) test was used to determine significance when comparing four groups (2 factors). Significant interactions between the factors were further tested with the Holm-Šídák post hoc. Data analysis and graphing were performed in GraphPad Prism 10, R and Matlab. Schematics were created with BioRender.com.